universität wien

DISSERTATION | DOCTORAL THESIS

Titel | Title

Positron preparation for (anti-)hydrogen measurements in the ASACUSA-Cusp experiment

verfasst von | submitted by

Andreas Lanz BSc MSc

angestrebter akademischer Grad | in partial fulfilment of the requirements for the degree of

Doktor der Naturwissenschaften (Dr.rer.nat.)

Wien | Vienna, 2025

Studienkennzahl lt. Studienblatt | Degree programme code as it appears on the student record sheet:	UA 796 605 411
Dissertationsgebiet lt. Studienblatt | Field of study as it appears on the student record sheet:	Physik
Betreut von | Supervisor:	Hon.-Prof. Dipl.-Phys. Dr. Eberhard Widmann

Abstract

The ASACUSA-Cusp experiment at CERN aims to measure the ground-state hyperfine splitting of antihydrogen in a low magnetic field region using a spin-polarised beam of antiatoms. Antihydrogen is produced via three-body recombination by merging a positron and an antiproton plasma in a Penning-Malmberg trap.

The focus of this work lies on the preparation of the positron plasma to achieve an increase in the production rate of antihydrogen atoms. The positron apparatus was upgraded and characterised. Within the scope of this work, the first measurements of evaporatively cooling positrons and compressing the positron plasma in the strong drive regime in the ASACUSA-Cusp experiment was performed.

The developments in the plasma control made it possible to convert up to 80 % of the trapped antiprotons into antihydrogen, yielding up to 0.4 million antiatoms. Additionally, the evolution of the temperature, radial density profile and the number of particles of the antiproton and positron plasmas were measured during the production of antihydrogen, yielding insight into the formation process. Further, the temperature dependence of the three-body recombination process was measured by heating the positron plasma and detecting the resulting number of antihydrogen atoms.

Last but not least, a low energy proton source was successfully installed into the experiment. This source was developed for times when CERN does not provide antiprotons. With this source it is possible to investigate the production of hydrogen by mixing protons and electrons in the same apparatuses used for antihydrogen production in a much shorter time frame. The results can then be applied to the antimatter experiments.

Zusammenfassung

Das Ziel des ASACUSA-Cusp Experiments am CERN ist die Messung der Aufspaltung der Hyperfein Struktur von grundzustands Antiwasserstoff in einem niedrigen Magnetfeld mittels eines Spin-polarisierten Strahl aus Antiatomen. Antiwasserstoff wird durch eine Drei-Körper Rekombination erzeugt, indem ein Positronen- und ein Antiprotonen-Plasma in einer Penning-Malmberg Falle zusammengeführt werden.

Der Fokus dieser Arbeit liegt in der Vorbereitung des Positronen-Plasmas, um eine Steigerung der Produktionsrate von Antiwasserstoff zu erreichen. Das Positronen System wurde erneuert und charakterisiert. Im Rahmen dieser Arbeit wurde zum ersten Mal Kühlung durch Verdunstung ("evaporative cooling") von Positronen und die Kompression von einem Positronen-Plasma im Strong Drive Regime, im ASACUSA-Cusp Experiment gemessen.

Wegen der verbesserten Kontrolle des Plasmas war es möglich, bis zu 80 % der gefangenen Antiprotonen in Antiwasserstoff umzuwandeln, was bis zu 0.4 Millionen Antiatomen entspricht. Zusätzlich wurde die Entwicklung der Temperatur, der Anzahl der Teilchen und des radiales Dichteprofils des Antiprotonen- und des Positronen-Plasmas während der Produktion von Antiwasserstoff gemessen. Dies gab einen Einblick in den Formierungsprozess. Des Weiteren wurde die Temperaturabhängigkeit des Drei-Körper Rekombinationspozesses gemessen, indem das Positronen-Plasma aufgeheizt wurde und die jeweilig produzierten Antiwasserstoffatome detektiert wurden.

Zu guter Letzt wurde eine Niederenergie-Protonenquelle erfolgreich in das Experiment installiert. Die Quelle wurde für Zeiten, in denen CERN keine Antiprotonen bereitstellt, entwickelt. Mit dieser Quelle ist es möglich, die Wasserstofferzeugung durch das Kombinieren von Elektronen und Protonen im gleichen experimentellen Aufbau, der für die Erzeugung von Antiwasserstoff verwendet wird, in einer sehr viel kürzeren Zeitspanne zu untersuchen. Die Ergebnisse können dann auf Antiwasserstoff angewendet werden.

Acknowledgement

First of all, I would like to express my sincere gratitude to Eberhard for the invaluable opportunity to pursue my PhD within this incredibly exciting experiment.

I want to thank Dan for giving me the chance to carry out the work in his group. His support and guidance have been instrumental in allowing me to contribute to this collaboration, and I am deeply appreciative of his confidence in me and for all the really helpful conversations we had.

Furthermore, I would like to extend my deepest thanks to Eric, who worked alongside me on-site and generously shared his expertise, teaching me much of the practical knowledge essential to becoming an experimental physicist. Achieving these results would have been far more challenging without his guidance and support.

I would also like to thank the many members of the collaboration who welcomed me warmly and made me feel truly included. A special mention goes to those who worked closely on the positron system, sharing their expertise and enthusiasm.

A heartfelt thank you to all my colleagues at SMI, who made the rare times I spent in Vienna truly unforgettable. Special thanks to all my friends who supported me through stressful times, and especially to Bernie, James, and Lili, whose company made the after-work moments at CERN truly enjoyable.

Last but not least, I want to express my deepest gratitude to my family: to my parents for their unwavering support - without which I wouldn't be where I am today - and to my brother, who always found time to help me unwind and keep me sane amidst the work.

Contents

Chapter 1

Motivation

1.1 Antimatter

In 1928 Dirac unified special relativity and quantum mechanics [1, 2]. The consequence of which was that the wave equation for an electron moving in an electromagnetic field had both a positive and a negative energy solution. The negative energy solution can be explained as an "electron with positive electric charge". In 1932 Anderson, in a cloud chamber experiment, discovered a particle with the same deflection radius as the electron but traveling in the opposite direction, i.e. having the same mass as the electron but positive electric charge [3, 4]. What he discovered was the antiparticle of the electron, the positron.

Every particle, e.g. the electron (e^-) or the proton (p), has its own antiparticle, e.g. the positron (e^+) and the antiproton ($\overline{p}$)[1]. An antiparticle has the same properties (for example the mass, lifetime, etc.) as its matter counterpart and the same absolute value but oppositely signed charges (e.g. electric charge, magnetic moments, etc.). A fundamental property is that when a particle collides with its antiparticle annihilation can occur, i.e. the production of lighter particle-antiparticle pairs or photons (e.g. $e^+ + e^- \rightarrow 2\gamma$, $p + \overline{p} \rightarrow \pi^+ + \pi^- + \pi^0$). Furthermore, particle-antiparticle pairs can be generated by the interaction of energetic particles, where the minimum energy in the center of mass system must be twice the equivalent rest mass energy of the product (e.g. $p + p \rightarrow p + p + p + \overline{p}$). Similarly to ordinary matter, antiparticles can form atoms, for example the antiproton and positron can form an antihydrogen atom ($\overline{H}$).

The Big Bang theory strongly suggests that matter and antimatter should have been produced in equal quantities, which means that based on current understanding they should have annihilated. Nevertheless, the universe consists mainly of matter and very little antimatter is observed. From measurements of the cosmic microwave background by the WMAP experiment [5] and measurements of the ratio of low-energetic antiprotons and protons [6] one can estimate the baryon-antibaryon asymmetry in the universe to be

[1] Antiparticles are often denoted by the matter symbol with an over bar or by their electric charge.

$$\eta = \frac{n_{\mathrm{B}} - n_{\overline{\mathrm{B}}}}{n_\gamma} \approx 10^{-10}, \tag{1.1}$$

where n_x, x = (B, $\overline{\mathrm{B}}$, and γ) are the number densities of the baryon, antibaryon and cosmic background photons in the universe. This opens the question of the origin of this asymmetry. Possible explanations will be discussed in Section 1.3.

1.2 The Standard Model of Particle Physics and Symmetries

The current model for describing particles and their interactions is the Standard Model of Particle Physics (SM). The SM is an effective field theory with the local gauge symmetry group $\mathrm{SU}(3)_C \times \mathrm{SU}(2)_L \times \mathrm{U}(1)_Y$. Particles in this model are described as excitations of their underlying quantum fields and forces are mediated by bosons. The three fundamental forces described in the SM are:

- **Electromagnetic interaction** mediated by photons.
- **Weak interaction** mediated by the $\mathrm{W}^{\pm}$ and Z^0 boson.
- **Strong interaction** mediated by gluons.

From this list one can immediately see the downside of this model: even though it describes many particles and their interactions it is not complete. For example, gravity is not explained within this model. Another problem in the SM is the assumption that neutrinos are massless. Pontecorvo described neutrino oscillations [7], later observed by the Homestake experiment [8], which can only occur if neutrinos have mass. These are just two examples which show that the SM is not a complete description of nature. Models which try to include physics which cannot be explained by the SM are often referred to as Physics Beyond the Standard Model (BSM).

In the SM, as well as in other theories in physics, symmetries play an important role. A symmetry can be described as a transformation under which the physical laws stay the same. For example, the translation in time: if an experiment is repeated under the same initial conditions at a different time, the result is the same. There are several other symmetries in physics (e.g. Galileian transformations, Lorentz transformations, rotations, etc.) which leave the laws of physics invariant. The importance of symmetries can be seen by the Noether-theorem, which connects symmetries to conserved properties [9]. For example, the conservation of energy follows from the invariance of translations in time ($t \to t+\Delta t$) and the conservation of momentum from the invariance of translations of space ($x \to x + \Delta x$).

Symmetries can be divided into two groups: continuous (e.g. time translation: $t \to t + \Delta t$) and discrete (e.g. time reversal: $t \to -t$). In particle physics, three important discrete symmetry transformations exist:

- **Parity (P)**: Point reflection ($\vec{r} \rightarrow -\vec{r}$).
- **Charge conjugation (C)**: Transformation of all charges, which can be seen as the exchange of particles with their antiparticles (C→-C).
- **Time reversal (T)**: Inversion of the time ($t \rightarrow -t$).

It was shown independently by Lüders [10] and Bell & Peierls [11] that every Lorentz-invariant local field theory - like the SM - is invariant under the simultaneous transformation of parity, charge conjugation and time reversals, which is the so-called CPT-theorem. It means that when mirroring the space, transforming all particles into their antiparticles and reversing time, the laws of physics stay the same.

In 1957, it was found by Wu *et al.* that parity is not conserved in weak interactions by studying the Beta-decay of ^{60}Co [12]. Additionally, this experiment showed that charge conjugation is broken. However, at that time it was believed that CP-transformations are invariant. In 1964, Christenson and co-workers detected CP-symmetry violation in the neutral kaon system [13]. As a consequence, the CPT-theorem implies that time reversal must be broken as well to restore the symmetry, which was observed by the BABAR experiment in 2012 [14]. Several experiments are searching for CPT-violation, however, so far no experimental evidence has been found. One of these is the ASACUSA-Cusp experiment, which aims to measure differences between the hydrogen and antihydrogen ground-state hyperfine energy levels.

1.3 Hyperfine splitting & Standard Model Extension

As mentioned above, an abundance of baryons over antibaryons in the universe exists, however, it cannot be explained by the SM. In 1991, Sakharov proposed three conditions to explain the observed asymmetry [15]:

- Baryon number violation,
- C- and CP-symmetry violation,
- The baryon-antibaryon annihilation rate must have occurred smaller than the pair creation rate, i.e. the interactions are out of thermal equilibrium.

Thus far, no violation of the baryon number has been observed. CP-violation has been seen [12], as mentioned in the preceding section, however, the measured effect is too small to explain the observed asymmetry. Nevertheless, these conditions are only necessary under the assumption that CPT-invariance is present. A small violation of CPT-symmetry can be used as a different explanation for the abundance of matter [16].

In 1998, Colloday and Kostelecký published a framework which was called the Standard Model Extension (SME) [17, 18]. In this framework the SM Lagrangian was extended by Lorentz- and CPT-violating terms but maintaining properties of the theory

like renormalizability, microcausality and being hermitian. The idea is that background fields exist, which give rise to CPT-violating terms. As the focus of this work lies in the ASACUSA-Cusp experiment, the following section will only expand upon the parts of the SME which can be constraint by measuring the energy levels of ground-state (anti-)hydrogen. The full derivation of the energy levels within the SME can be found in [19] and is briefly described below.

1.3.1 Hyperfine splitting of (anti-)hydrogen

The hyperfine splitting of an atom arises from the interaction of the magnetic moment of the nucleus and the electron(s). The total angular momentum quantum number of the atom $F = J + I$ is the sum of the total angular momentum quantum number of the electron(s) $J = L_\mathrm{e} + S_\mathrm{e}$ and the nucleus $I = L_\mathrm{N} + S_\mathrm{N}$, with the angular momentum quantum number of the nucleus (electron(s)) L_N (L_e) and the spin quantum number of the nucleus (electron(s)) S_N (S_e). The possible quantum numbers are $F = |J - I|, ..., J + I$ in steps of one. For the ground state the angular momentum is zero and as a consequence the total angular momentum of the orbit and the nucleus are equal to the spin of the proton and the electron(s), i.e. $\vec{F} = \vec{S_e} + \vec{S_p}$. As protons and electrons are both spin-1/2 particles, the total spin of the system can either be $F = 0$ (singlet state) or $F = 1$ (triplet state). The transition frequency between the singlet and the triplet states was measured in hydrogen to be [20]

$$\nu_0 = (1420405751.768 \pm 0.001)\mathrm{Hz}. \tag{1.2}$$

Additionally, the magnetic moment of the atom (i.e. the sum of the magnetic moments of the nucleus and the electron) can interact with an external magnetic field resulting in a potential energy $V = -\vec{\mu} \cdot \vec{B}$. This gives rise to a Zeeman-splitting of the states, as shown in Fig. 1.1. The states can be grouped into low-field-seeking states (LFS, red and black line in Fig. 1.1) and high-field-seeking states (HFS, green and grey lines in Fig. 1.1), depending on their behaviour in the external magnetic field.

For antihydrogen described by the SM the splitting, as well as the energy levels, stay the same. Due to the opposite sign of the magnetic moments, the behaviour in an external magnetic field switches the labels of $\mathrm{H} : (F = 1, m_F = 1) \rightarrow \mathrm{H} : (F = 1, m_F = -1)$.

1.3.2 Hyperfine splitting in the Standard Model Extension

As protons and electrons are fermions, they are described by the Dirac-Lagrangian

$$\mathcal{L}_D = \overline{\psi}(i\gamma^\mu \partial_\mu - m_\mu)\psi + \mathrm{h.c.}, \tag{1.3}$$

where γ^μ are the γ-matrices, m_μ is the mass of the fermion, ψ is the spinor field and $\partial_\mu = \frac{\partial}{\partial x^\mu}$. In the SME, the Dirac-Lagrangian is extended by the spinor matrix $\hat{\mathcal{Q}}$, which

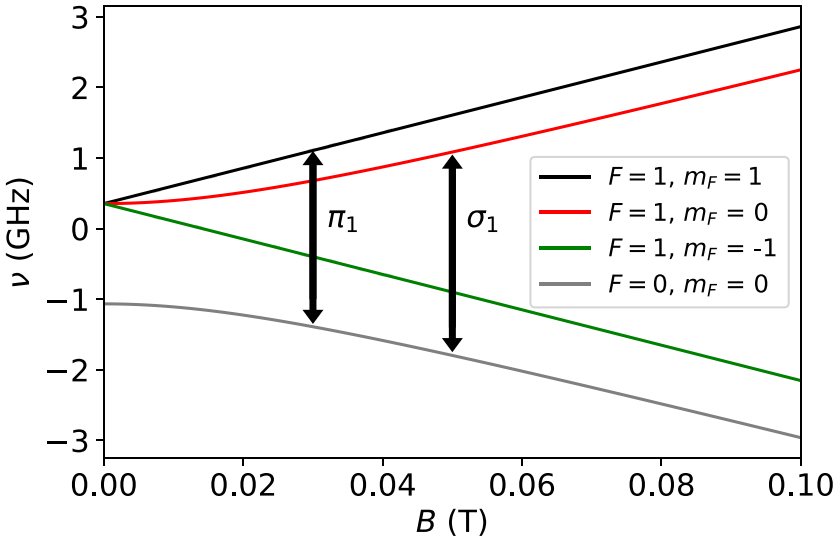

Figure 1.1: Zeeman splitting of the ground-state hyperfine structure of hydrogen. For antihydrogen the states $(F = 1, m_F = 1)$ and $(F = 1, m_F = -1)$ are swapped. The two transitions from a LFS-state into a HFS-state which are relevant for the ASACUSA-Cusp experiment are indicated as well.

is the sum of all possible terms formed by the contraction of Lorentz-and CPT-breaking coefficients with derivative $i\partial_\mu$. The resulting Lagrangian is

$$\mathcal{L}_D^{\mathrm{SME}} = \overline{\psi}(i\gamma^\mu\partial_\mu - m_\mu + \hat{\mathcal{Q}})\psi + \mathrm{h.c.} \tag{1.4}$$

As the effect of the Lorentz- and CPT-violating terms is expected to be small, perturbation theory can be used. The leading order perturbation of the Dirac hamiltonian h_{D} for the hydrogen energy spectrum can be obtained from $\mathcal{L}_D^{\mathrm{SME}}$ by adding the Lorentz-violating contribution of the electron h_{e} and the proton h_{p}

$$h_D^{\mathrm{SME}} = h_{\mathrm{D}} + h_{\mathrm{e}} + h_{\mathrm{p}} = h_{\mathrm{D}} + \delta h_{\mathrm{H}}, \tag{1.5}$$

where $\delta h_{\mathrm{H}} = h_{\mathrm{e}} + h_{\mathrm{p}}$. To calculate the effect of the Lorentz- and CPT-violating terms one has to calculate the matrix elements of the form

$$\langle nFJLm'_F|\, \delta h_H\, |nFJLm_F\rangle = \sum_{jm} A_{jm}\, \langle Fm_F jm|Fm'_F\rangle\,, \tag{1.6}$$

where $|nFJLm_F\rangle$ are the unperturbed states defined by the principal quantum number n, the total angular momentum of the atom F, the total angular momentum of the electron J, the orbital angular momentum L and the magnetic eigenvalue m_F. The weights A_{jm} contain the non-relativistic Lorentz- and CPT-violating coefficients $\mathcal{V}^{\mathrm{NR}}_{wkjm} = c_{wkjm} - a_{wkjm}$ and $\mathcal{T}^{\mathrm{NR}(qP)}_{wkjm} = g^{(qP)}_{wkjm} - H^{(qP)}_{wkjm}$[19]. In this notation the CPT-odd operators are associated with the a- and g-type coefficients and the CPT-even operators with the c- and H-type coefficients. The flavour index $w = e, p$ indicates the

particle type, i.e. electron and proton, and the superscript (qP) are the non-relativistic spherical coefficients for Lorentz violation, which can take the values $0B$, $1B$, and $1E$, and describe the factor gained under a parity transformation of the operator ($(-1)^j$ for E-type operators and $(-1)^{j+1}$ for B-type operators) [21]. For antiparticles the expression stays the same, but the signs of the a- and g-type coefficients are reversed.

For the case of $F = 0, 1$ the matrix elements can be calculated analytically and the resulting energy shifts $\delta\epsilon$ are [19]

$$F = 0: \qquad \delta\epsilon(n, L) = A_{00} = -\sum_{wk} \langle |\vec{p}|^k \rangle_{nL} \frac{\mathcal{V}^{\mathrm{NR}}_{wk00}}{\sqrt{4\pi}} \tag{1.7}$$

$$F = 1: \qquad \delta\epsilon\left(n, L, J = \frac{1}{2}, m_F\right) = A_{00} + \frac{1}{\sqrt{2}} m_F A, \tag{1.8}$$

where $\vec{p}$ is the fermion momentum, and $A = \sqrt{\sum_m A^*_{1m} A_{1m}}$. As one can see, all states gain an equal shift A_{00} which does not affect the transition frequency between two states. As the shift of the states $(F = 0, m_F = 0)$ and $(F = 1, m_F = 0)$ only consists of this constant, the transition between these (the so-called σ_1-transition) is not sensitive to CPT-violation to the order of perturbation described in this model.

A more explicit form of the shifts of the transition energies $\delta\epsilon$ at zero magnetic field can be given in terms of the Lorentz- and CPT-violating coefficients to be [19]

$$\begin{aligned} \delta\epsilon(m_F) = &-\sum_{q=0}^{2} \left(\frac{\alpha m_{\mathrm{r}}}{n}\right)^{2q} \left(1 + \left(\frac{8n}{2L+1} - 4\right)\delta_{q2}\right) \\ &\times \sum_w \frac{\mathcal{V}^{\mathrm{NR}}_{w(2q)00}}{\sqrt{4\pi}} + \frac{m_F}{2\sqrt{3\pi}} \left(\mathcal{T}^{\mathrm{NR}(0B)}_{w(2q)10} + 2\mathcal{T}^{\mathrm{NR}(1B)}_{w(2q)10}\right), \end{aligned} \tag{1.9}$$

where α is the fine structure constant, $m_{\mathrm{r}} = m_{\mathrm{p}} m_{\mathrm{e}}/(m_{\mathrm{p}} + m_{\mathrm{e}})$ is the reduced mass and δ_{2q} is the Kronecker delta. From that it is possible to calculate the frequency shift $\delta\nu$ of the ground-state between two states with Δm_F to be

$$\begin{aligned} 2\pi\delta\nu = &-\frac{\Delta m_F}{2\sqrt{3\pi}} \sum_{q=0}^{2} (\alpha m_{\mathrm{r}})^{2q} (1 + 4\delta_{2q}) \\ &\times \sum_w \left[g^{\mathrm{NR}(0B)}_{w(2q)10} - H^{\mathrm{NR}(0B)}_{w(2q)10} + 2g^{\mathrm{NR}(1B)}_{w(2q)10} - 2H^{\mathrm{NR}(1B)}_{w(2q)10}\right]. \end{aligned} \tag{1.10}$$

In total $2 \times 3 \times 4 = 24$ coefficients contribute to the shift in the transition frequency of states with $\Delta m_F \neq 0$. As mentioned above, the expression for antihydrogen stays the same but with the opposite sign of the CPT-odd coefficients a and g. As a consequence, it is possible that if there was a measurable shift in antihydrogen it could cancel out for hydrogen. If the Lorentz-and CPT-violating coefficients are zero, the energy shifts

are zero, i.e. the unperturbed hyperfine splitting is restored. An illustration of possible effects on the ground-state hyperfine splitting for (anti-)hydrogen is shown in Fig. 1.2. The SME does not predict the sign and value of the CPT-violating coefficients, i.e. the direction of the shifts. However, for the case of a shift in hydrogen as indicated as the red dashed line, antihydrogen will have a shift indicated as the green dashed line and vice versa. Distinct energy levels are possible in the SME even at zero magnetic field.

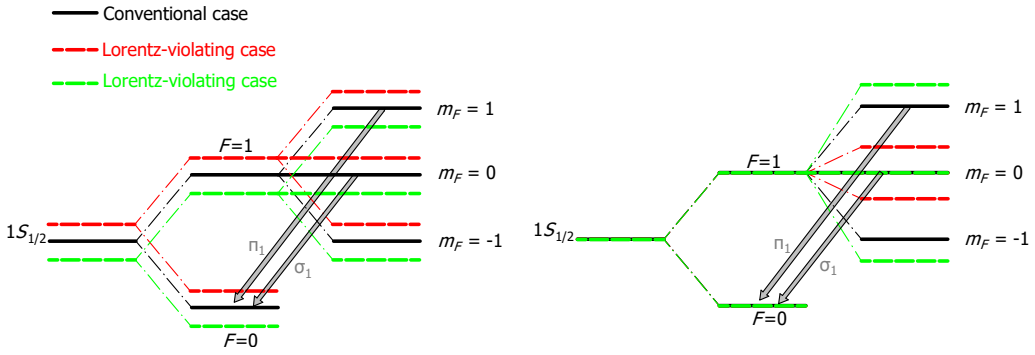

Figure 1.2: Diagram of the hyperfine splitting of hydrogen without (black) and with (red dashed & green dashed lines) possible CPT-violating effects for a constant shift of all sublevels (left) and a shift of levels $m_F = 1, -1$ (right). The colours indicate possible directions of the shifts. The σ_1- and π_1-transitions are indicated for the conventional case as grey arrows.

1.4 ASACUSA-Cusp experiment

The ASACUSA (**A**tomic **S**pectroscopy **A**nd **C**ollision **U**sing **S**low **A**ntiprotons) collaboration consists of two flagship experiments: The ASACUSA-Cusp experiment [22] (which will be the scope of this work) and antiprotonic helium laser spectroscopy to measure the antiproton-to-electron mass ratio [23]. The ASACUSA-Cusp experiment aims to measure the ground-state hyperfine splitting of antihydrogen using a spin-polarised beam of antiatoms in a low magnetic field region [24]. As mentioned in the previous section, a possible CPT-violation could give rise to an energy splitting of the $F = 1$ state of the hyperfine splitting in zero magnetic field. A difference of the transition frequency of the states ($F = 1$, m_F=1) $\rightarrow$ ($F = 0$, m_F=0) - the so-called π_1-transition - between hydrogen and antihydrogen can be a measure for CPT-violation within the SME, as indicated on the right hand side (RHS) of Fig. 1.2.

The ASACUSA experiment is located in the Antiproton Decelerator (AD) facility at CERN. This facility is the only location worldwide where low-energy antiprotons are available. The first production of cold antihydrogen was reported by the ATHENA collaboration in 2002 [25] and shortly after by the ATRAP collaboration [26]. Today there are several different approaches to study antimatter. Six experiments are currently performing measurements on (or with) low-energetic antiprotons. The collaborations

working in the AD and a short description of the flagship experiments are listed below:

- **ASACUSA**: In-beam measurement of the ground-state hyperfine structure of antihydrogen [22] and antiproton-to-electron mass ratio using antiprotonic helium [23].
- **ALPHA**: Antihydrogen laser spectroscopy. Wide spectrum of experiments, including: fine structure [27], 1S-2S transition [28], hyperfine splitting [29], and gravitational behaviour of antihydrogen [30].
- **BASE & BASE-STEP**: Magnetic moment [31] & charge-to-mass ratio [32] of antiprotons, and development of a portable antiproton trap [33].
- **AEgIS**: In-beam measurement of the gravitational behaviour of antihydrogen [34].
- **GBAR**: Measurement of the Weak Equivalence Principle using antihydrogen [35].
- **PUMA**: Development of a portable trap for antiprotons [36] with the aim of creating antiprotonic atoms with short-lived nuclei to study the nucleon distributions of these nuclei.

1.4.1 Experimental method

A description of how to produce antihydrogen will be given in Chapter 2.3 and the setup of the ASACUSA-Cusp experiment will be described in detail in Chapter 3. In this subsection, the experimental technique will be described.

The ASACUSA-Cusp experiment will use a Rabi-type method [37] to measure the ground-state hyperfine splitting of antihydrogen. A schematic diagram of the technique is shown in Fig. 1.3.

Antihydrogen atoms are produced by mixing antiprotons and positrons in the so-called Cusp trap, which receives its name from the strongly inhomogeneous - a cusped - magnetic field along the trap axis [22]. The strongly inhomogeneous magnetic field spin-polarises the antihydrogen atoms, i.e. it focuses the two LFS-states and defocuses the two HFS-states. The LFS-states enter the spin-flip cavity, in which a longitudinally oscillating magnetic field of $\sim$ 1.42 GHz is applied. Additionally, a small (order of mG) homogeneous magnetic field perpendicular to the cavity is used to induce Zeeman-splitting of the energy levels. A spin-flip is induced by the microwave field, transforming one of the LFS-states into a HFS-state. The subsequent analysing sextupole magnet deflects the atoms which underwent a transition (i.e. the HFS-states) and focuses the atoms which remained in the initial state (i.e. the LFS-states) onto a detector. At the transition frequency between the two states a minimum in the count rate can be detected.

As mentioned previously, the ALPHA collaboration performed a measurement on the hyperfine splitting of antihydrogen [29]. The relative precision achieved in this experiment was $3.5 \cdot 10^{-4}$ using trapped antihydrogen in a magnetic field of $\sim$1 T. However,

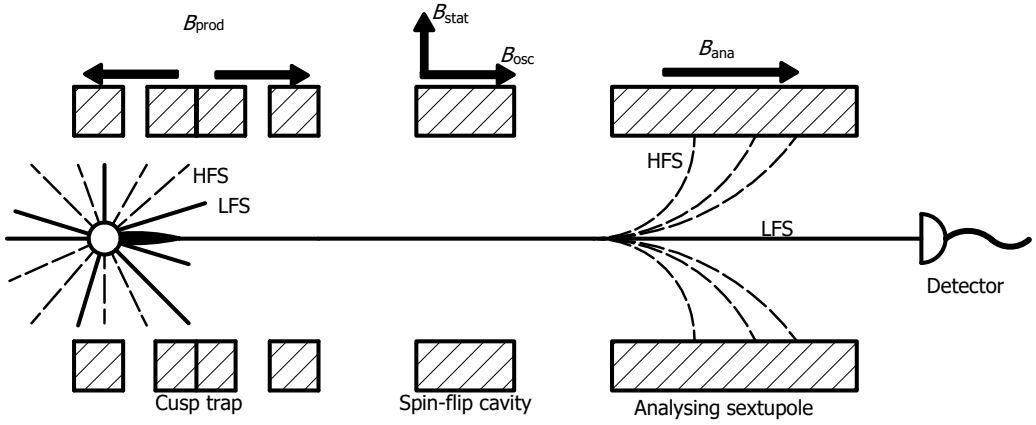

Figure 1.3: Schematic of a Rabi-experiment. The hatched blocks indicate the position of the coils producing the magnetic field in the production region (B_{prod}), the static (B_{stat}) and oscillating (B_{osc}) fields in the spin-flip cavity, and the magnetic field in the analysing sextupole magnet (B_{ana}). The deflected HFS-states are indicated as dashed lines, the LFS-states are indicated as solid lines. Adapted from [37].

in order to be able to trap antihydrogen strong magnetic fields are necessary, these limit the precision of this measurement due to the strong magnetic field dependence of the transitions. The advantage of the in-beam measurement, as proposed by the ASACUSA collaboration, is that the atoms can be transferred from the high field production region into a low magnetic field region. This enables the possibility of a much more sensitive measurement. The initial goal of the ASACUSA-Cusp experiment is to reach a relative precision of 10^{-6}, which is mainly limited by the low production rate of ground-state antihydrogen atoms. Measurements using the same spin-flip cavity in a similar apparatus with hydrogen showed that it is possible to achieve a relative precision of $4.4 \cdot 10^{-10}$ [38]. Additionally, it was shown that the spin-flip cavity is designed such that it is possible to measure either the σ_1- or π_1-transition, without the necessity to change the setup in between measurements.

Nevertheless, using an in-beam measurement opens new challenges. A low field is needed, therefore shielding must be added to remove effects of stray fields and the earths magnetic field at the cavity. Another challenge is the amount of antihydrogen in the ground state which is needed to perform this measurement. As the atoms are not trapped, the time to de-excite is limited by the time-of-flight between the production region and the interaction region. Therefore, it is important to increase the number of atoms produced in states with low principal quantum number.

1.4.2 Previous results

In 2010, the ASACUSA-collaboration successfully produced antihydrogen atoms in the Cusp trap [39]. It was estimated that approximately 2-7 % of the antiprotons were converted into antihydrogen atoms in high Rydberg states. The mixing scheme used was "direct injection". In this technique antiprotons with an energy of $\sim 145\,\mathrm{eV}$ are

transferred directly from the antiproton trap into the positron plasma, which was held in a potential well as shown in Fig. 1.4. The disadvantages of this method were that (i) due to the energy spread of the antiprotons the positron temperature increased via the injection of the antiprotons and (ii) the antiprotons and positrons separated axially due to energy loss of the former by interacting with electrons formed in annihilation on background gas and the reduction of axial energy due to collisional relaxation [40]. A consequence of (ii) was that the antihydrogen formation process terminated when the axial energy of the antiprotons dropped below the positron potential energy. To counteract this termination of the process a radio-frequency (rf) assisted direct injection was used, in which a rf drive was applied during mixing which excited the axial oscillation of the antiprotons [40]. With this technique the number of antihydrogen atoms produced could be increased by a factor of 3.5. Further, the antihydrogen detector was installed 2.7 m downstream of the antihydrogen production trap, which is the position the microwave cavity will be installed. An electric field ioniser was used to give a lower limit on the principal quantum number n of antihydrogen atoms reaching the detector, which yielded 6 atoms with $n \gtrsim 43$ and 4 atoms with $n \gtrsim 29$ in one mixing cycle ($\sim$ 15 minutes) [40]. This was the first observation of antihydrogen atoms outside of the mixing trap. However, in these measurements no diagnostic of the properties of the positron and antiproton plasmas was present, hence it was not possible to optimise the formation process with respect to the initial parameters of the plasmas.

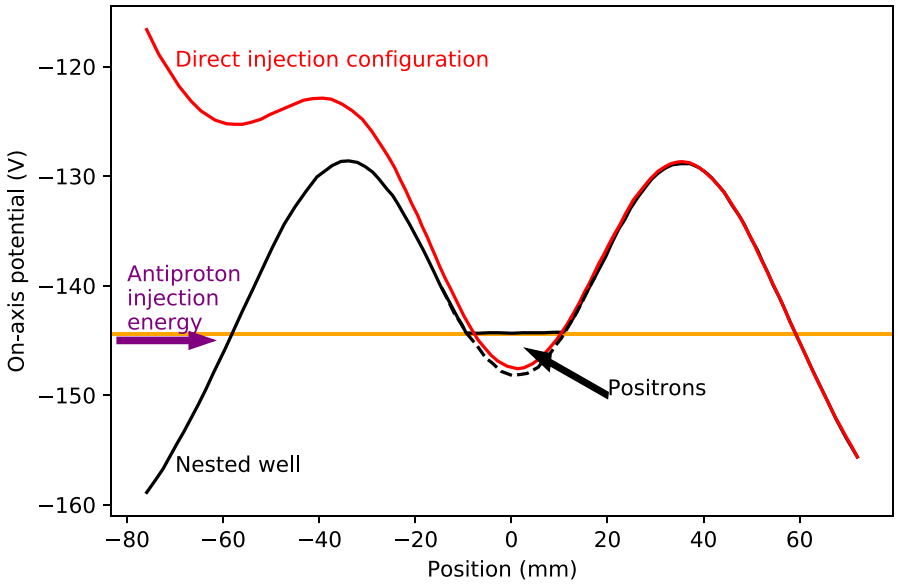

Figure 1.4: On-axis potential in the direct injection scheme. The positrons are held in a nested well (black solid line), which on-axis potential is changed due to the space charge of the positrons (black dashed line). The well is opened (red solid line) for letting the antiprotons into the trapping well to interact with the positrons to produce antihydrogen. Adapted from [40].

In 2018, a systematic measurement of the distribution of the principal quantum number of the produced antihydrogen at the entrance of the spectroscopy beamline was

performed [41]. The antihydrogen production technique was the same as previously used but with a reduced energy spread of the antiprotons and an improved matching of the energies of the two species. As a consequence the increase of the positron temperature during the injection is lower [41]. The atoms were field ionised and the n-state of the atoms was measured as a function of applied field. The resulting n-states were given as $n_{100\%} > n \geq n_{\text{threshold}}$, being described as the range between the minimum state which is partly ionised ($n_{\text{threshold}}$) and the lowest n-state which is fully ionised ($n_{100\%}$). The result was that most of the atoms were produced in high Rydberg states [41], as can be seen in Fig. 1.5.

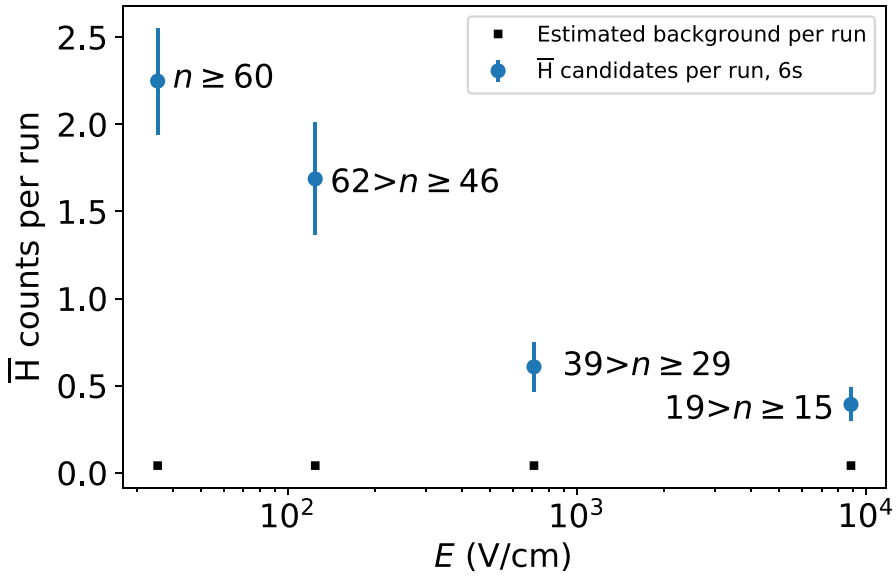

Figure 1.5: Number of antihydrogen atoms per run as a function of the field strength of the field ioniser. Data from [41].

Only 0.395 ± 0.096 of the atoms per production cycle ($\sim$ 15 minutes) were in low n-states ($15 \leq n < 19$), which are able to decay into the ground-state before reaching the spin-flip cavity. This experiment showed the necessity to increase the production of atoms in low $n-$states by one to two orders of magnitude.

This work will describe the improvements which were made to the experimental setup as well as the techniques to increase the number of antihydrogen atoms produced, which is necessary to achieve the first in-beam measurement of the hyperfine splitting of antihydrogen.

Chapter 2

Theoretical background

2.1 Penning trap

An ideal Penning trap is an apparatus consisting of three hyperboloidally shaped electrodes (two endcaps and one central cylinder) and an axial magnetic field, as shown in Fig. 2.1.

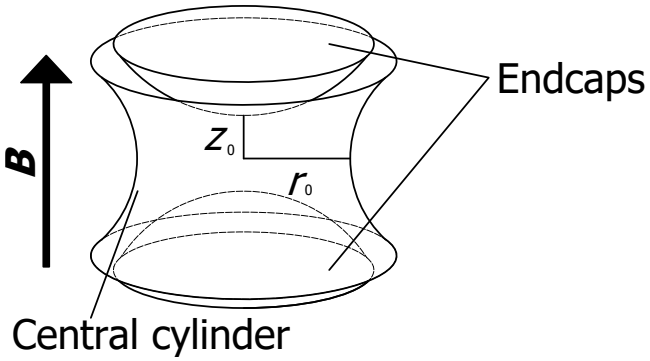

Figure 2.1: Schematics of the electrodes of an ideal Penning trap. A magnetic field is applied along the z-axis.

The trapping idea was based on the observation of the extension of the free path of a charged particle in a crossed electric and magnetic field by Penning [42] and the hyperboloidal trap was realised by Dehmelt [43]. By applying an electrical potential $\pm V_0/2$ to the endcaps the resulting potential along the trap has the form

$$\phi(x, y, z) = \frac{V_0(z^2 - \frac{x^2+y^2}{2})}{2R^2}, \tag{2.1}$$

that is, it is a harmonic potential in both the axial and radial directions, where $R = \frac{1}{2}\sqrt{z_0^2 + \frac{r_0^2}{2}}$, with r_0 and z_0 as shown in Fig. 2.1. In a pure electrostatic field, the axial motion of a single particle of charge $+e$ and mass m can be described by $F_z = -e(\vec{\nabla}\phi)_z$, i.e. through the differential equation

$$m\ddot{z} = -e(\vec{\nabla}\phi)_z = -\frac{eV_0}{R^2}z, \tag{2.2}$$

where m is the particle mass and e the elementary charge. The solution yields the axial oscillation frequency of the particle

$$\omega_z = \sqrt{\frac{eV_0}{mR^2}}. \tag{2.3}$$

The particle is trapped on-axis, however, it could escape radially, hence the application of a magnetic field along the trap axis. For simplicity, the magnetic field is assumed to be along the z-axis, i.e. $\vec{B} = (0, 0, B_z)$, which has no effect on the z-component of the force, and therefore the solution of the electrostatic case Eq. (2.3) is still valid. Starting from the Lorentz force $\vec{F} = -e\vec{\nabla}\phi + e\vec{v} \times \vec{B}$ and introducing the cyclotron frequency $\omega_c = \frac{qB}{m}$, the three equations of motions can be written as

$$\ddot{x} = \frac{\omega_z^2}{2}x + \omega_c\dot{y}, \tag{2.4}$$

$$\ddot{y} = \frac{\omega_z^2}{2}y - \omega_c\dot{x}, \tag{2.5}$$

$$\ddot{z} = -\omega_z^2 z. \tag{2.6}$$

Solving the two coupled equations for the radial motion in the $x - y$ plane by using the substitution $u = x + iy$ results in

$$\omega_\pm = \frac{\omega_c}{2} \pm \sqrt{\frac{\omega_c^2}{4} - \frac{\omega_z^2}{2}} \tag{2.7}$$

The two frequency solutions are called the modified cyclotron ω_+ and the magnetron motion ω_-. Stable confinement is achieved when the quantity under the square root is positive. This is typically guaranteed as the inequality chain $\omega_c \gg \omega_z \gg \omega_-$ holds. Figure 2.2 shows a qualitative sketch of the individual and the combined motions of a single particle in a Penning trap which are summarised as

$$\omega_- = \frac{\omega_c}{2} - \sqrt{\frac{\omega_c^2}{4} - \frac{\omega_z^2}{2}}, \tag{2.8}$$

$$\omega_+ = \frac{\omega_c}{2} + \sqrt{\frac{\omega_c^2}{4} - \frac{\omega_z^2}{2}}, \tag{2.9}$$

$$\omega_z = \sqrt{\frac{eV_0}{mR^2}}. \tag{2.10}$$

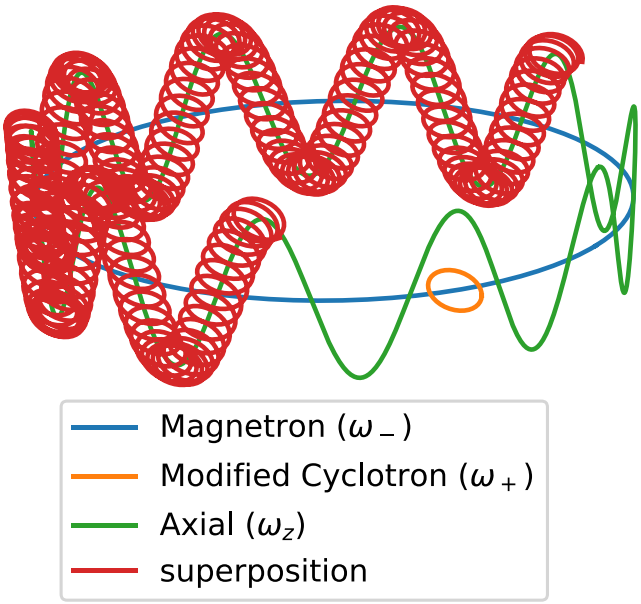

Figure 2.2: Schematic of the motions of a single particle in a Penning trap: magnetron motion (blue), modified cyclotron motion (orange), axial motion (green), and the superposition of all (red).

Cylindrical traps

The idealised Penning trap shown in Fig. 2.1 is often not applicable for experiments. A different approach, using cylindrical electrodes and flat endcaps was introduced by Gabrielse and Mackintosh [44]. It was found that harmonic potentials could be achieved in the center of a stack of cylindrical electrodes with different lengths and diameters. Further, the setup was improved by having open ended cylindrical endcaps [45]. The advantage of cylindrical electrodes is that they can be machined to a higher precision than hyperboloidally shaped electrodes in a shorter time. Additionally, by having open ended electrodes, the trap is easily accessible, which is important if the particles to be trapped need to enter (or leave) the trapping region.

2.2 Non-neutral plasma in Penning-Malmberg traps

For antihydrogen production a large number of particles need to be trapped. For this purpose a special cylindrical trap, specifically aimed at containing a large quantity and possibly density of particles, i.e. a non-neutral plasma, was developed by Malmberg, the Penning-Malmberg trap [46]. A sketch of three electrodes of such a trap is shown in Fig. 2.3[1]

In order to define a non-neutral plasma it is necessary to introduce the Debye length which given by

[1] In reality Penning-Malmberg traps consist of more electrodes, e.g. the Cusp trap is made up of 22 electrodes. However, the plasma confinement typically happens in a smaller region of the trap, which is indicated in the figure.

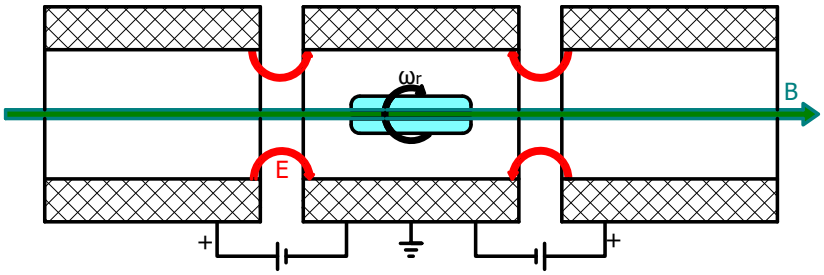

Figure 2.3: Cross-sectional view of a sketch of three electrodes of a Penning-Malmberg trap with a plasma (light blue) rotating around the center of the trap with a rotation frequency of ω_r. The magnetic field (green) is parallel to the electrode axis. The electric field (red) is produced by potentials applied to the electrodes. Adapted from [47].

$$\lambda_D = \sqrt{\frac{\epsilon_0 k_\mathrm{B} T}{n e^2}}, \tag{2.11}$$

with T being the temperature and n the number density of the particles in the trap. The Debye length describes the self-shielding of the particles due to their electric charge. A cloud of particles is defined as a plasma if (i) the radius of the ensemble r_p is much larger than the Debye length ($\lambda_D \ll r_\mathrm{p}$) and (ii) the number of charges in a Debye sphere, the sphere surrounding the charges outside of which the charges are electrically screened, is large ($n\lambda_D^3 \gg 1$). The plasma parameter $n\lambda_D^3$ can be rewritten as [47] $n\lambda_D^3 = \left[k_\mathrm{B}T/(e^2/\epsilon_0 a)\right]^{3/2}$, with $a = n^{-1/3}$. Hence, it is proportional to the ratio of the mean kinetic energy of a particle and the interaction potential between nearest neighbours. For a state defined as a plasma, this ratio has to be large and therefore it can be described as a nearly ideal gas of weakly-interacting particles. If this requirement is not fulfilled, the plasma is referred to as strongly-coupled. At the same time, (i) means that a plasma is essentially shielded from external perturbation fields and hence shows a collective response to those as opposed to a simple ionised gas where no shielding is provided, and individual particles interact one-to-one with each other and with the external fields. Further, if the net charge of the particles is non-zero it is called a non-neutral plasma, which is the case for a single-component electron or positron plasma.

When a large number of particles with the same electric charge is confined in a trap it is advantageous to use the charge distribution over the volume of the plasma - the space charge ϕ_s - rather then individual point charges. In a Penning-Malmberg trap the equilibrium distribution of particles in a non-neutral plasma is roughly cylindrical. In this case, an estimate of the space charge potential is obtained, which is valid for high aspect ratios $L_\mathrm{p}/r_\mathrm{p}$, with L_p being the plasma length and r_p the plasma radius [48]

$$\phi_\mathrm{s} = \frac{q n r_\mathrm{p}^2}{2\epsilon_0}\left(\ln\frac{r_\mathrm{w}}{r_\mathrm{p}} + \frac{1}{2}\right), \tag{2.12}$$

where r_w is the radius of the electrode, and n the number density. The space charge potential adds up to the external potential produced by the electrodes, hence altering the particle motion in the confinement volume according to the change in the potential.

2.2.1 Plasma properties

It is impossible to calculate the trajectories of all particles in a high-density non-neutral plasma, hence a collective description of the motion is adopted. A fully kinetic description is not necessary in a regime of high magnetisation, and a fluid-element approach is taken into account [47, 49].

In this approach the plasma is seen as a fluid which can be divided into infinitesimal small elements in which all particles move together with an average velocity $\vec{u}$, leading to the fluid equation

$$mn\frac{\mathrm{d}\vec{u}}{\mathrm{d}t} = qn(\vec{E} + \vec{u} \times \vec{B}), \tag{2.13}$$

where m is the mass of the particle, n the number density, q the elementary charge, and $\vec{E}$ and $\vec{B}$ the electric and magnetic field, respectively. For simplicity, a transformation into a coordinate system co-moving with the fluid element is performed. In this co-moving frame, the time derivative of the velocity of the fluid changes to

$$\frac{\mathrm{d}\vec{u}(\vec{x},t)}{\mathrm{d}t} = \frac{\partial\vec{u}}{\partial t} + (\vec{u}\cdot\vec{\nabla})\vec{u}, \tag{2.14}$$

which, when inserted into Eq. (2.13), yields the equation of motion in the new frame

$$mn\left[\frac{\partial\vec{u}}{\partial t} + (\vec{u}\cdot\vec{\nabla})\vec{u}\right] = qn(\vec{E} + \vec{u} \times \vec{B}). \tag{2.15}$$

Because of thermal motions a pressure force has to be added to the equation of motion. This force is due to particles randomly moving in and out of the fluid element. Hence, the full equation of motion, assuming an isotropic fluid, is

$$mn\left[\frac{\partial\vec{u}}{\partial t} + (\vec{u}\cdot\vec{\nabla})\vec{u}\right] = qn(\vec{E} + \vec{u} \times \vec{B}) - \vec{\nabla}p, \tag{2.16}$$

where $p = nk_\mathrm{B}T$.

Temperature

Assuming thermal equilibrium, the velocity of particles in a gas follows a Maxwell-Boltzmann distribution. In the one dimensional case the distribution is

$$f(u) = Ae^{-\frac{1}{2}\frac{mu^2}{k_\mathrm{B}T}}, \tag{2.17}$$

and $f\mathrm{d}u$ is the number of particles with velocities between u and $u+\mathrm{d}u$. Integrating the distribution over $\mathbb{R}$ gives the number density n

$$n = \int_{-\infty}^{\infty} f(u)\mathrm{d}u, \tag{2.18}$$

yielding for the normalisation coefficient A

$$A = n\sqrt{\frac{m}{2\pi k_\mathrm{B}T}}. \tag{2.19}$$

Calculating the average kinetic energy E_avg as

$$E_\mathrm{avg} = \frac{\int_{-\infty}^{\infty} \frac{1}{2}mu^2 f(u)\mathrm{d}u}{\int_{-\infty}^{\infty} f(u)\mathrm{d}u}, \tag{2.20}$$

which, by introducing the thermal velocity $v_\mathrm{th} = (2k_\mathrm{B}T/m)^{1/2}$ and $y = u/v_\mathrm{th}$, results in

$$E_\mathrm{avg} = \frac{1}{2}k_\mathrm{B}T. \tag{2.21}$$

As a plasma is confined radially by a magnetic field, it can have two different Maxwellian distributions: one parallel, and one perpendicular to the magnetic field with temperatures $\mathrm{T}_\parallel$ and $\mathrm{T}_\perp$, respectively. In a non-collisional plasma transverse (radial) and parallel (axial) motions affected and unaffected respectively by the magnetic part of the generalised Lorentz force, are ideally decoupled and different equilibrium temperatures can be attained. A unique temperature is reached when motions are coupled, either by collisions or asymmetries or active manipulation of the sample.

Number density & plasma rotation frequency

It is assumed that a trapped non-neutral plasma cylinder has reached a thermal equilibrium state. In that state the plasma fluid elements rotate around the symmetry axis with a constant frequency of ω_r and the plasma is a time-independent fluid which can be defined in cylindrical coordinates as $\vec{u}(r) = -\omega_\mathrm{r} r\hat{\Theta}$ [47]. The z-component of Eq. (2.16)

$$qnE_z - \frac{\partial n}{\partial z}k_\mathrm{B}T = 0 \tag{2.22}$$

is a differential equation for the density. The solution of which is

$$n(r,z) = n_0(r)e^{\frac{q\phi(r,z)}{k_\mathrm{B}T}}. \tag{2.23}$$

Using cylindrical coordinates the radial component of Eq. (2.16) is

$$-mn\omega_\mathrm{r}^2 r = -qn\left(\frac{\partial\phi}{\partial r} + B\omega_\mathrm{r} r\right) - k_\mathrm{B}T\frac{\partial n}{\partial r}. \tag{2.24}$$

Inserting Eq. (2.23) into the equation of motion Eq. (2.16) yields

$$k_\mathrm{B}T\frac{\partial n_0}{\partial r} = -m\omega_\mathrm{r} n_0 r\left(\frac{qB}{m} - \omega_\mathrm{r}\right), \tag{2.25}$$

where the first term in the brackets of the RHS is the cyclotron frequency $\omega_c = \frac{qB}{m}$. Solving this differential equation leads to the density

$$n(r,z) = Ce^{-\frac{q\left[\phi(r,z)+\phi_{\text{eff}}(r)\right]}{k_B T}} \tag{2.26}$$

where $q\phi_{\text{eff}}(r) = \frac{1}{2}m\omega_r(\omega_c - \omega_r)r^2$ is the effective potential, which provides radial confinement due to the rotation, and C is a constant of integration. The system can be solved by finding $\phi(r,z)$ and the correlated boundary conditions from the electrodes and the Poisson equation

$$\nabla^2\phi(r,z) \equiv \frac{1}{r}\frac{\partial}{\partial r}\left(r\frac{\partial\phi(r,z)}{\partial r}\right) = -\frac{qn(r,z)}{\epsilon_0}. \tag{2.27}$$

Without knowing the electrode potential it is possible to solve the Poisson equation for the effective potential only, yielding

$$n_o = 2\frac{m\epsilon_0}{q^2}\omega_r(\omega_c - \omega_r) \tag{2.28}$$

The solutions to Eq. (2.26) and the Poisson equation show that the plasma density n_0 is uniform within the plasma and falls to zero at the surface within a few Debye lengths. This can only hold if the plasma length and radius are larger than the Debye length.

From Eq. (2.28) it is possible to get an expression for the plasma rotation frequency ω_r

$$\omega_r^{\pm} = \frac{\omega_c}{2} \pm \sqrt{\frac{\omega_c^2}{4} - \frac{q^2 n_0}{2m\epsilon_0}} \tag{2.29}$$

which means that the plasma rotates at a constant frequency, independent of the radial position.

2.2.2 Plasma manipulation

Evaporative Cooling - EVC

As mentioned above, the temperature of a plasma in thermal equilibrium follows a Maxwell-Boltzmann distribution. This means that a small fraction of the particles have a high energy. By releasing this energetic fraction the mean kinetic energy of the remaining particles decreases. This technique has been used for neutral atoms [50], and it was shown to work for non-neutral plasmas [51].

In this technique the trapping potential is slowly decreased such that the higher energy particles can leave the trap while the lower energy ones remain trapped. This is in principle achieved by limiting the depth of the potential to $V_d = \eta k_B T$, where η is the ratio of the potential well depth and $k_B T$. The rate at which particles escape is the same as the production rate of particles with an energy greater than V_d. In a system in

equilibrium the production rate of particles with energy greater than V_d is the number of particles in the high energy tail of the distribution multiplied by the elastic collision rate $n_0 \cdot \sigma_\mathrm{el} \cdot v_\mathrm{th}$, where n_0 is the density, σ_el is the elastic scattering cross section, and v_th is the average thermal velocity. Hence, one can write the rate of evaporation to be [50]

$$\frac{\mathrm{d}N}{\mathrm{d}t} = -N n_0 \sigma_\mathrm{el} v_\mathrm{th} \eta e^{-\eta} = -\frac{N}{\tau_\mathrm{ev}}, \tag{2.30}$$

where τ_ev is the time constant for evaporation and N is the number of particles. The change in temperature and number of particles during evaporative cooling is described by the two differential equations

$$\frac{\mathrm{d}N}{\mathrm{d}t} = -\frac{N}{\tau_\mathrm{ev}}, \tag{2.31}$$

$$\frac{\mathrm{d}T}{\mathrm{d}t} = -\alpha\frac{T}{\tau_\mathrm{ev}}, \tag{2.32}$$

and α being

$$\alpha = \frac{\mathrm{d}\ln T}{\mathrm{d}\ln N}, \tag{2.33}$$

which describes the temperature reduction per particle loss.

Cyclotron Cooling

Light particles, such as electrons or positrons, cool in a strong magnetic field by cyclotron radiation. For a Maxwell-Boltzmann distribution the average change in temperature by cyclotron cooling is

$$\frac{\mathrm{d}T_\perp}{\mathrm{d}t} = -\frac{3T_\perp}{2\tau_\mathrm{r}}, \tag{2.34}$$

with the radiation time τ_r (assuming two out of three dimensions radiate in a strong axial magnetic field [52])

$$\tau_\mathrm{r} = \frac{9}{2}\frac{\pi\epsilon_0 m^3 c^3}{q^4 B^2}. \tag{2.35}$$

For electrons or positrons τ_r is therefore

$$\tau_{\mathrm{r},e^\pm} \sim \frac{3.86\ \mathrm{s}}{B[\mathrm{T}]^2}. \tag{2.36}$$

As the radiation time scales with the mass cubed, this effect is negligible for heavier particles. For example, the radiation time for an antiproton is

$$\tau_{\mathrm{r},\overline{\mathrm{p}}} \sim \frac{24 \cdot 10^9\ \mathrm{s}}{B[\mathrm{T}]^2}. \tag{2.37}$$

Electron Cooling

In order to cool heavier particles such as antiprotons, which were caught in a Penning-Malmberg trap, a different approach than evaporative cooling can be used which does not reduce the - for antiprotons already low - number of particles. A low temperature electron plasma, which is achieved by the cooling methods described above, is prepared in the trap. Hot antiprotons will lose energy via collisions with the cold electrons with a rate of [53]

$$\frac{\mathrm{d}T}{\mathrm{d}t} = \frac{T_\mathrm{e} - T_\mathrm{p}}{\tau_\mathrm{eq}}, \tag{2.38}$$

where T_e is the temperature of the electrons and T_p the temperature of the antiprotons, with a characteristic time at which equipartition of the energy is established between the two ensembles τ_eq of [53, 54]

$$\tau_\mathrm{eq} = \frac{3 m_\mathrm{p} m_\mathrm{e} c^3}{8\sqrt{2\pi} n_\mathrm{e} e^4 \ln\Lambda} \left(\frac{k_\mathrm{B} T_\mathrm{p}}{m_\mathrm{p} c^2} + \frac{k_\mathrm{B} T_\mathrm{e}}{m_\mathrm{e} c^2} \right)^{3/2}, \tag{2.39}$$

where m_p and m_e are the masses of the antiproton and electron, respectively, n_e is the electron density and Λ is the ratio of the Debye length to the minimum impact parameter

$$\Lambda = \frac{4\pi}{\sqrt{n_\mathrm{e}}} \sqrt{T_\mathrm{e}} \left(T_\mathrm{e} + \frac{T_\mathrm{p}}{1836} + \frac{\sqrt{T_\mathrm{p} T_\mathrm{e}}}{21} \right). \tag{2.40}$$

The Coulomb logarithm $\ln\Lambda$, which is related to the Debye shielding of the Coulomb force has typical values of 10-20 [54].

The main limitation of this cooling technique is how fast the electrons can dissipate the energy gained from the antiprotons. Therefore, one can look at the electrical resistivity η, which is the ratio of the rate at which electrons gain momentum by the impact of antiprotons and the current density [54]. For the simplified case that electrons do not interact with each other and the antiprotons are at rest, i.e. for a Lorentz gas, it is possible to derive the resistivity as

$$\eta_L = \frac{\pi^{3/2} m_\mathrm{e}^{1/2} Z e^2 c^2 \ln\Lambda}{2(2 k_\mathrm{B} T)^{3/2}} \tag{2.41}$$

which is referred to as the Spitzer collision rate [54].

Rotating wall technique - RW

The total canonical angular momentum of a non-neutral plasma, which in a strong magnetic field is approximately $P_\theta \approx \sum_j qBr_j^2/(2c)$[55], is conserved. That means that particles moving outwards from the plasma, i.e. increasing r_j, must be compensated by particles moving inwards, i.e. reducing r_j. As a consequence the plasma will relax towards an equilibrium state. However, in reality the trap has imperfections and residual

gas is present, these can lead to a change of total angular momentum, and to a decrease of the rotation frequency and consequently to a lower density, as shown in Eq. (2.29). The decrease in the rotation frequency, and hence the reduction in density, can be counteracted by injecting angular momentum into the plasma. This is typically achieved by using the rotating wall (RW) technique [55]. To increase the angular momentum one has to decrease the mean square radius $\langle r^2 \rangle$ (to decrease P_θ one has to increase $\langle r^2 \rangle$). This can be achieved by applying a rotating electric field with frequency $\omega_{\mathrm{RW}} > \omega_{\mathrm{r}}$ which introduces a torque τ_{RW} on the plasma. Compression is achieved when the torque of the rotating wall is larger than the ambient torque τ_{ambient}, i.e. that of the natural angular momentum in the absence of external forces,

$$|\tau_{\mathrm{RW}}| \geq |\tau_{\mathrm{ambient}}|. \tag{2.42}$$

The rotating electric field is generated by a time-varying potential applied to azimuthally sectored electrodes, as shown in Fig. 2.4. The potential on each sector ϕ_j is given by [47]

$$\phi_j(\theta, t) = A_{\mathrm{RW}} \cos\left[m_\theta(\theta_j - \omega_{\mathrm{RW}} t)\right], \tag{2.43}$$

$$\theta_j - \frac{\Delta\theta}{2} < \theta < \theta_j + \frac{\Delta\theta}{2}, \tag{2.44}$$

with the amplitude of the sinusoidal perturbation applied to each segment A_{RW}, a phase shift of θ_j (as indicated on the right hand side of Fig. 2.4 for a four-fold segmented electrode, i.e. $j = 4$), and a frequency of ω_{RW}. The quantity m_θ represents the azimuthal multipole order of the drive, e.g. $m_\theta = 1$ is a dipole drive (typically used in the ASACUSA experiment), while $m_\theta = 2$ would be a quadrupole drive.

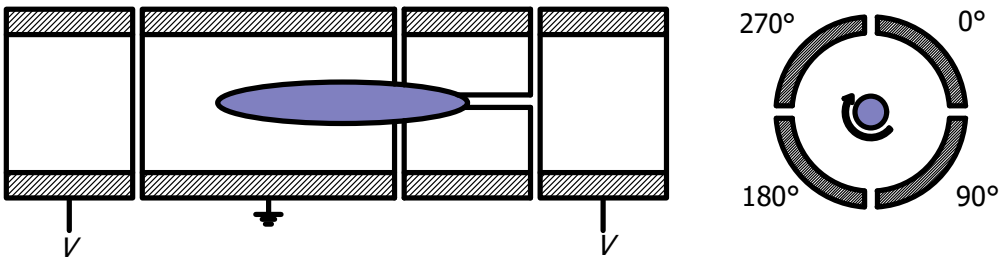

Figure 2.4: Left: Sketch of a Penning trap with a azimuthally split electrode for the application of a RW. Right: Front view of a fourfold segmented electrode and labelled phase shift of the dipole perturbation.

A side-effect of the RW is heating of the plasma due to the excitation of plasma

modes [56]. To counteract this effect it is necessary to cool the plasma with one of the techniques described above.

It is important to note that the RW technique works in the single particle regime as well [57]. For example, in the case of positron trapping in a buffer gas trap, which will be described in more detail in the subsequent chapters, the RW can be used to compress the particle cloud during accumulation. It was shown that good compression in the independent particle regime can be achieved when the RW frequency is smaller than or equal to the axial frequency, i.e. $\omega_{\mathrm{RW}} \leq \omega_z$ [57].

Strong drive regime - SDR

At low amplitudes of the perturbation, the RW technique may be limited by coupling to the plasma, which is only possible to parts of the cylinder which are outside of the Debye shielding. This yields only discrete frequencies at which the plasma density increases [58], as shown as the hollow circles in Fig. 2.5. By increasing the amplitude of the drive it is possible to couple the RW to the plasma rotation frequency which results in a linear increase of the plasma density over a wide range of the RW frequency ω_{RW}, which is called the Strong Drive Regime [58]. This increase in the density continues until the difference between the RW frequency and the plasma rotation frequency is small, hence $\omega_{\mathrm{RW}} \approx \omega_{\mathrm{r}}$ for SDR. Figure 2.5 shows the density and plasma rotation frequency as functions of the RW frequency. The steps visible in the black data set are due to coupling of plasma modes to static trap asymmetries producing a drag on the plasma, which can be overcome by increasing the RW frequency.

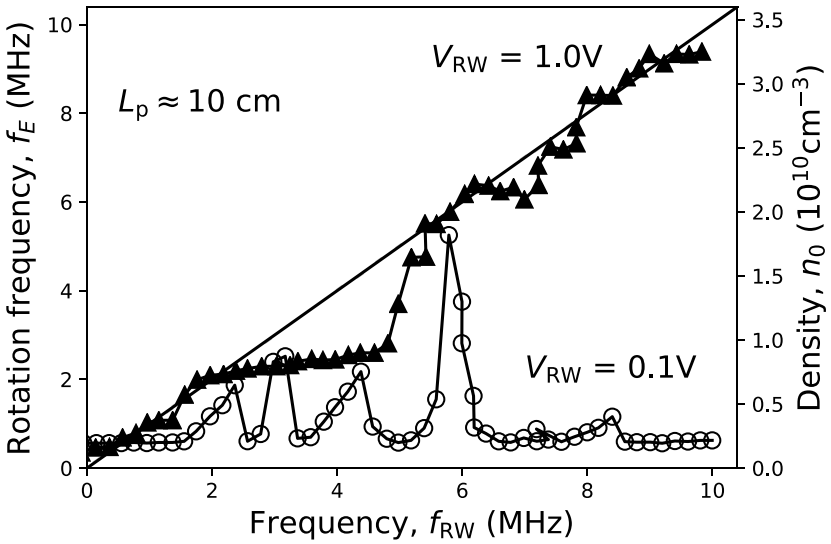

Figure 2.5: Steady-state density as a function of RW frequency (f_{RW}) for a plasma of length 10 cm at a RW amplitude of 1 V (triangles) and 0.1 V (hollow circles). The black solid line is the case $\omega_r = \omega_{RW}$. Adapted from [59].

SDREVC

It is crucial to have a technique which yields the same initial plasma properties prior to the production of antihydrogen, minimising possible fluctuations in the number of particles, temperature and density. In 2018, the ALPHA collaboration reported a novel technique to achieve reproducible properties over a wide range of the initial number of particles and densities, by combining EVC and SDR in the "Strong Drive Evaporative Cooling" (SDREVC) technique [60, 61]. In this technique the plasma space charge potential, as shown in Eq. (2.12), is controlled by EVC while simultaneously applying a RW to set the plasma density. For this method to work it is necessary to find adequate potential well shapes such that the compression in the SDR is possible over the whole range of confinement potential changes due to EVC. Figure 2.6 shows the final number of particles (top plot) and the density (central plot) as functions of the initial number of particles for no manipulation (black triangles), after EVC (red dots) and after SDREVC (orange downward triangle). Additionally, the bottom plot shows the final density as a function of the initial density. The shot-to-shot variations of the final properties could be reduced to about 1 % in the ALPHA experiment, which is described as the precision limit of the measurement technique applied.

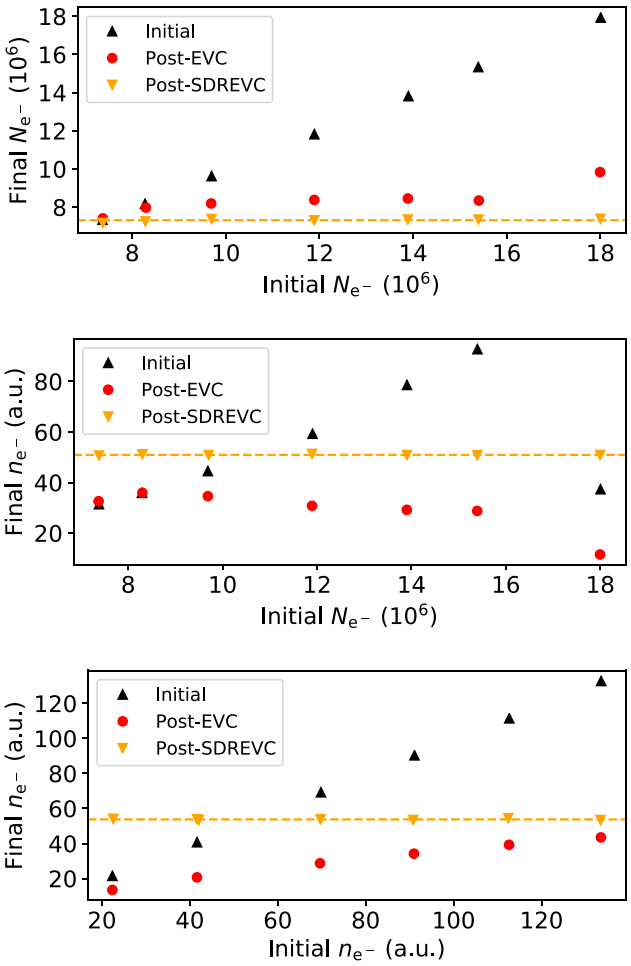

Figure 2.6: Final number (top) and density (middle) of the electron plasma as a function of of the initial number of electrons measured by the ALPHA collaboration before perturbation (black triangles), after EVC (red dots) and after SDREVC (orange downward triangle). The bottom plot shows the final density as a function of the initial density. The horizontal dashed line indicates the mean of the SDREVC data. Adapted from [60].

2.3 Antihydrogen production

Current experiments at the AD attain antihydrogen synthesis in Penning-Malmberg traps following two different routes: three-body recombination ($e^+ + e^+ + \overline{p} \rightarrow \overline{H}^* + e^+$) and charge exchange with a positronium atom (PS) ($Ps^* + \overline{p} \rightarrow \overline{H}^* + e^-$). Further, radiative recombination ($e^+ + \overline{p} \rightarrow \overline{H}^* + h\nu$) is possible. In the following subsection the focus lies on the three-body recombination technique, as it is the dominant process in the ASACUSA-Cusp experiment; details on the other processes can be found elsewhere (e.g. [62–64]). Additionally, the relation between the principal quantum number distribution of the produced antihydrogen atoms, and the temperature and density of the positron plasma will be described in more detail.

2.3.1 Three-body recombination

For three-body recombination it is necessary that two positrons are in close proximity to one antiproton. One positron and the antiproton form an antihydrogen atom, and the binding energy is taken away by the other positron. This is typically achieved by mixing positron and antiproton plasmas, which means that the potentials of the trap confining the positrons and antiprotons in adjacent regions with opposite potential concavity are slowly changed, to introduce an overlap of the particles. The theoretical rate at which antihydrogen is produced is given by [65, 66]

$$R_{\mathrm{tbr}} = Cn^2 v b^5 \propto n^2 T^{-9/2}, \tag{2.45}$$

where n is the positron number density, v is the thermal velocity of the positrons, $b = e^2/(4\pi\epsilon_0 k_{\mathrm{B}} T)$ is the impact parameter, and C is a dimensionless coefficient weakly depending on the positron temperature and magnetic field strength [64, 66, 67]. As can be seen, the rate for three-body recombination is highly dependent on the temperature and the density of the positrons. However, this expression does not describe in which state the atoms are produced, hence it is important to look at the scaling behaviour of the principal quantum number.

2.3.2 Energy level population

The principal quantum number n of an atom produced by three-body recombination is inversely proportional to the temperature of the positrons $n \propto T^{-1/2}$. Hence, the lower the positron energy, the weaker the positron is bound to the antiproton. However, the atoms spend time in the positron plasma after production, and additionally have a time-of-flight to the detector. This means that the atoms can undergo several other processes which can change the principal quantum number such as collisional (de)excitation, ionisation, spontaneous radiative decay, and stimulated radiative transition due to black body radiation. Previously, Monte Carlo simulations were performed to examine the dependence of the principal quantum number distribution on the positron plasma density

and temperature, taking these interactions into account [68].

The simulation modeled 10^6 antiprotons mixed with a positron plasma with a temperature between 20 K and 300 K, and a density of $10^{14}\,\mathrm{m}^{-3}$ to $10^{16}\,\mathrm{m}^{-3}$. Two scenarios were simulated: (i) the antihydrogen atoms were allowed to spend 10 μs in the positron plasma after the production, and (ii) the antihydrogen atoms were allowed to spend 10 μs in the plasma and then a 1 ms time-of-flight outside the plasma. The left and right plot of Fig. 2.7 show contour plots of the number of ground-state antihydrogen atoms as a function of the positron plasma density and temperature for case (i) and (ii), respectively. It is clearly visible that the lower the temperature and the higher the density of the positron plasma, the larger the number of ground-state antihydrogen atoms exiting the plasma (or reaching the detector). This is due to the fact that for low positron temperatures the principal quantum number of the atoms produced is high, but so is the three-body recombination rate, i.e. more atoms are produced than for a high temperature positron plasma. By additionally having a high positron density, it is more likely for atoms to undergo collisional de-excitation, hence when they leave the plasma, the principal quantum number is lower.

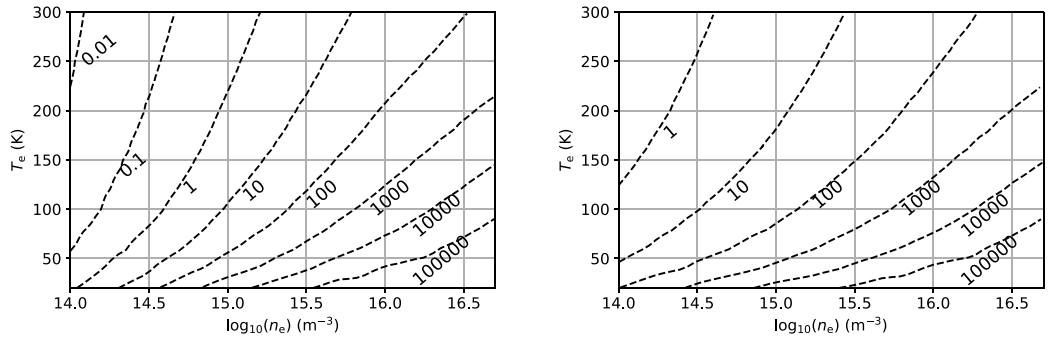

Figure 2.7: Contour plot of the number of ground-state antihydrogen atoms as a function of positron temperatures and densities after 10 us interaction in positron plasma only (left) and after additional 1 ms time-of-flight outside the plasma (right), adapted from [68].

Further, the authors looked at the scaling behaviour of the principal quantum number distribution which for three-body recombination shown in Eq. (2.45), is proportional to $n^2T^{-9/2}$. The simulations looked at the number of ground-state antihydrogen atoms as a function of positron temperature for different densities, as shown in Fig. 2.8(a) and Fig. 2.8(c) for case (i) and (ii), respectively. The simulations were repeated for the number of ground-state antihydrogen atoms as a function of positron density at different temperatures, as shown in Fig. 2.8(b) and Fig. 2.8(d) for case (i) and (ii), respectively.

The simulated scaling behaviour for the ground-state atoms was found to differ from the theoretical result in Eq. (2.45), depending on the density and temperature. As examples for the three-body recombination scaling behaviour the authors showed that a positron plasma at room temperature has a density dependence of only $n^{1.6}$, and at a density of $10^{14}\,\mathrm{m}^{-3}$ a temperature dependence of $T^{-2.0}$. For higher densities and lower

temperatures the scaling approaches the case for only three-body recombination. This indicates that at low temperatures and high densities three-body recombination is the dominant influence on the principal quantum number, while at higher temperatures and lower densities other processes (like collisional (de)excitation and radiative processes) play significant roles.

To conclude this section, it is important to stress the low temperature - high density region of the simulations. At a positron density of $10^{14}\,\mathrm{m}^{-3}$ decreasing the temperature by one order of magnitude increases the number of ground-state antihydrogen atoms by two orders of magnitude. Similarly, by increasing the density an increase in the ground-state fraction can be achieved.

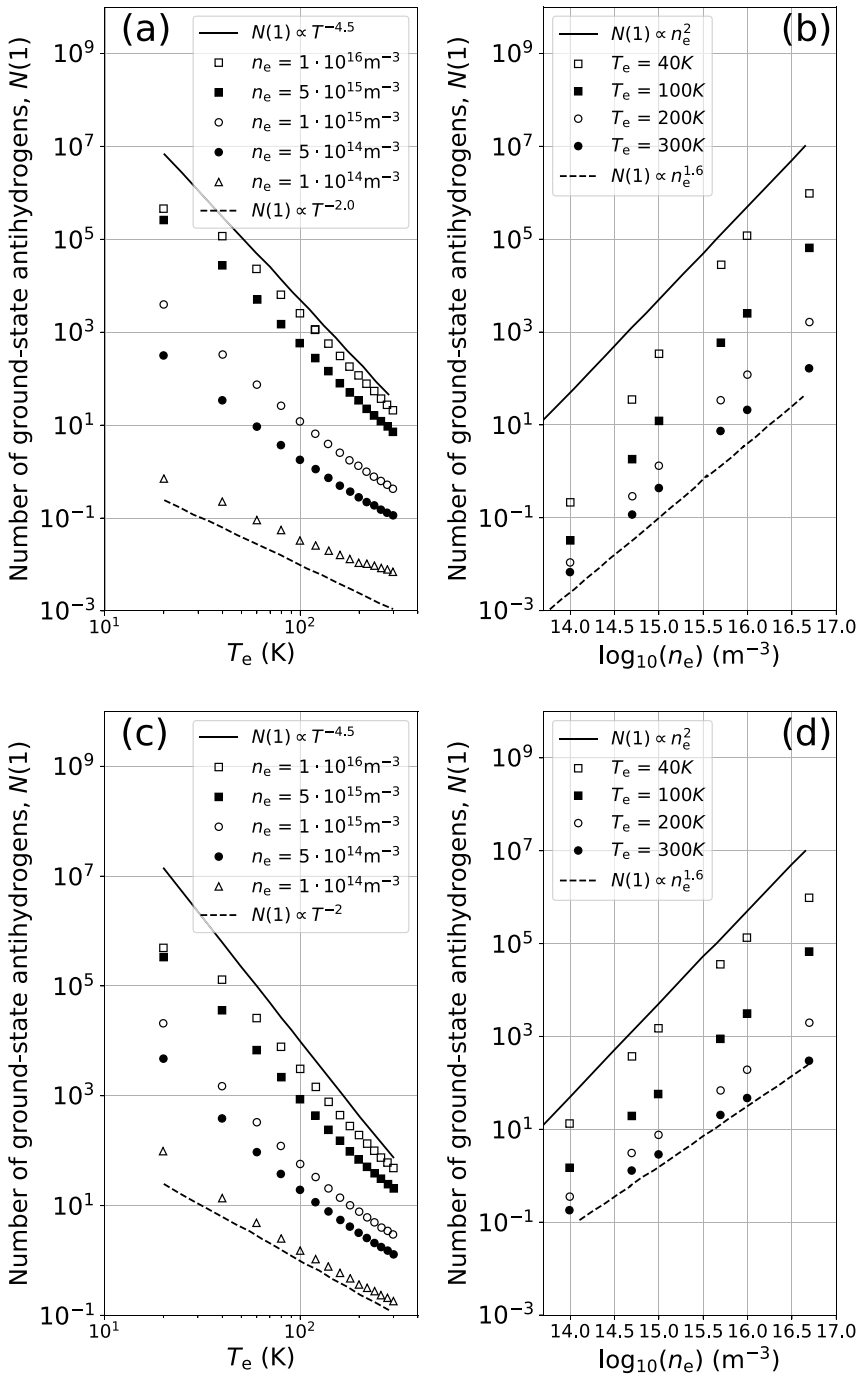

Figure 2.8: Simulated number of ground-state antihydrogen atoms as a function of positron temperatures (a,c) and density (b,d) at different densities and temperature, respectively. The simulated results are given for scenario (i) (top) and (ii) (bottom) as described in the text. The solid line ($\propto n_e^2 T_e^{-4.5}$) and dashed line ($\propto n_e^{1.6} T^{-2}$) are indicated for reference. All data are adapted from [68].

Chapter 3

Experimental setup

This chapter describes the setup of the ASACUSA-Cusp experiment and the working principles of the individual apparatuses. A more detailed discussion of the procedures used to acquire data will be given in the subsequent chapters.

The experiment can be divided into four sections:

- Positron system: rare-gas moderator (RGM), buffer gas trap (BGT) and the accumulator,
- Antiproton system: antiproton trap (MUSASHI) and drift tube,
- Mixing trap (Cusp trap),
- Spectroscopy beamline: microwave cavity, analysing sextupole magnet and antihydrogen detector.

Furthermore, the low-energy proton source, which can be installed into the experiment to perform matter mixing studies, will be described. A scale drawing of the experiment is shown in Fig. 3.1.

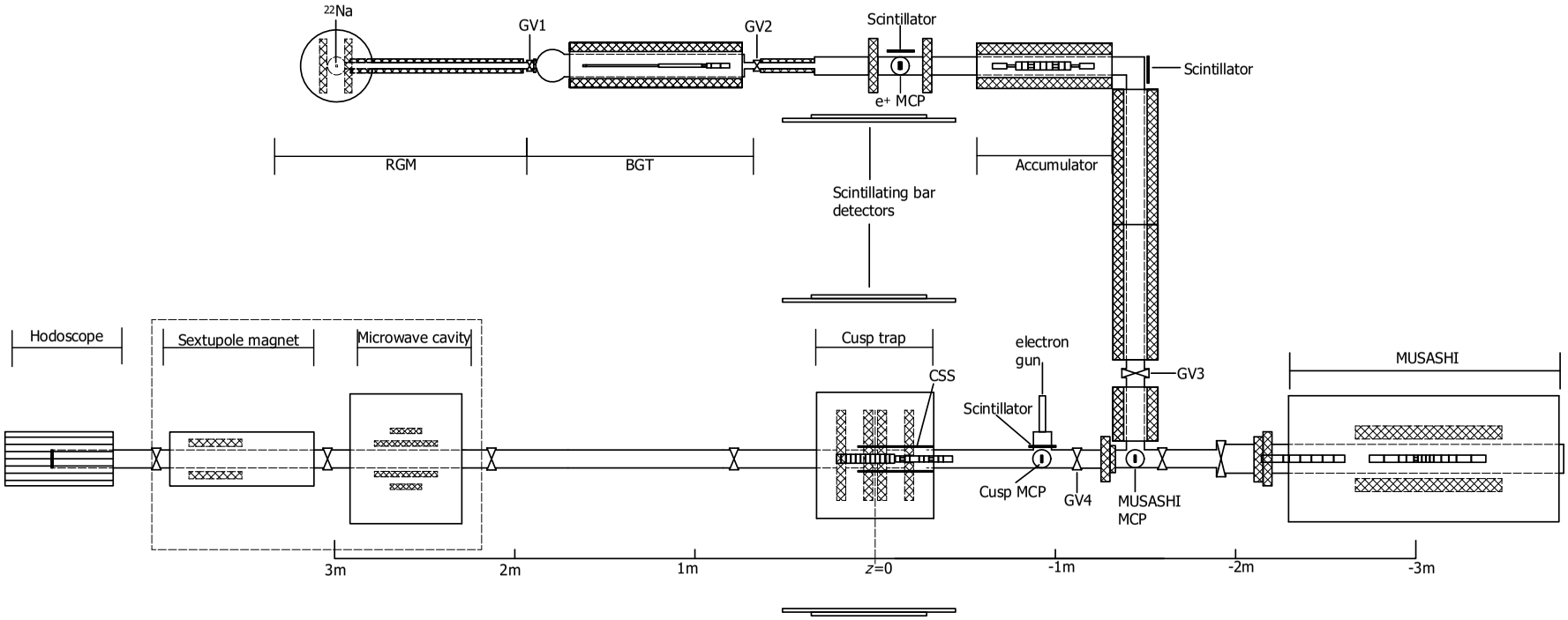

Figure 3.1: Scale drawing of the experimental setup. The magnets are indicated with cross hatching and are magnified for visibility. The electrodes of the traps are shown in their position within the magnets. The detector labeled "scintillator" is moved along the beamline, indicated are the three used locations. One out of four panels of the scintillating bar detectors is not shown. The microwave cavity and the sextupole magnet were not installed in the course of this work (indicated as dashed rectangle) and the hodoscope was installed right after the GV after the Cusp trap. Additionally, the $z = 0$ position in the Cusp trap is indicated.

3.1 Positron System

In this section the positron system, consisting of a commercial RGM and BGT from First Point Scientific Inc. (FPS) previously used at Aarhus University and the accumulator, is described. These apparatuses replaced a previous RGM and BGT [69]. After a general introduction to RGM systems and BGTs, the individual setups are discussed in more detail.

3.1.1 Rare-Gas Solid Moderator

Positrons are produced by a commercial ^{22}Na source manufactured by iThemba-labs. ^{22}Na is a suitable source for positron experiments because the only possible decay processes are β^+-decay ($\sim 90\,\%$) and electron capture ($\sim 10\,\%$) into ^{22}Ne with a half life of 2.6 years. The calculated energy spectrum of the emitted positrons is shown in Fig. 3.2.

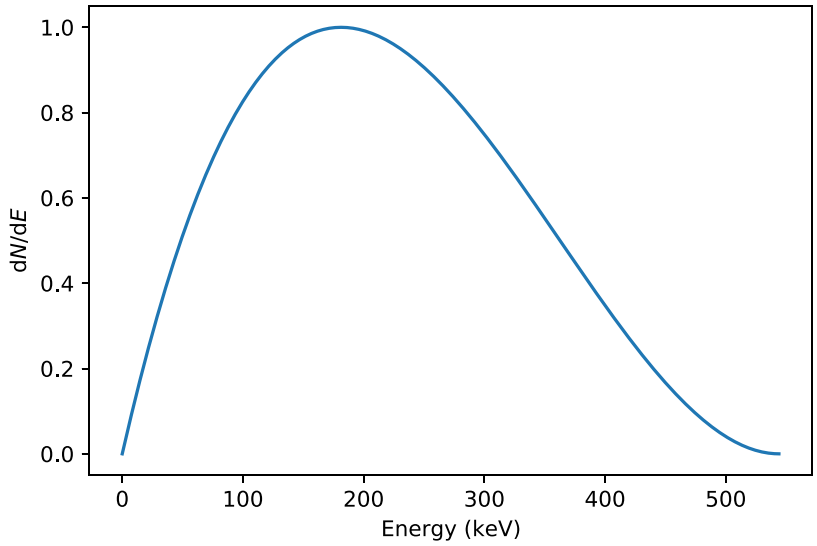

Figure 3.2: Calculated energy spectrum of the positrons emitted from a ^{22}Na source normalised to the maximum value.

In order to trap the particles emitted from the source, they have to lose energy and form a beam. This process is referred to as "moderation" and is typically achieved with a rare-gas (Ne, Xe, Ar or Kr) solid moderator. A more detailed description of the dynamics of positrons in Xe, Kr and Ar is given in [70] and for Ne in [71]. This technique requires a thin layer (order of hundreds of nm to a few μm) of the rare-gas frozen onto an electrode in front of the source. Unlike in most metals, the work function for positrons in these insulator materials is positive. As a result, if the positron energy decreases below the work function, it gets trapped in the material. Initially, positrons from the ^{22}Na source lose energy by ionisation and electronic excitations of the moderator material.

At lower energies when a positron interacts with an electron in the solid, it can excite it from the valence band to the conduction band and produce an electron-hole pair, an exciton - i.e. a bound state between the electron and the hole - or positronium - a bound state of a positron and an electron. Due to the large band gap of the insulator ($E_g = 21.5\,\text{eV}$ [71]), there is a minimum energy threshold for these interactions, below which the only possible energy loss mechanism is phonon excitation - i.e. a collective excitation of vibrational energy of the lattice. As the maximum energy of phonons is small, the energy loss rate of positrons is slow but the diffusion rate is high, yielding a high probability of re-emission from the solid before the energy falls below the work function and the positron gets trapped [70, 71].

The efficiency of a moderator can be defined as $\varepsilon_M = N_s/A$, where N_s is the number of moderated positrons and A is the activity of the source. Efficiencies of up to 0.7 % were achieved by using solid Ne moderators [71].

Setup at CERN

A sketch of the setup of the RGM of the positron system is shown in the top drawing of Fig. 3.3. The ^{22}Na source is housed in a conical electrode, as sketched in the bottom drawing of Fig. 3.3, attached to the 4 K stage of a cryo cooler (Advanced Research Systems DE-204). The Ne gas is fed into the system via a small metal pipe. The electrode is surrounded by a heat shield made of aluminium and blocks of elkonite (CMW100), an alloy consisting of 45 % copper and 55 % tungsten, which is an in-vacuum radiation shield. The vacuum chamber is surrounded by a cylindrical container filled with small ($\sim 3\,\text{mm}$ diameter) lead balls to provide additional shielding.

A 30 cm long elkonite round tube is inserted downstream (DS) of the source chamber. The tube consists of three parts: a 13 cm long section with an inner diameter (ID) of 1 cm, a 10 cm long part with an ID of 3 cm and a 7 cm long part, with an ID of 0.8 cm which is 1 cm offset from the center of the vacuum chamber. A 20 cm long copper pumping restriction is installed at the end of the vacuum chamber, separated into one 15 cm long section with an ID of 1 cm which opens to a 5 cm long section with an ID of 3 cm.

The moderated positrons are magnetically guided from the source to the trap by two coils in a Helmholtz configuration ($B \sim 120\,\text{G}$), the beamtube solenoid ($B \sim 250\,\text{G}$) and are focused by an additional coil ($B \sim 175\,\text{G}$) into the trap. To pass the offset in the elkonite rod, two saddle coils produce a perpendicular field ($B \sim 23\,\text{G}$) to push moderated positrons off-center and back, while unmoderated positrons annihilate on the rod.

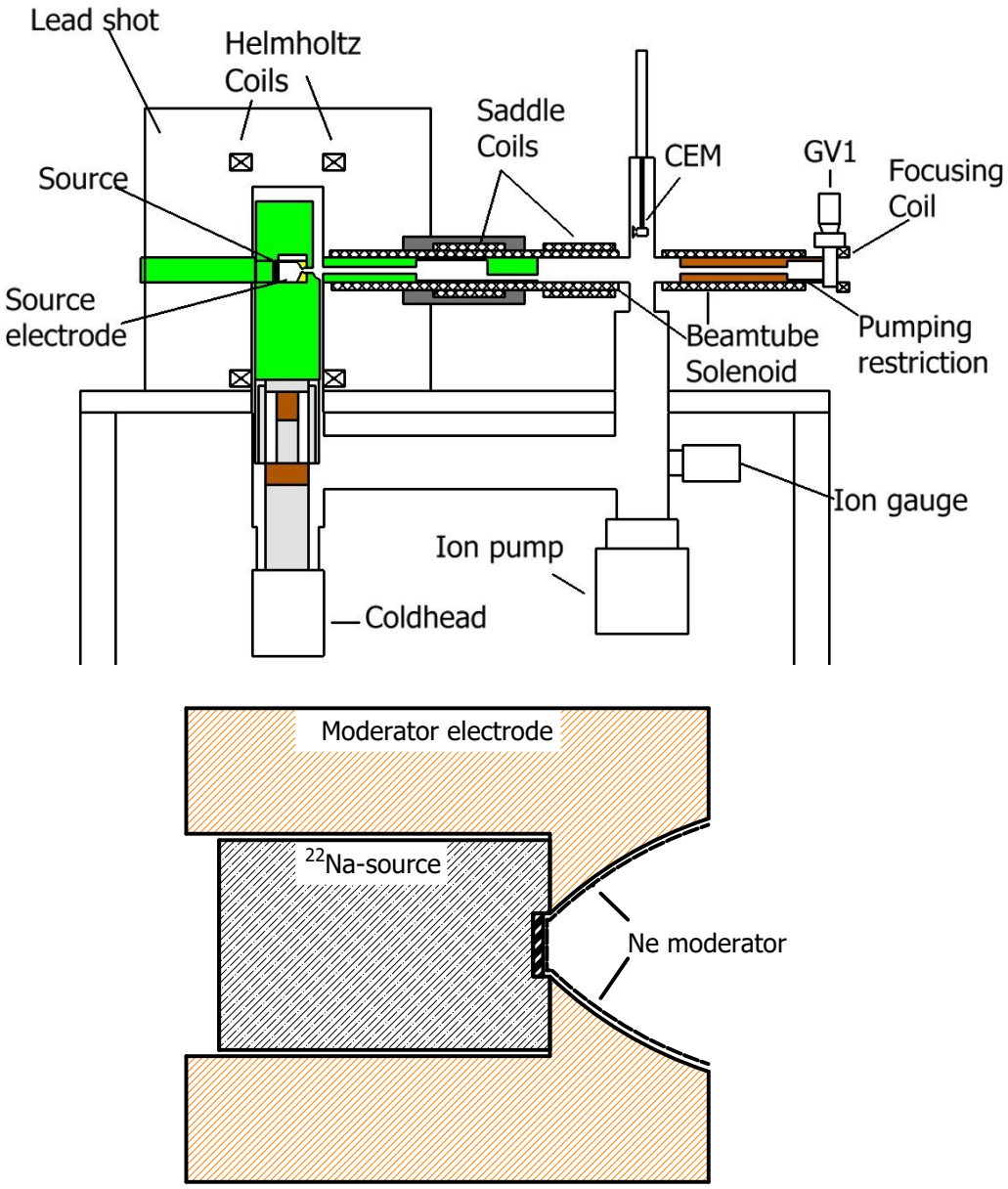

Figure 3.3: Top: Schematic drawing of the RGM-system. The magnets are indicated as cross-hatching. Elkonite is coloured in green, aluminium in light grey, lead in dark grey, and copper in brown.
Bottom: Sketch of the conical moderator electrode housing the ^{22}Na source. The frozen Ne is indicated as a dashed line.

3.1.2 Buffer Gas Trap

The buffer gas trap, a so-called Surko trap [72], is a modified Penning-Malmberg trap used for producing bunches of positrons. The positrons in the slow beam have to lose energy in order to be caught in an axial potential. Positrons lose energy by the excitation of the $a^1\Pi$ transition of molecular nitrogen [73]. The cross section for this transition peaks at around 10-12 eV as shown in Fig. 3.4 by the green downwards triangles. The

trap electrodes are designed such that a pressure gradient is produced, having high pressure in the first stage (order of 10^{-2}-10^{-3} mbar), a slightly decreased pressure in the second stage (order of 10^{-4} mbar) and a low pressure in the third stage, which is the trapping region (order of 10^{-5}-10^{-6} mbar). A simulation of the pressure using MOLFLOW+ [74] is shown in red in Fig. 3.5 in the subsequent section for the setup at CERN. The high pressure in the first stage is set such that the positrons have on average one collision in one single pass and cannot leave the trap because of an applied stepped potential, a simulation of which using COMSOL® [75] is shown in blue in Fig. 3.5. After several collisions in the first and second stage, the positrons have lost enough energy to be trapped in the third stage.

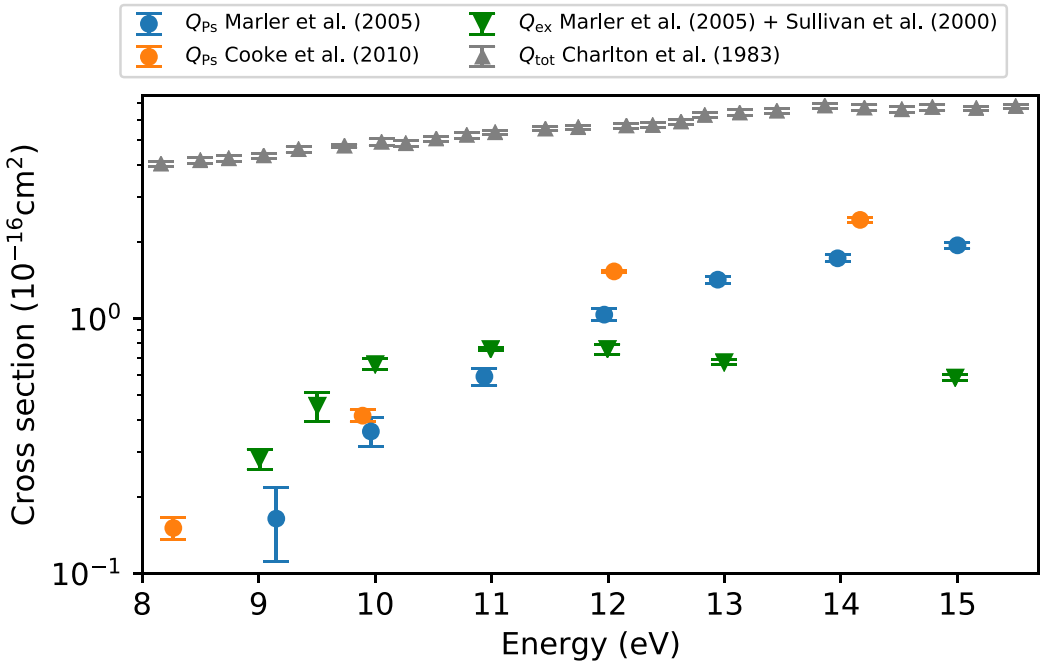

Figure 3.4: Measurements of the total scattering cross section (Q_{tot} from[76] - grey triangles), the positronium formation cross section (Q_{Ps} from [77] - blue dot - and from [78] - orange dot) and the cross section of the electronic excitation of the $a^1\Pi$ state (from [77] - green triangles) for low energy positrons in N_2.

The trapping efficiency can be defined as $\varepsilon_T = \frac{N_T}{N_s}$, where N_T is the number of trapped positrons and N_s is the number of moderated positrons. The main loss mechanism of this design during trapping is positronium formation, which has a threshold energy of ~ 8 eV in N_2, and the cross section of which is shown in Fig. 3.4 as orange and blue dots. The optimal step potential should be chosen such that the positron energy is in the range where the cross section for the electronic excitation is higher than for positronium formation, which is between 9-11 eV.

After being trapped the positrons still undergo collisions with the N_2 molecules. This leads to an expansion of the cloud and positrons are pushed outwards and annihilate

on the electrodes. To counteract the expansion a RW electric field is typically applied to increase the confinement time of positrons in the trap. However, positrons will eventually annihilate on the buffer gas, limiting the lifetime of trapped positrons. To speed up thermalisation and to reduce the energy spread of the bunch, a second gas, a cooling gas, is introduced into the trapping region. Typically CF_4 or SF_6 is chosen because of their high cross sections for vibrational and rotational excitations [79]. The advantage of using these gases is that positrons lose energy faster than using only N_2, reducing the time spent in the buffer gas, limiting annihilation. For CF_4, and similarly for SF_6, positrons with a temperature of up to 1700 K cool to room temperature within 50 ms, which is two orders of magnitude faster than for N_2[79].

Setup at CERN

A scale drawing of the BGT of the FPS system and simulations of the pressure (red) and on-axis potential (blue) are shown in Fig. 3.5. It consists of seven electrodes of varying length and inner diameter, as listed in Table 3.1.

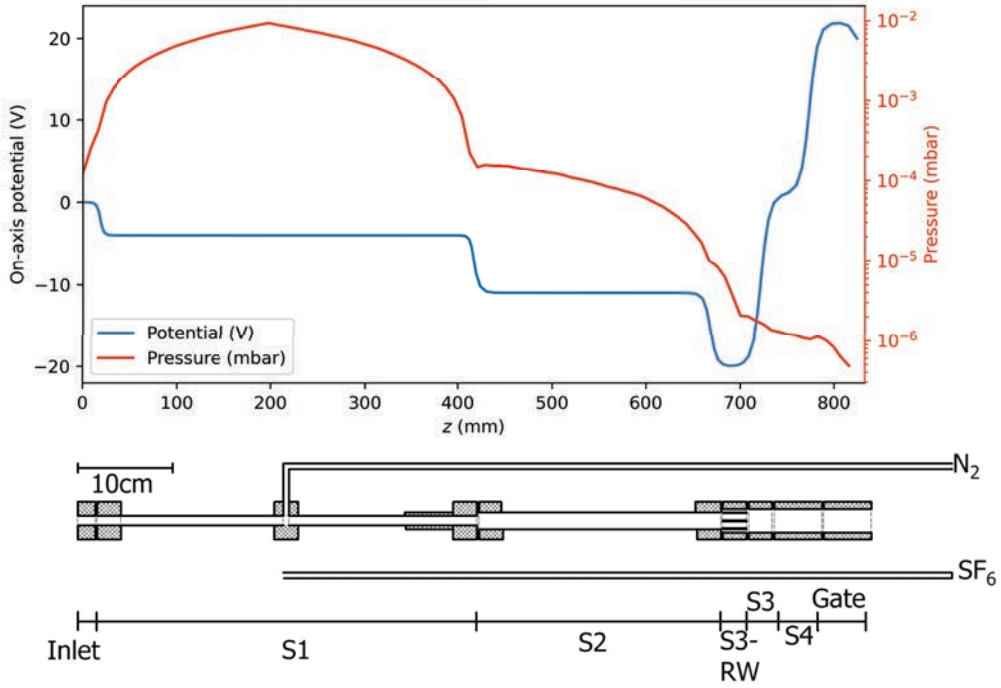

Figure 3.5: Scale drawing of the buffer gas trap electrodes, simulations of the trap pressure (red) and a typical on-axis potential (blue). N_2 is introduced into S1 as a buffer gas, SF_6 is introduced into the vacuum chamber as cooling gas.

The trap electrodes are housed in a water-cooled solenoid magnet producing an on-axis magnetic field of 750 G. The stepped potential is applied along the electrodes labeled Inlet, S1 and S2 in Fig. 3.5. The positrons are trapped in a potential well generated by the electrodes S3-RW (an eight-fold split electrode where opposite sections are shorted to apply a quadrupolar rotating field), S3, S4 and the Gate. The voltages applied are

Table 3.1: Dimensions of the BGT electrodes.

Name	Length (mm)	ID (mm)
Inlet	18.5	10
S1	400	10
S2	255	18
S3-RW	25	18
S3	25	25
S4	50	25
Gate	50	25

routed via a filter box which circuit diagram is shown in appendix A.1. To achieve ultra-high vacuum (UHV) a cryopump (Austin Scientific CP8 Cryoplex) is used. N_2 gas is introduced directly into S1 while SF_6 is introduced into the vacuum chamber via a gas pipe. The control of the trap potentials and the devices needed to fill the BGT was included into the upgraded control software of the ASACUSA-Cusp experiment, which is described in more detail in appendix B. A RW quadrupole electric field perturbation is applied during accumulation to counteract radial expansion, which is turned off prior to extraction, to allow the positrons to cool to room temperature. After a few tens of milliseconds, the positrons are extracted by applying a fast high voltage pulse to the Gate electrode.

3.1.3 Accumulator

The accumulator is a Penning-Malmberg trap, as shown in Fig. 3.6, DS of the BGT, the position of which in the experiment is shown in Fig. 3.1. The trap is housed in a water-cooled solenoid magnet operated at a magnetic field of $\sim 1100\,\mathrm{G}$.

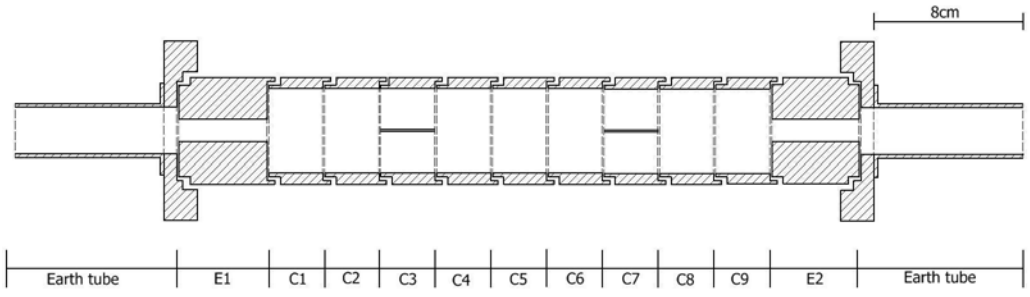

Figure 3.6: Scale drawing of the accumulator electrodes. The ceramic spacers between the electrodes are not shown.

Previously, positrons were accumulated in the BGT and multiple bunches were caught and stored (or 'stacked') in the Cusp trap to reach a sufficient number of positrons for antihydrogen production (order of millions to tens of million). This meant that during the production of antihydrogen in the Cusp trap, positrons could not be accumulated. Additionally, as mentioned above, the BGT is operating at a pressure of $\sim 10^{-6}$ mbar in the trapping region, the vacuum in the Cusp trap is $< 10^{-12}$ mbar. Previously, it was not possible to pump out the buffer gas in advance of a transfer from the BGT to the Cusp trap, consequently, the vacuum of the latter was contaminated every ~ 30 s. The accumulator stacks several bunches from the BGT, hold them while the buffer and cooling gases are pumped out and afterwards transfer all positrons stored into the Cusp trap at a low pressure ($<10^{-8}$ mbar).

The accumulator consists of eleven aluminium electrodes, the dimensions of which are listed in table 3.2. The electrodes are spray-painted with an alcohol based colloidal graphite solution to reduce potential inhomogeneities across the electrode surfaces (patch potentials [80]), and are separated by 1 mm through ceramic spacers. To hold the positrons in the accumulator a dipole RW electric field is applied to the four-fold split electrode C7. No additional cooling gas is introduced, since through natural conductance between the accumulator and BGT enough cooling gas reaches the trapping volume. Prior to extraction from positrons out of the accumulator into the Cusp trap, the upstream (US) gate valve (GV2 in Fig.3.1) is closed to pump out the chamber to $<10^{-8}$ mbar within 3 s. Afterwards, GV3 and GV4 are opened and the positrons are pulsed out by a high voltage pulse applied to the E2 electrode.

Table 3.2: Dimensions of the accumulator electrodes.

Name	Length (mm)	ID (mm)
E1	47.5	12
C1-C9	29	45
E2	47	12

3.1.4 Detectors and detection methods

This subsection describes the working principles of the detectors used for: measuring the number of positrons (Channel electron multiplier - CEM), for imaging (microchannel plate + phosphor screen - MCP/PS - and CCD camera), and measuring annihilation signals (CsI and plastic scintillators). The positions of the MCP and CEM are indicated in Fig. 3.1 and in Fig. 3.3. The CsI is cross-calibrated to the CEM and looks for annihilation signals on GV1 when the CEM is not inserted into the beamline. The scintillator paddle can be moved to positions along the experiment to look for annihilations, for example during transfer of positrons into the Cusp trap. The positions used most often

are indicated in Fig. 3.1.

Channel Electron Multiplier (CEM)

A schematic drawing of the CEM (model: KBL15RS/90-EDR from Dr. Sjuts Optotechnik GmbH) is shown in the top drawing of Fig. 3.7.

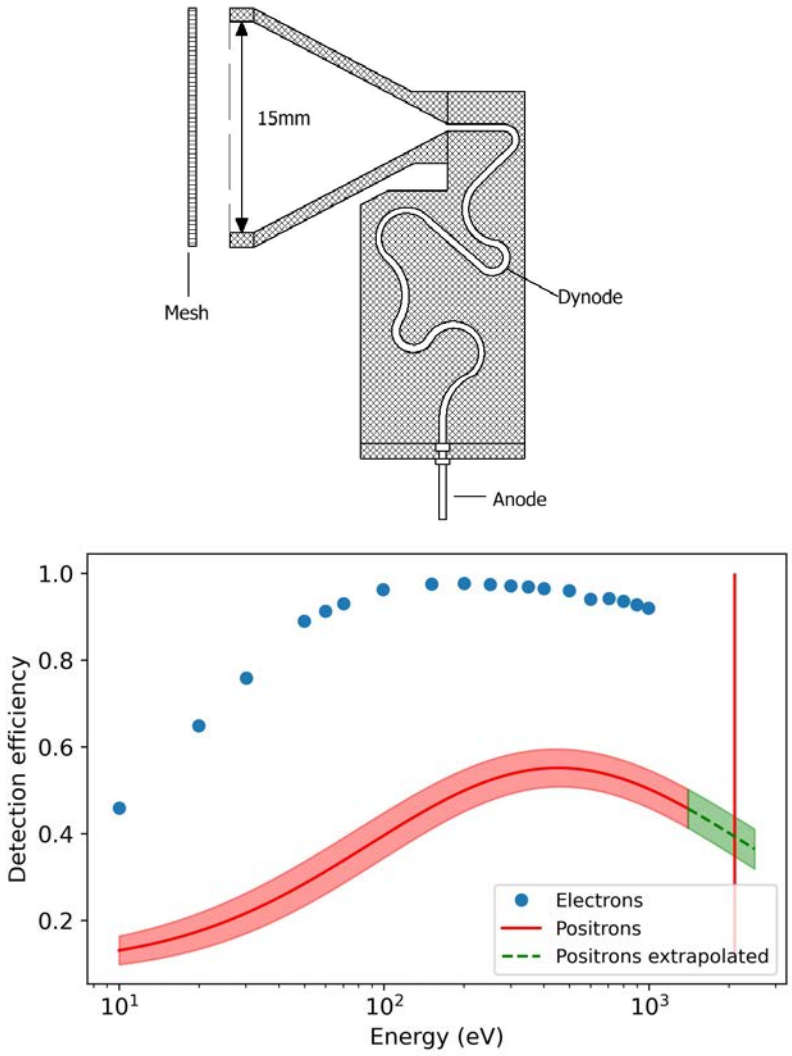

Figure 3.7: Top: Schematic drawing of the CEM.
Bottom: Detection efficiencies of a CEM measured for electrons (blue, from [81]) and positrons (red, using the lognormal fit function and parameters from [82]). The colored area indicates the uncertainty of the fit. The green region is the extrapolation performed to estimate the efficiency for the 2100 eV implantation energy of the positron beam used in this work.

The working principle of a CEM is secondary electron emission. Electrons emitted by an impinging particle are accelerated by a positive bias and produce an avalanche of secondary electrons which can be picked up at the anode. The CEM used can count up to 15 million particles per second. In front of the CEM a steel fine mesh (wire diameter 0.03 mm, pitch 0.25 mm) is installed to apply a potential barrier to perform an energy

spread measurement of the moderated positrons.

The efficiency of the CEM depends on the particle type. For electrons, the efficiency can be higher than $\sim 90\,\%$ [81], as shown in the bottom plot of Fig. 3.7. However, for positrons the efficiency is reduced due to the negative bias on the front [82] - the bias typically used in this work is $-2.1\,\mathrm{keV}$ - which allows electrons produced to be deflected out of the CEM instead of participating in the avalanche. To estimate the efficiency of the CEM for positrons, the log-normal function with the fit parameters given in [82] are used, resulting in an efficiency of $(39 \pm 5)\,\%$.

CsI and plastic scintillator

These detectors are used to measure the gamma-ray photons produced by positrons annihilating on surfaces. A gamma-ray photon traversing the crystal produces scintillation light. The light can be measured by an attached photomultiplier tube (plastic scintillator) or by an avalanche photodiode (CsI). In a photomultiplier, an electron is emitted from the cathode by an impinging photon. The electron gets accelerated by an electric potential produced by dynodes, starting an avalanche of secondary electrons. A measurable voltage pulse can be picked up at the anode, which is proportional to the incident number of gamma-ray photons. An avalanche photodiode is made of a p-n-junction operated in reverse bias. The impinging photon creates electron-hole pairs in the depletion layer. Due to the high electric field in the region, the electrons get accelerated and can ionise further atoms, hence produce an avalanche of charge carriers proportional to the incoming signal.

In the ASACUSA-Cusp experiment, a CsI detector with an active area of 1x1 cm is used to monitor the slow beam whenever the CEM is not inserted into the beamline (e.g. during the moderator growth, when the pressure is too high to operate the CEM). The plastic scintillator has an active area of ∼20x30x0.7 cm and a Hamamatsu PMT Model H8409-70 is attached to it. This detector has the advantage of a fast rise time of 2.1 ns, which can be used to measure the bunch width of the positrons extracted from the BGT. The detector is moved between the positions indicated in Fig. 3.1 to make relative measurements between positron bunches, for example during transfer into the Cusp trap to monitor losses.

3.1.5 Microchannel plate (MCP)

A MCP detector is a plate made of a resistive material with a large number of channels with a diameter of $\sim 10\,\mu\mathrm{m}$, as shown in Fig. 3.8a. The working principle is the same as for a CEM: particles impinging on the surface of the channels release an electron, which gets accelerated by an electrical potential and produce an avalanche of electrons, which can be measured as a current at the anode, as sketched in Fig. 3.8c. It is possible to install multiple MCP detectors in series (e.g. two MCP detectors in series as shown in Fig. 3.8b are called a chevron stack MCP detector) to further increase the gain. A

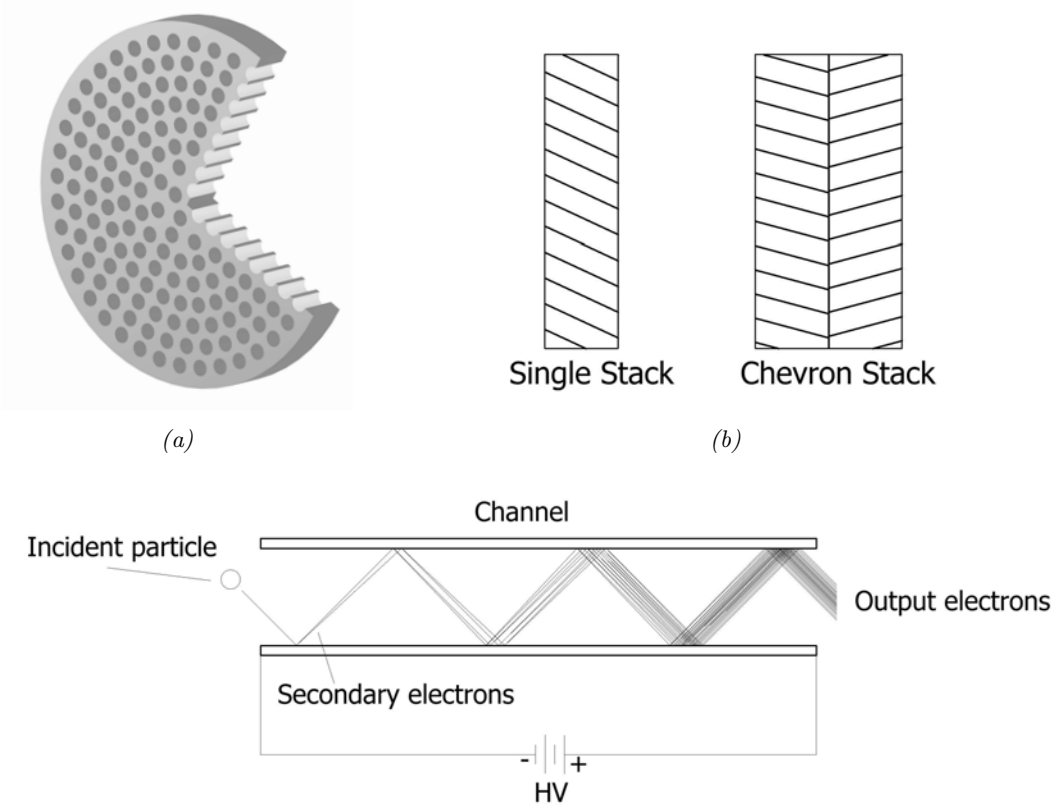

Figure 3.8: a) Schematics of a MCP detector. b) Side view of the MCP configurations used in the ASACUSA experiment. c) Operation principle of a single channel.

phosphor screen (PS) can be attached behind the MCP. The electrons interact with the screen and produce phosphorescence light. The light is reflected onto a CCD or CMOS camera to measure the radial distribution of a particle cloud or a plasma.

Three MCP detectors from Hamamatsu with a diameter of the effective area of 42 mm with phosphor screens attached are used in the ASACUSA-Cusp experiment, the positions of which are shown in Fig. 3.1. The positron MCP is in a chevron stack configuration, which is mounted on a rotatable feedthrough to either face the BGT or the accumulator. For the Cusp trap and MUSASHI single stack MCPs are used. The CCD camera used with the positron system MCP is an Apogee ALTA-U77, the cameras for the Cusp trap and MUSASHI are CS165MU1/M CMOS cameras from Thorlabs.

3.2 Antiproton catching: MUSASHI & Drift tube

Antiprotons are produced and delivered by CERN's accelerator complex. Only a brief description of the production of slow antiprotons will be given, more details on the deceleration procedure can be found in [83]. Protons are accelerated by a linear accelerator and the first two ring accelerators (the Proton Synchrotron Booster and the Proton

Synchrotron) to a momentum of 26 GeV/c and are extracted into the Antiproton Decelerator (AD). The production of antiprotons happens by the interaction of high energy protons in an Iridium target, where the process

$$\mathrm{p} + \mathrm{p} \rightarrow \mathrm{p} + \mathrm{p} + \mathrm{p} + \overline{\mathrm{p}} \tag{3.1}$$

can occur in a small fraction of collisions. More than $5 \cdot 10^7$ antiprotons are produced, by an incident number of protons on the order of 10^{13}, with a momentum of 3.6 GeV/c, which need to be decelerated and cooled. Deceleration is achieved by RF cavities. Cooling is performed in several stages, dependent on the mean energy of the particles. The first cooling stage is at the initial momentum of 3.6 GeV/c. The first deceleration phase decreases the momentum of the antiprotons to 2 GeV/c (second cooling stage). Stochastic cooling is used in the first and second stage to cool the antiprotons [84]. In this technique pickup electrodes measure the difference of momentum and transverse position Δp and Δx of a subset of antiprotons. On the opposite side of the ring a "Kicker" corrects the trajectory by the application of an electric pulse. After several corrections, the resulting relative momentum spread decreases to the order of a few percent.

The third cooling stage which occurs at a momentum of 300 MeV/c and the final cooling stage at 100 MeV/c, which equates to a kinetic energy of 5.3 MeV, use electron cooling [85]. In this technique a co-linear electron beam is produced with an energy such that in the centre-of-mass frame the antiprotons see a stationary, low temperature electron reservoir. The antiprotons lose energy by Coulomb interactions and the heated electrons are afterwards removed from the antiprotons. This cooling method reduces the final relative momentum spread to the order of 0.01 %.

Previously, these antiprotons were delivered to the experiments, where further deceleration methods were applied in order to be able to catch the antiprotons (e.g. for ASACUSA a Radio-frequency Quadrupole Decelerator (RFQD) was installed to reduce the energy to 120 keV). However, in 2021 an additional decelerator ring, the Low ENergy Antiproton ring (ELENA), started operation [86]. This ring decelerates the antiprotons further to 100 keV and uses electron cooling to reduce the energy spread. These antiprotons are then delivered simultaneously in up to four bunches on the order of $\sim (5 - 10) \cdot 10^6$ particles each to the experiments.

In order to be able to catch the incoming antiproton beam the particles have to lose energy. This is achieved via degrader foils [87]. The antiprotons energy loss in the foil comes from ionisation and excitation of the electrons and interaction with the nucleus of the foil material [87]. After passing through the foils the energy of the antiprotons has decreased to several keV, depending on the thickness of the foil, and they are caught in a potential well. To stop the particles from escaping, a low temperature electron plasma is prepared in the trap such that the antiprotons cool by interactions with the electrons as described in Section 2.2.2.

3.2.1 Electron gun

The antiproton preparation cycle needs electrons to cool the antiprotons to sub eV energies. The electron gun consists of two Ba sintered cathodes with four electrodes as sketched in Fig. 3.9. It can be inserted and taken out of the beamline DS of the antiproton trap as shown in Fig. 3.10 in the subsequent section. Electrode A is used to apply a negative bias to the cathode, electrode B is the anode, electrode C is at ground potential to fix the electric field and electrode D shields the antiprotons from the stray electric field from the electron gun when it is not inserted into the beamline. The electron gun can provide several million electrons per second.

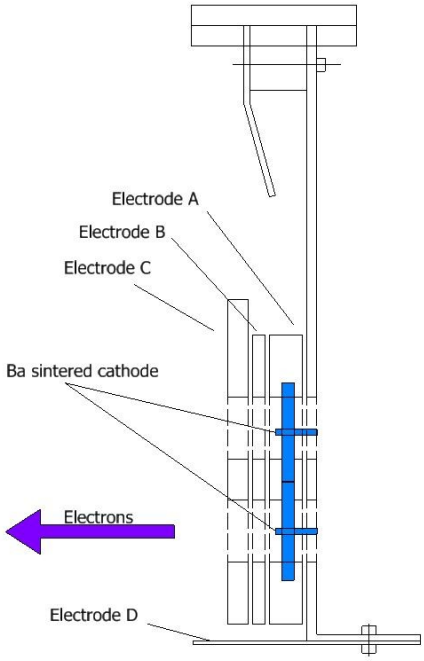

Figure 3.9: Sketch of the electron gun.

3.2.2 Drift tube

As mentioned above, the AD previously provided antiprotons with an energy of 5.3 MeV, which were decelerated to 120 keV using the RFQD. Since the installation of ELENA, which provides an antiproton beam with an energy of 100 keV, the RFQD is no longer needed. However, the degrader, which consists of two biaxially orientated polyethylene terephtalate (Bo-PET) foils [88] with a nominal thickness of 900 nm and a mass thickness of 90 μgcm^{-2}, was optimised to the output energy of the RFQD and it was decided to leave the foil in place and design and install a drift tube [89]. This has the advantage that the incident energy of the antiprotons can be optimised to the highest efficiency of the degrader foils. A sketch of the drift tube and the antiproton catching trap is shown in Fig. 3.10. The drift tube consists of a 1.5 m long aluminium-alloy electrode with an ID of 31 mm [89]. Four electrostatic deflectors are installed at the DS side of the electrode

to steer the antiprotons. A voltage of up to 20 kV can be applied which corresponds to a maximum beam energy of 120 keV. The left hand side of Fig. 3.11 shows the dependence of the trapped fraction of antiprotons as a function of acceleration voltage.

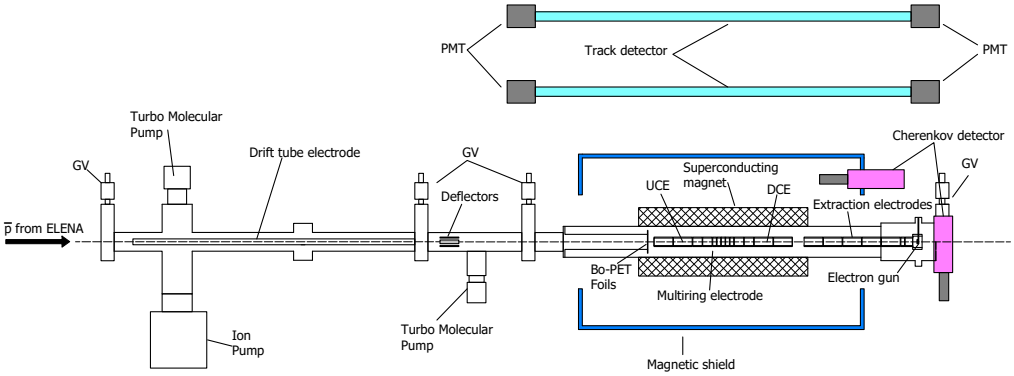

Figure 3.10: Sketch of the Drift tube and MUSASHI. The dimensions are not to scale. Adapted from [89].

3.2.3 MUSASHI

MUSASHI (Mono-energetic Ultra-Slow Antiproton Source for High-precision Investigation) is a Penning-Malmberg trap housed in a superconducting magnet to trap antiprotons delivered by ELENA and are accelerated by the drift tube [88]. A sketch is shown in Fig. 3.10. The trap is located in a cold bore, which is held at cryogenic temperatures by two cryo coolers. Additionally, two thermal shields (one US and one DS) are held at 50 K to reduce the thermal radiation introduced from room temperature regions outside the trap. Achieving a low temperature in the trapping region is essential for antiproton trapping because it reduces residual gas and hence the loss of antiprotons via annihilation, which increases the lifetime of antiprotons in the trap.

The trap electrodes of MUSASHI consist of two separate parts: a multiring electrode stack (MRE) for catching and cooling of the degraded antiprotons, and a stack of extraction electrodes (EE). The MRE consists of 14 ring electrodes with an inner radius of 20 mm. The central five electrodes are 20 mm in length to apply a harmonic potential. One electrode is split into four segments to apply a dipole RW electric field for compression.

A typical catching cycle is as follows. A harmonic potential well is produced by the five central electrodes. Before catching antiprotons, electrons are filled and expanded to a radius of > 5 mm and a density of $(1-3) \cdot 10^8\,\mathrm{cm}^{-3}$ to increase the overlap with the incoming antiprotons. The drift tube is biased to increase the antiproton beam energy from 100 keV to 119 keV, which was found to be the maximum in trapped antiproton signal [89]. After the arrival of the antiprotons, a potential of -12 kV is applied to the US and DS catching electrodes (UCE and DCE in Fig. 3.10) to confine the particles decelerated by the foil. Antiprotons cool on the electrons for 40 s, after which the high

voltage potential barrier is removed to let the antiprotons which did not cool on the electrons due to the poor overlap with the electrons escape. Afterwards, the electrons are removed from the well and the cold antiprotons are compressed by the application of a RW electric field. The bunch can then be extracted through the EE, which serve as an electrostatic lens. Without this additional focusing the antiproton cloud would expand because the antiprotons follow the diverging magnetic field lines. With this scheme a catching efficiency of $(26.6 \pm 6)\,\%$ was measured, resulting in $(1.4 \pm 0.2) \cdot 10^6$ antiprotons per bunch confined and cooled in the trap [89]. The right hand side of Fig. 3.11 shows a typical time evolution of the annihilation counts during one catching cycle measured with the track detector. At the end of the cycle, the antiprotons were slowly extracted to the foils to measure the trapped fraction.

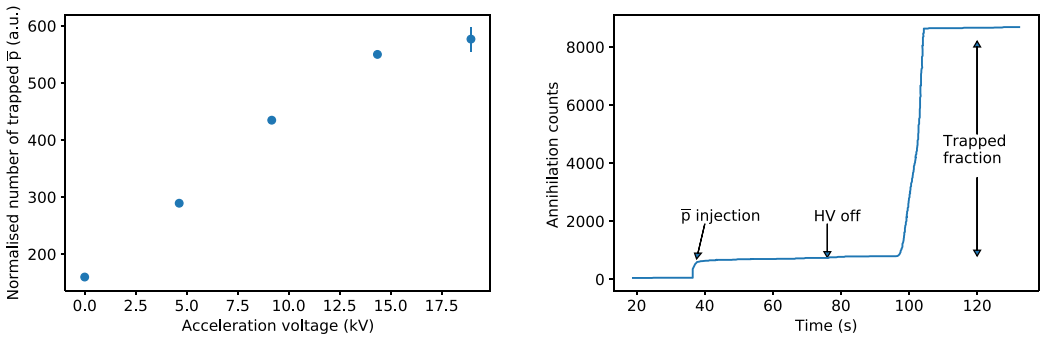

Figure 3.11: Left: Trapped fraction of antiprotons as a function of acceleration voltage applied to the drift tube.
Right: Typical cumulative annihilation counts measured by the track detector during an antiproton catching cycle. Both adapted from [89].

3.2.4 Detectors

For the diagnostics of the antiprotons several detectors are used: the foil detector, the track detector, and Cherenkov detectors (all indicated in Fig. 3.10).

The foil detector is used for measuring the beam profile of the incoming antiprotons non-destructively. It consists of ten 25 nm thick and 940 μm wide silver strips printed onto each of the Bo-PET foils [88]. Antiprotons impinging on the silver strips produce secondary electrons, which are accelerated to an anode foil. From the charge picked up at each of the strips the beam profile and position can be measured.

The annihilation products of antiprotons are mainly pions. The charged pions can be measured using a cherenkov detector installed DS of the trap. The detector is an acrylic plate (Mitsubishi Rayon, Acrylite-000) with a refractive index of n = 1.49, which means that particles with a velocity greater than $v/c = 0.7$ produce cherenkov light, corresponding to a pion velocity of at least 130 MeV/c[90]. The photons produced are detected by a fine-mesh PMT (Hamamatsu Photonics, R5505GX-ASSY). This detector is mainly used to detect annihilation signals of antiprotons on the DS side of the

apparatus, for example, the fraction of the degraded antiprotons at different drift tube voltages.

Two sets of scintillating bars, called the track detector in Fig. 3.10, count the annihilation signal during the antiproton catch and preparation cycle and are used for estimating the number of caught antiprotons. The track detector consists of two 2 m long plastic scintillator bars, mounted parallel to the axis of the trap at a distance of 82 cm and 150 cm. The cross sections of the bars are 4x6 cm. Scintillation light produced in each of the bars by pions is read out by one PMT on each end. The difference in arrival time of the signal on each of the PMTs can be used as an estimate of the location of the annihilation with a precision of 20 cm.

3.3 Cusp trap

The Cusp trap is a Penning-Malmberg trap within a magnetic field produced by four coils in an anti-Hemholtz configuration. As explained in chapter 2.3.2, the energy levels in which the antihydrogen atoms are leaving the trap is highly dependent on the temperature and density of the positron plasma. In the previous trap (in the following called trap I, which was not used in this work, hence details can be found elsewhere [52]) used for antihydrogen production [91], the minimum temperature of the plasma was ~ 125 K, as can be seen as the red data set in Fig. 3.12. Hence, an upgrade of the trap was necessary to achieve a reduction of temperature.

The upgrade was performed in two iterations: Firstly, in trap II the diameter of the trap electrodes was reduced from 80 mm to 34 mm, the electrodes were spray painted with colloidal graphite and installed into the same coldbore as Trap I. A technical drawing of this trap with a sketch of the vacuum chamber is shown in Fig. 3.13. This iteration was intended to test the new electrode design in the apparatus and perform plasma studies. Measurements in this trap indicated that the minimum temperature of the plasma is not only limited by the electrode temperature, but the plasma heats up by microwaves entering from the room temperature region DS [52]. This was seen by closing/opening a thermal shield which was installed DS of the region were the plasmas are stored for mixing, indicated in orange in Fig. 3.13. The plasma was consistently 20 K warmer if the shield was open, as is shown in Fig. 3.12. Nevertheless, as the ASACUSA-Cusp experiment aims to produce an antihydrogen beam, it is not possible to use a closed shield during operation.

The second iteration of the upgrade was to redesign the Cusp trap and the surrounding cold bore (trap III in Fig. 3.12) with the focus on the reduction of the temperature of the electrodes and blocking microwaves entering from room temperature regions. As this trap was used for most of the experiments presented in this work it will be described in more detail in the following subsection. Additionally, in the course of the upgrade, the control software was renewed with the focus on having a simple and user friendly setup which is the same for all apparatuses (i.e. positron system, Cusp trap

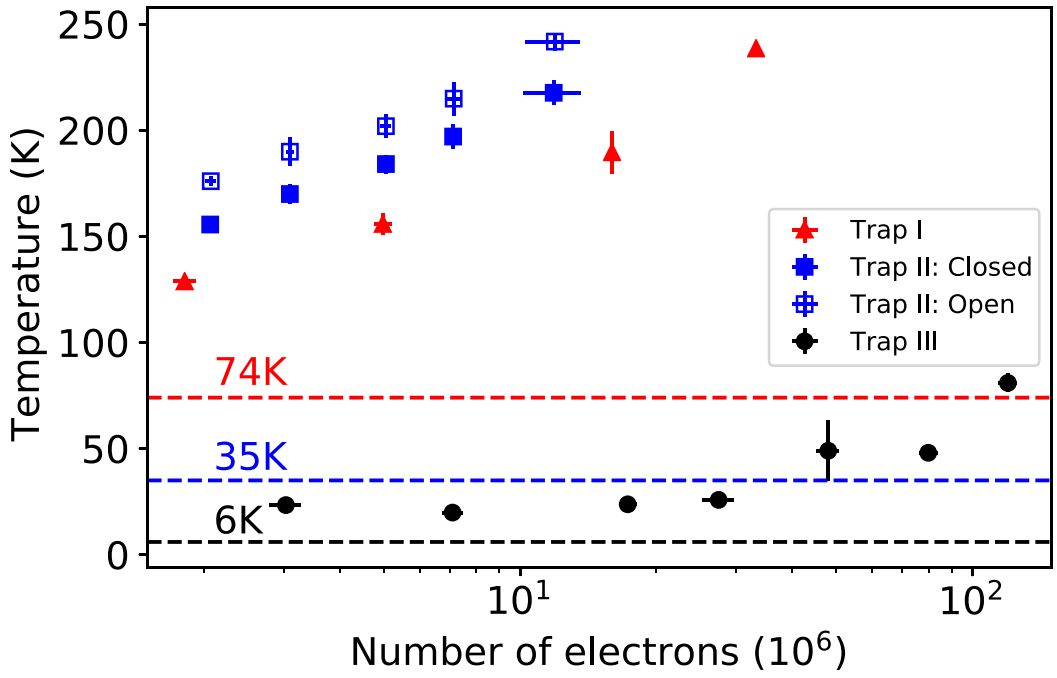

Figure 3.12: Temperature of an electron plasma as a function of the number of particles for Cusp trap I (red), trap II with a thermal shield open (open blue squares), and closed (filled blue squares) and the upgraded trap (trap III, black). The horizontal dashed lines indicate the temperature of the electrodes in the traps. Data from [52].

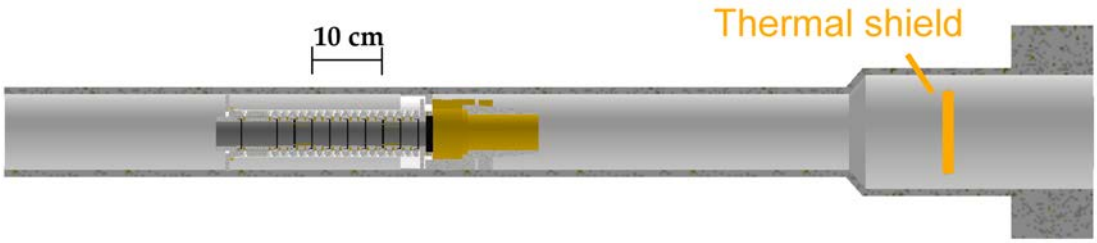

Figure 3.13: Technical drawing of trap II and a sketch of the vacuum chamber. The position of the heat shield is indicated in orange.

and MUSASHI). A description of the new control software is given in appendix B.

3.3.1 Cold bore and MRE

A technical drawing of the electrodes of trap III and its relative position within the inhomogeneous magnetic field is shown in Fig. 3.14.

Cold bore

The system consists of an outer insulation vacuum chamber housing the cold heads, and an inner vacuum chamber with the MRE.

To reduce the temperature of the electrodes, good thermal contact between the 4 K

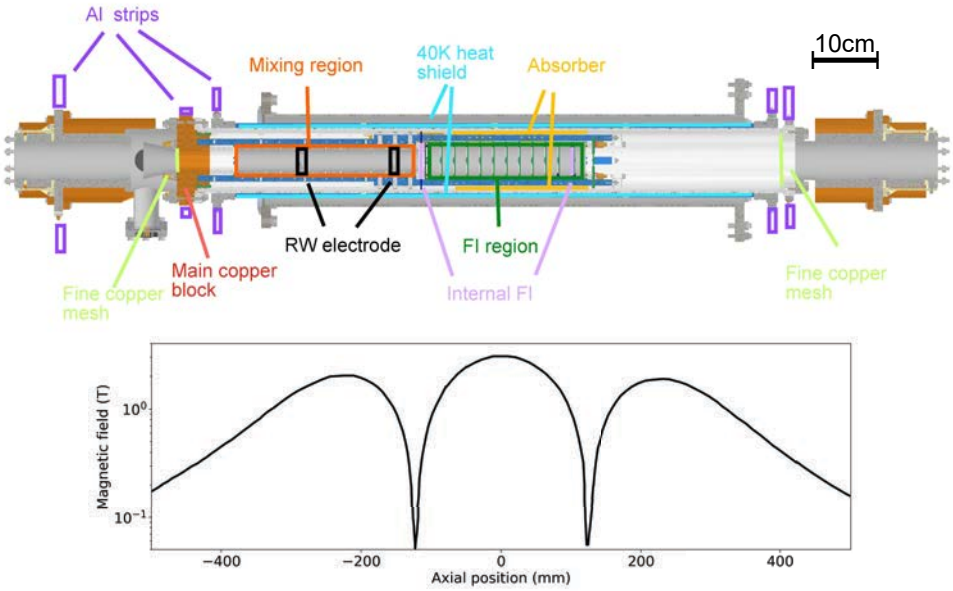

Figure 3.14: Technical drawing of the cold bore and the electrodes, and the on-axis magnetic field. The outer vacuum chambers, the cryo coolers and the magnet are not shown. The main parts of the upgrade are labelled.

stage of the US cryo cooler and the electrodes is achieved via annealed 5N aluminium strips, which are fixed on a copper block (labelled "main copper block" in Fig. 3.14) on which the electrode stack is mounted.

Electrical and thermal connections of the electrodes are obtained by using cryogenic filters. These connections, mounted on annealed 5N aluminium bars, provide direct contact between the electrodes and the main copper block. The trap is housed in the inner vacuum chamber. Because of its connection to room temperature vacuum chambers, it is essential to avoid heat leaks. This is achieved by using a staggered bellows system US and DS, which are connected to the 4 K, then to the 40 K and eventually to the 300 K region. A copper heat shield surrounds the inner vacuum chamber and additionally, cryogenic insulation (Beyond Gravity Coolcat 2 NW, PL100297) is wrapped around the 40 K regions.

MRE

The MRE consists of 22 electrodes, ten electrodes form the US mixing region, and twelve form the DS field ionising (FI) region, as shown in Fig. 3.14. Two electrodes are split into four sections to apply a RW electric field. The inner diameter of the electrodes in the mixing region is 34 mm and the length of a single electrode is 25 mm. The DS electrodes are all 50 mm in diameter and 19.5 mm long. All electrodes are gold coated and spray painted with colloidal graphite to reduce patch potentials [80].

To attenuate microwaves entering the trap from room temperature regions, fine copper meshes with a pitch of 0.25 mm and a wire diameter of 0.03 mm, and also spray

painted with colloidal graphite, are installed at the entrance and exit of the trap. These meshes provide a reduction in microwave power of frequencies below 60 GHz by at least 20 dB. Additionally, long sections of resistively coated ceramic are connected onto the 5N aluminium bars to absorb microwaves produced by the rotation of the plasma. This material is also used by CERN's RF group to absorb microwaves in accelarator beamlines [92].

To align the trap with the magnetic field from the outside, kevlar ropes are tied in loops around rings on the inner vacuum chamber, which are adjustable from the air-side. This provides alignment in x, y and z direction after the trap is installed in vacuum.

The upgrade of the trap succeeded in reducing the temperature of the electrodes from 35 K to 6 K. Additionally, as can be seen in Fig. 3.12, the temperature of the measured electron plasma was reduced by at least a factor of five to 25 K over a wide range of number of particles in the plasma. The temperature of the plasma was within 20 K of the wall temperature, which was not achieved with any of the previous traps.

3.3.2 Detectors

A single stack MCP with a phosphor screen is installed US of the Cusp trap, as indicated in Fig. 3.1. The light is acquired by a CMOS camera for imaging the radial distribution of the plasmas contained within the Cusp trap. Additionally, a setup with a sillicon photomultiplier(SiPM) surrounding the camera is used to acquire light from the PS. This detector assembly is essential for plasma manipulation and optimisation because it enables measurements of the temperature, radius and number of particles.

A scintillator is installed around the UHV chamber of the trap, which was previously used to trigger the ASACUSA micromegas tracker (AMT)[93]. The AMT was removed from the system, however, the scintillator (called the Cusp Segmented Scintillator - CSS) was still in place and could be used to measure pions produced by antihydrogen/antiprotons annihilating on the trap electrodes. The detector consists of eight, 3 mm thick, 7 cm wide and 42 cm long plastic scintillators. The bars were polished and curved to fit around the trap chamber. The light from each of the scintillators of the CSS is read out by a multianode PMT (Hamamatsu H7546A), which is connected to a programmable logic module (Technoland N-PL 101), which can be set to produce a trigger of an event when a signal appears in two of the scintillators (2-coincidence) or three of the scintillators (3-coincidence).

Additionally, two pairs of scintillating bar detectors are installed at a distance of ~ 0.5 m and ~ 1 m from the Cusp trap, as shown in Fig. 3.1. The detector consists of eight panels of 54-60 scintillator bars, each having a cross section of 15x19 mm^2 and a length of 960 mm, which are read out by SiPMs. Two of the panels, one with horizontally oriented bars and the other with vertically oriented bars, are coupled. This gives in total four x-y sensitive detectors for vertex reconstruction with a spatial resolution of 6 mm

[94].

To be able to measure the principal quantum number of antihydrogen atoms produced, the atoms need to be field ionised. Field ionisation is a process in which a bound electron is removed from the atom by the application of an electric field. Classically speaking, this can occur if an external electric field (for simplicity we assume it is pointing in the z-direction) changes the Coulomb potential of the atom produced by the nucleus to the perturbed form $V(\vec{r}) = -1/|\vec{r}| + Ez$, where Ez is the perturbation due to the electric field. The Coulomb potential has a saddle point $V_\mathrm{s} = -2\sqrt{E}$, which can be decreased by the external electric field. If the saddle point is less than the binding energy of the electron, it can escape the atom leaving a positive ion behind [95]. For a Rydberg state the classical ionisation limit equates in atomic units to $E_\mathrm{C} = 1/(9n^4)$ [95].

For that purpose, field ionisers (FI) are installed inside and outside of the Cusp trap. The external field ioniser, mounted 140 cm DS of the production region, was previously used to measure the principal quantum number n of the antihydrogen atoms [41]. It consists of two parallel copper meshes (3.04 mm spacing and 0.07 mm tine thickness) separated by (10.25 ± 0.25) mm with a total transparency of 95 %. A potential difference between the two meshes produces the ionising electric field region. Additionally, two internal field ionisers, an image of which is shown in Fig. 3.15, were installed in the center and at the end of the MRE, positioned at the two magnetic field nulls, as indicated in Fig. 3.14, which are coated with colloidal graphite with a transparency of 97 %.

Figure 3.15: Image of DS internal field ioniser.

3.4 Spectroscopy line

As described in Section 1.4.1, the experimental method for measuring the ground-state hyperfine splitting of a spin-polarised antihydrogen beam is a Rabi experiment. The following subsections describe briefly the individual apparatuses of the spectroscopy line.

3.4.1 Microwave cavity

The microwave cavity consists of a strip-line resonator in a homogeneous magnetic field produced by coils in a McKeehan-like configuration [96, 97]. The split-line resonator, shown on the left hand side of Fig. 3.16, produces an oscillating magnetic field with inhomogeneities of 3 % in the plane perpendicular to and a sinusoidal gradient along the beam-axis. A homogeneous magnetic field with a relative precision of (590±70) ppm is produced by four coils in a McKeehan-like configuration, which is used to generate the Zeeman splitting of the states.

To be in control of the static magnetic field, the magnetic noise coming from the environment, such as the earth's magnetic field or from other magnets, has to be shielded. This is achieved by a three layer cylindrical mu metal shielding surrounding the cavity, as shown on the right hand side of Fig. 3.16 [97]. To further minimise stray magnetic fields from the Cusp magnet which produce inhomogeneities at the interaction region, measurements and the development of compensation coils are currently ongoing. The cavity and shielding was tested with hydrogen and it was shown that hyperfine splitting could be measured to a relative precision of $4.4 \cdot 10^{-10}$ [38].

3.4.2 Sextupole magnet and Detector

The sextupole magnet produces an inhomogeneous magnetic field in the perpendicular plane to the beam-axis to deflect atoms which undergo a transition in the microwave cavity. The magnet was manufactured by Tesla Engineering Ltd. and produces a magnetic field with a pole strength of 3.5 T.

The antihydrogen detector consists of a Bismuth-Germanium-Oxide ($Bi_4Ge_3O_{12}$, BGO) crystal scintillator and a tracking detector, a two layer hodoscope [98, 99], as shown in Fig. 3.17. The BGO crystal is 90 mm in diameter and 5 mm thick and is mounted on the vacuum side of a viewport. The US surface is coated with a 0.7 μm layer of graphite to absorb reflected photons from the DS side. On the air-side of the viewport 64 SiPMs are mounted to acquire the scintillation light produced by the annihilating antihydrogen atoms. The annihilation products, mainly pions, are tracked with the hodoscope. The latter consists of two layers of 32 scintillating bars each arranged in an octagonal configuration around the BGO chamber oriented parallel to the beam-axis. The light is acquired by two SiPMs on each bar, yielding a position resolution of 35x30 mm^2 for the outer layer and 20x20 mm^2 for the inner layer. Additionally,

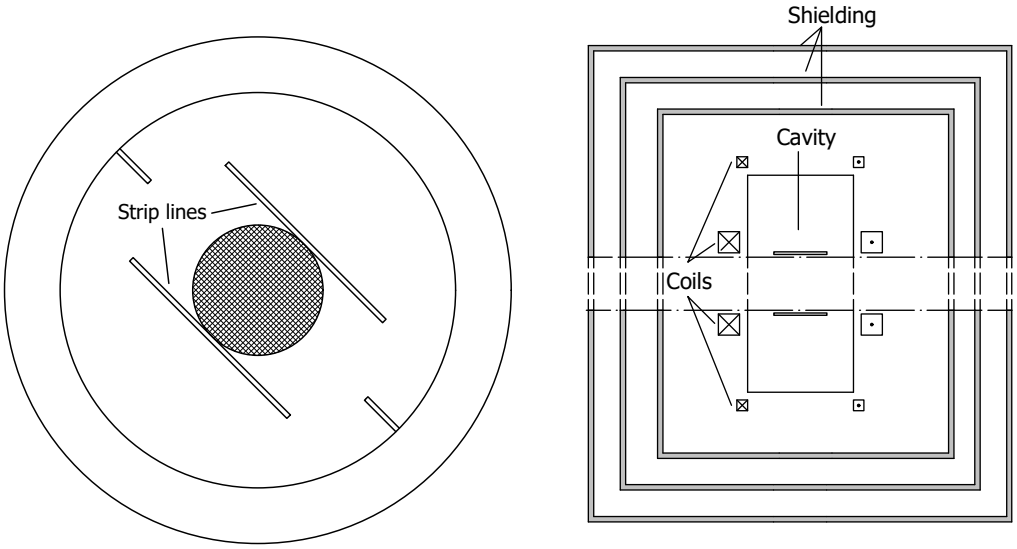

Figure 3.16: Left: Sketch of the spin-flip cavity. The atoms pass through in the direction into the paper.
Right: Sketch of the cavity the magnetic shielding with the four coils in a McKeehan-like configuration.

scintillator tiles (EJ 200) are mounted perpendicular to the scintillating bars to provide position resolution in the beam direction, shown in Fig. 3.17 in orange.

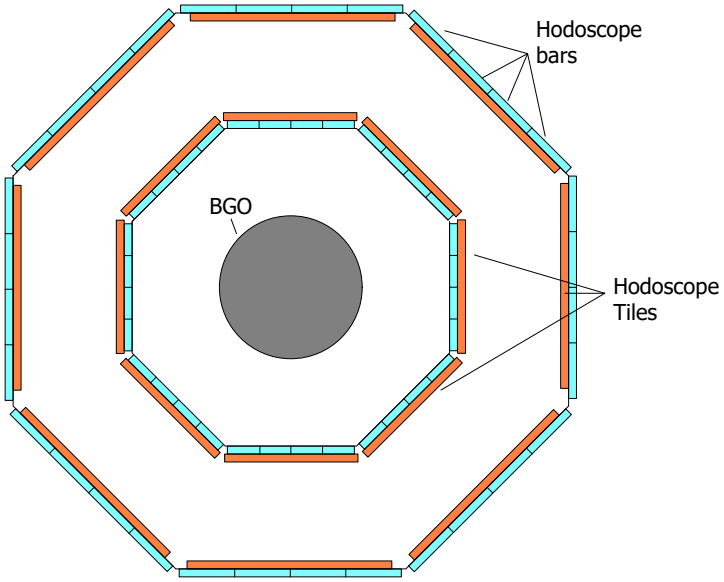

Figure 3.17: Front view of the hodoscope.

3.5 Proton source

In order to optimise the techniques used to produce antihydrogen at times when no antiprotons are available at CERN, such as the long shutdowns and the annual year-end technical stop, the ASACUSA collaboration developed a low energy proton source [100]. This source can be installed at the position of MUSASHI, which has to be removed from the experimental beamline. The advantage of this system is that the same apparatus, i.e. the same traps and beamline, can be used to produce hydrogen instead of antihydrogen. It should be possible to produce antihydrogen with the same plasma properties as for hydrogen production by reversing the polarity of the electric fields for trapping and mixing.

3.5.1 Method

The source uses electron impact ionisation of H_2 gas to produce bunches of protons [100]. It consists of three modules: an electron gun, a gas cell trap, and an ion extraction and steering module, as shown in Fig. 3.18(a) in red, blue and orange, respectively. Each module consists of electrodes surrounded by permanent magnets producing the inhomogeneous magnet field shown in Fig. 3.18(b) to be able to trap and guide the protons from the source along the beam axis. The distribution of the magnets is shown in Fig. 3.18(c). The electron beam is produced by a tungsten filament and is focused by the anode through a 2 mm aperture into the gas cell.

The gas cell consists of three electrodes (two endcaps and a fourfold segmented electrode), see Fig. 3.18(a) in blue. The molecular hydrogen gas is introduced directly into the center of the gas cell trap via a plastic hose where it can be dissociatively ionised ($H_2 + e^- \rightarrow 2e^- + H + H^+$) by the electron beam and the protons can be trapped in a potential well produced by the three electrodes as shown in Fig. 3.18(d)&(e).

However, processes which produce H_2^+ via direct ionisation ($H_2 + e^- \rightarrow 2e^- + H_2^+$) have an order of magnitude higher cross section [101], as shown in Fig. 3.19. Subsequently, the molecular ion can produce H_3^+ by interaction with the hydrogen gas via $H_2^+ + H_2 \rightarrow H_3^+ + H$. To suppress the number of extracted contaminants a RW electric field can be applied to the central electrode of the gas cell. At a frequency and amplitude stabilising the motion of protons, H_2^+ and H_3^+ will not fulfill the confinement condition due to their larger mass and consequently different motion in the trap. After some accumulation time the particles can be extracted by pulsing down the DS endcap.

The extraction module consists of three electrodes (the endcap, a fourfold segmented steering electrode and an exit electrode). The purpose of this module is not only to accelerate the protons out of the production region, but also to be able to steer and focus the bunch. As this device is installed into the experimental beamline at the position of MUSASHI, it is necessary to be able to steer the particles into the mixing trap if small misalignments of the two systems are present.

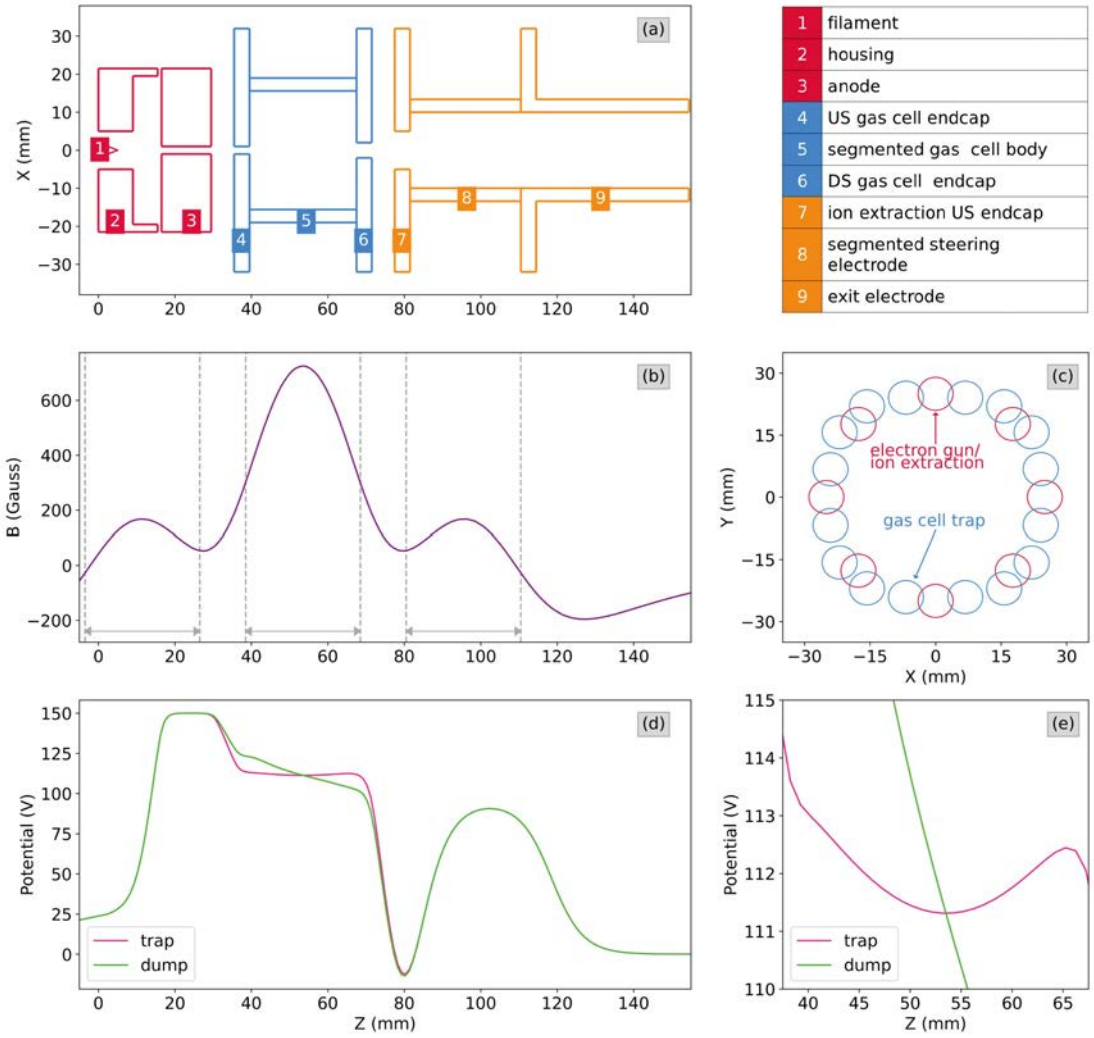

Figure 3.18: Top: Schematic of the proton source modules (a): the electron gun (red), the gas cell (blue) and the extraction and steering module (orange).
Middle: On-axis magnetic field (b) produced by the permanent magnets with an azimuthal distribution (c).
Bottom: Electrical potential during trapping and dumping of protons (d) and a zoom on the trapping region (e). All from [100]

3.5.2 Results of test setup

The proton source successfully produces bunches of protons [100], which was shown in a test setup before it was sent to CERN. A sketch of the experimental setup used for commissioning the proton source in Vienna is shown in Fig. 3.20.

The proton source is mounted on a DN160 ISO-K 4-way cross, which is connected to the detector chamber, a DN100 CF 4-way cross, via an adapter flange. The vacuum is provided by two turbo molecular pumps (TMP1: Agilent TwisTorr 304 FS and TMP2: Leybold Turbovac 350iX). Molecular hydrogen gas is produced by a MARS H_2 generator and is introduced into the gas cell of the source through an externally controlled needle

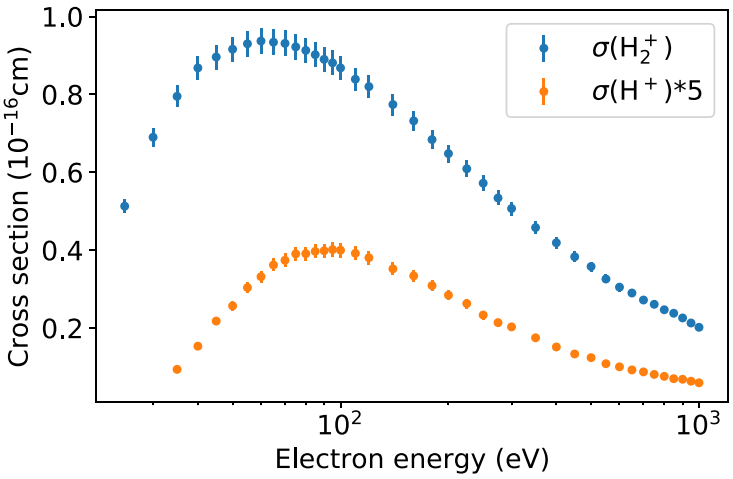

Figure 3.19: Cross section of direct ionisation of molecular hydrogen $\sigma(H_2^+)$ (blue) and of dissociative ionisation $\sigma(H^+)$ (orange) multiplied by a factor of five for visibility. Data from [101].

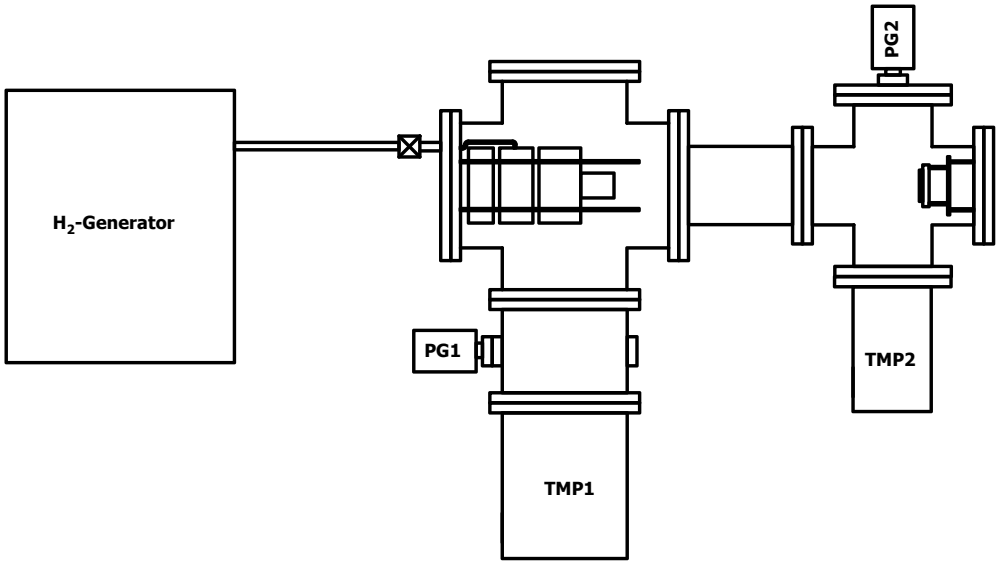

Figure 3.20: Sketch of the experimental setup for commissioning the proton source. The source itself is sketched in the left chamber and the MCP with delay line anode in the right chamber. The turbo molecular pumps (TMP), the scroll pump, the hydrogen generator and the pressure gauges (PG) are not to scale. The valves is indicated by "X".

valve to control the pressure inside the vacuum chamber. Typically, a H_2 pressure of $1 \cdot 10^{-6}$ mbar (measured with the PG1) is used, corresponding to $\sim 1.2 \cdot 10^{-4}$ mbar in the gas cell, according to a simulation performed with Molflow+ [102].

To be able to apply a RW electric field and to pulse the entrance and exit electrodes of the gas cell, the voltages are routed via a RF-coupling box, as shown in the appendix A.3. The RF signals are produced by two arbitrary waveform generators (BK Precision

4054B) followed by two Mini Circuits $0° - 180°$ power splitters (ZSCJ-2-2+). The ions are measured by a RoentDek DLD40 detector, which is a MCP with a position sensitive delay-line anode [103].

The electron gun, a tungsten filament from Kimball Physics (ES-020), is operated at 1.725 A/1.07 V, instead of the nominal current of 2.5-2.8 A, which yields a current of $I_0 \sim 84$ pA. This low emission current was chosen to protect the MCP from the high-intensity ion beams. The electron beam was focused by the anode, which was set to ~ 100 V.

The protons and ions are extracted from the source by pulsing down the DS blocking potential. The different species can be distinguished by their time-of-flight spectrum. By applying a RW electric field it is possible to suppress the unwanted molecular ions as shown in Fig. 3.21. Each species is driven out by a frequency close to the magnetron frequency (ω_-). Additionally, for protons a frequency close to twice the axial bounce frequency (ω_z) increases the count rate observed. The reduction in the count rate close to the mass-reduced cyclotron frequency (ω_c), which broadens with increasing RW amplitude, is explained by dipolar excitation, which is used as an ion cleaning mechanism in Penning trap setups (e.g. ISOLTRAP [104]).

Figure 3.22 shows the number of protons, H_2^+ and H_3^+ as a function of the RW frequency at an amplitude of 13.5 V. At a frequency of 0.47 MHz the highest difference in the proton count rate and the unwanted molecular ions is achieved.

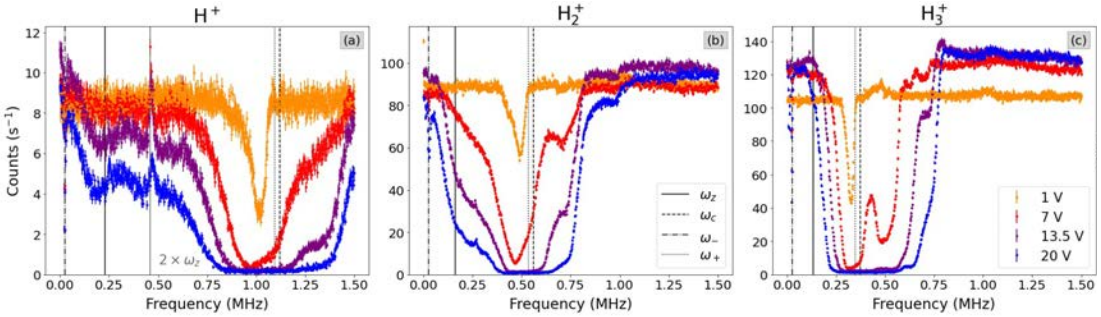

Figure 3.21: Count rate as a function of RW frequency for H^+ (a), H_2^+ (b) and H_3^+ (c) at a RW amplitude of 1 V (orange), 7 V (red), 13.5 V (purple) and 20 V (blue). Additionally, the magnetron (dashed-dotted), axial bounce (solid), cyclotron (dashed) and modified cyclotron (dotted) frequencies are shown. From [100].

The optimised system yields energy tunable proton pulses of $(8.67 \pm 0.38)\,\mathrm{s}^{-1}$, with a repetition rate of 500 Hz. The contamination of H_2^+ and H_3^+ is minimised to 5.5 % and 15.5 %, respectively. It is important to note that this rate was due to the low electron intensity of $I_0 \sim 84$ pA. By operating the source with the filament at the nominal value of about 2.5 A ($I_0 \sim 4.8\,\mu$A) the count rate should increase to $\sim 10^5\,\mathrm{s}^{-1}$.

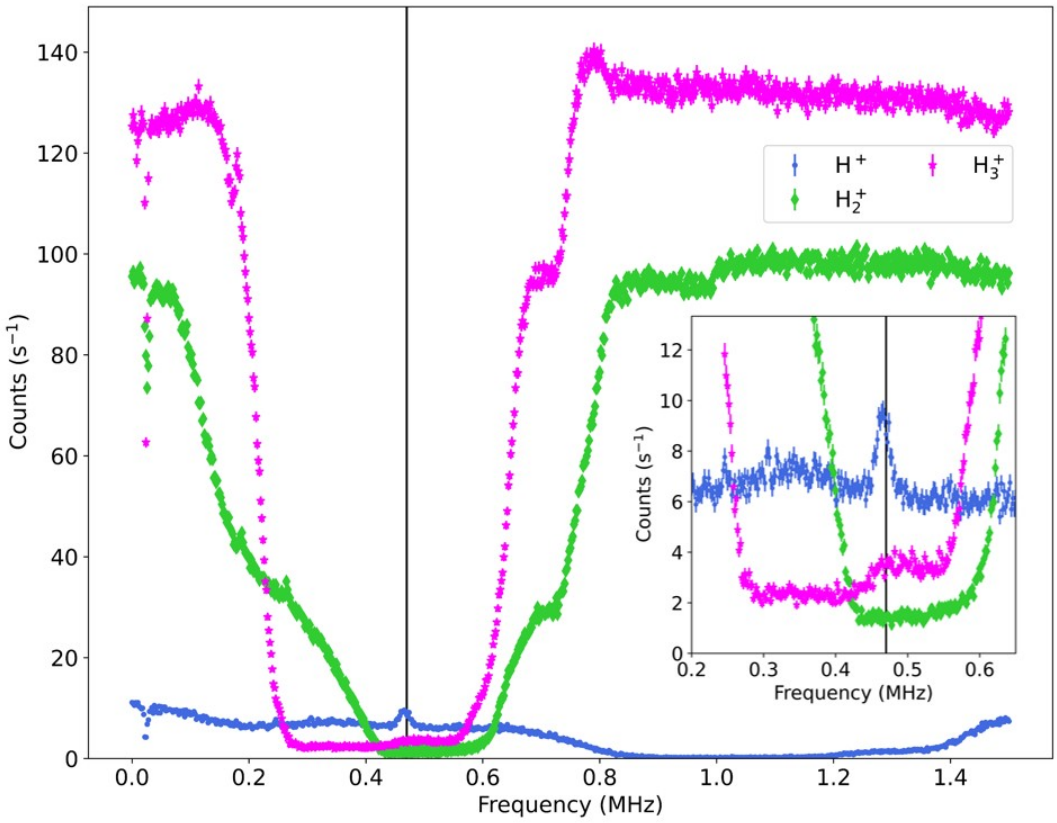

Figure 3.22: Number of H^+ (blue), H_2^+ (green) and H_3^+ (pink) as a function of RW frequency at an amplitude of 13.5 V. The solid black line shows the optimised frequency of 0.47 MHz, from [100].

Chapter 4

Positrons

As mentioned in the previous chapter, the positron system of the ASACUSA-Cusp experiment has recently been upgraded. Measurements with the FPS system at Aarhus university [105] and the specifications provided by the company indicated higher moderation and trapping efficiencies than the system previously used at ASACUSA [69]. Further, to continuously accumulate and store a large number of positrons, even when the Cusp trap is occupied due to mixing, a 3$^{\text{rd}}$ stage accumulator was installed. The system uses water-cooled magnets instead of a superconducting magnet, which removes the necessity of using $\sim 1000\,\text{l}$ of liquid Helium per week. As an additional advantage of the new system, the accumulator can be separated from the BGT by closing a GV between to pump out the cooling gases before transferring the particles into the Cusp trap.

This chapter presents the results of the measurements performed to characterise the RGM system and the BGT in Sections 4.1 & 4.2 followed by the characterisation of the accumulator in Section 4.3. Further, the operation of the FPS system at CERN is compared to the results presented at Aarhus University and a comparison of the whole positron system to the previous system used at CERN in Section 4.4. In Section 4.5 the results of measurements of positron plasma manipulation in the Cusp trap are presented.

A scale drawing of the system with the relevant detectors, pumps and apparatuses for positron measurements is shown in Fig. 4.1.

4.1 RGM-system

The ^{22}Na source was purchased in 2011 with an activity of 1.857 GBq. At the time the source was installed at CERN in 2022 it had decayed to 113.1 MBq. The moderator efficiency presented in this section was calculated using the source activity for the day the data sets were taken.

The results of the moderation efficiency, its decay rate, the axial energy spread and the radius of the slow beam are listed in Table 4.1.

During the moderator growth sequence the count rate of the slow beam was mon-

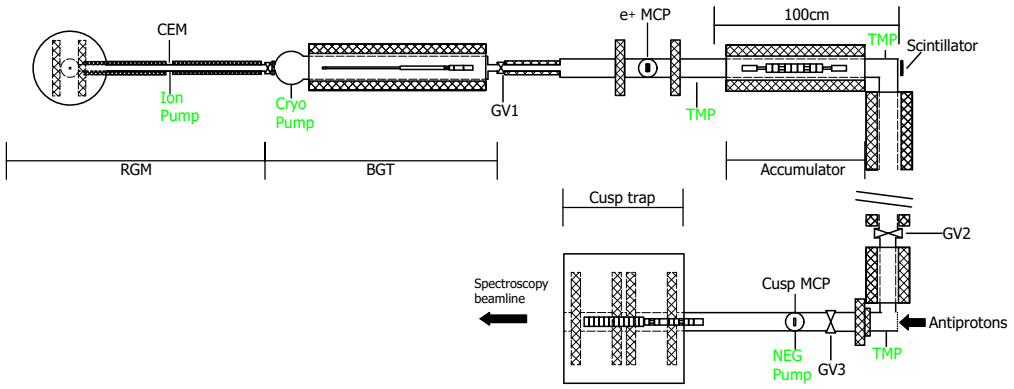

Figure 4.1: Scale drawing of the experiment with the focus on relevant information for the positron measurements. The $\sim 2.2\,m$ long transfer line setup between the positron system and the Cusp trap is shortened for visibility.

Table 4.1: Results of the RGM system and properties of the moderated positrons.

Property	Result
Moderator efficiency (%)	0.18 ± 0.04
Moderator decay (%/day)	5.59 ± 0.85
Axial energy spread (eV)	3.9 ± 0.3
Radius (mm)	2.2 ± 0.2

itored with the CsI at the gate valve between the source and the trap (labeled GV1 in Fig. 4.1). It was not possible to use the CEM because of the high pressure during the growth. Figure 4.2 shows the count rate, the pressure in the RGM system and the temperature of the moderator electrode for a typical moderator growth sequence. A full dump and grow sequence, as experimentally found to yield the highest number of moderated positrons, was as follows:

1. Dump: The Ne and possible contaminants such as N_2 from the BGT were evaporated by heating up the moderator electrode to 70 K with the ion pump off and the GV to the trap closed. The temperature was held stable at 70 K to pump the system for ten minutes with the backing TMP only before the ion pump was switched back on, the backing TMP was shut from the system, and the setup was pumped for ten more minutes. Afterwards, the coldhead was turned on to cool down to 7.5 K.

2. Stabilising: The temperature of the moderator electrode was increased to 7.8 K and was left for two minutes to stabilise. During this time the Ne line was opened to the backing pump to purge the lines.

3. Growing (orange region in Fig. 4.2): The ion pump was switched off and Ne was introduced into the source chamber at a pressure of $2 \cdot 10^{-4}$ mbar for 1000 s.

4. Annealing (purple region in Fig. 4.2): The Ne flow was stopped, the electrode was warmed up to 8.1 K and the system was left without pumping for 1000 s up to 3000 s, depending on the time available.

5. Finalising: The ion pump was turned back on and the electrode was cooled down to the operating temperature of 6.8 K.

The count rate further increased after the growth sequence was finished for several hours before the moderator started to decay with a rate of (5.59 ± 0.85) % per day when the BGT was operating.

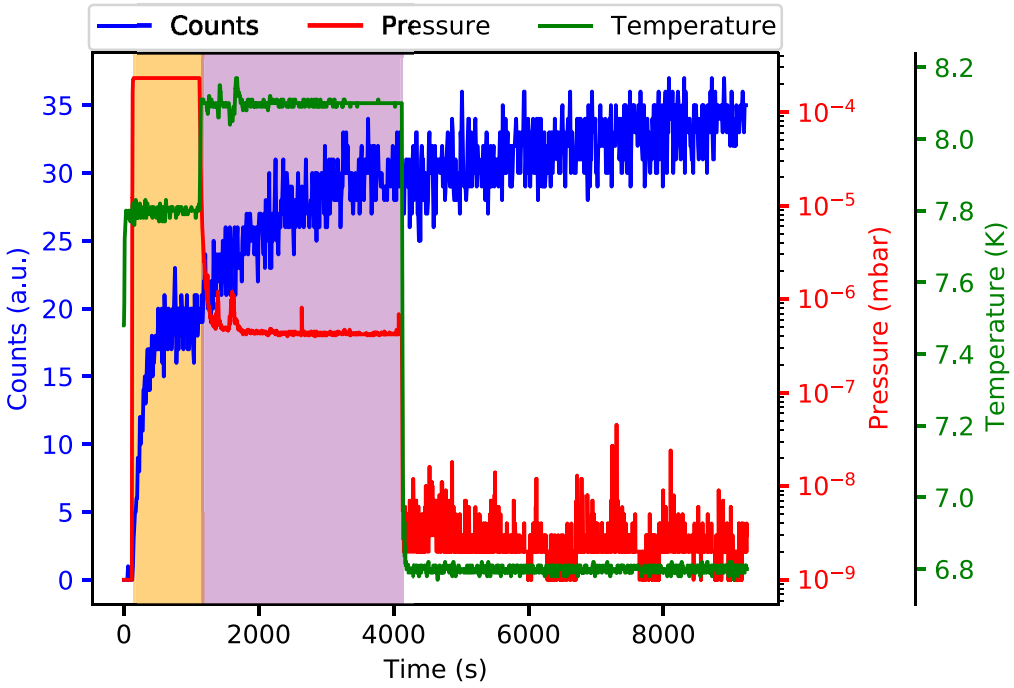

Figure 4.2: Count rate of the CsI (blue), pressure (red) and temperature (green) during a typical moderator growth sequence. The coloured areas indicate the growth (orange) and annealing (purple) phases.

4.1.1 Measurement of the number of positrons

After the growth sequence, the CEM was inserted into the beamline at the position indicated in Fig. 4.1 to measure the number of positrons. A voltage of −2100 V was applied and the mesh in front was grounded. The signal was amplified (x10) by a fast amplifier, and a quad discriminator (LeCroy NIM Model 821) was used. As described in Chapter 3.1.4, the detection efficiency was estimated by extrapolating the result in

[82] to an energy of 2100 eV, yielding (39 ± 5) %. To calculate the number of positrons the nominal 79 % transmission of the mesh was included.

The number of positrons from a newly grown moderator was $(1.6 \pm 0.2) \cdot 10^5\,\mathrm{s}^{-1}$ which equals a moderation efficiency of $\varepsilon_\mathrm{M} = (0.18 \pm 0.04)$ %.

By applying a voltage bias to the mesh a measurement of the axial energy of the moderated positrons was performed, as shown in Fig. 4.3. For this measurement the moderator electrode was biased to 60 V. The data can be fitted by the integral of a Gaussian distribution, i.e.

$$f(x) = c + A \cdot \mathrm{erf}\left(\frac{x_c - x}{\sigma\sqrt{2}}\right), \tag{4.1}$$

where the fit parameter A is the maximum number of positrons, x_c is the mean energy, and σ is the standard deviation of the distribution. The energy spread could be given in terms of the full width at half maximum (FWHM $= 2\sqrt{2\ln 2} \cdot \sigma$), which was (3.9 ± 0.3) eV with a mean energy of (61.7 ± 0.1) eV. Additionally, Fig. 4.3 shows the derivative of Eq. (4.1) in green, i.e. the Gaussian distribution of the beam.

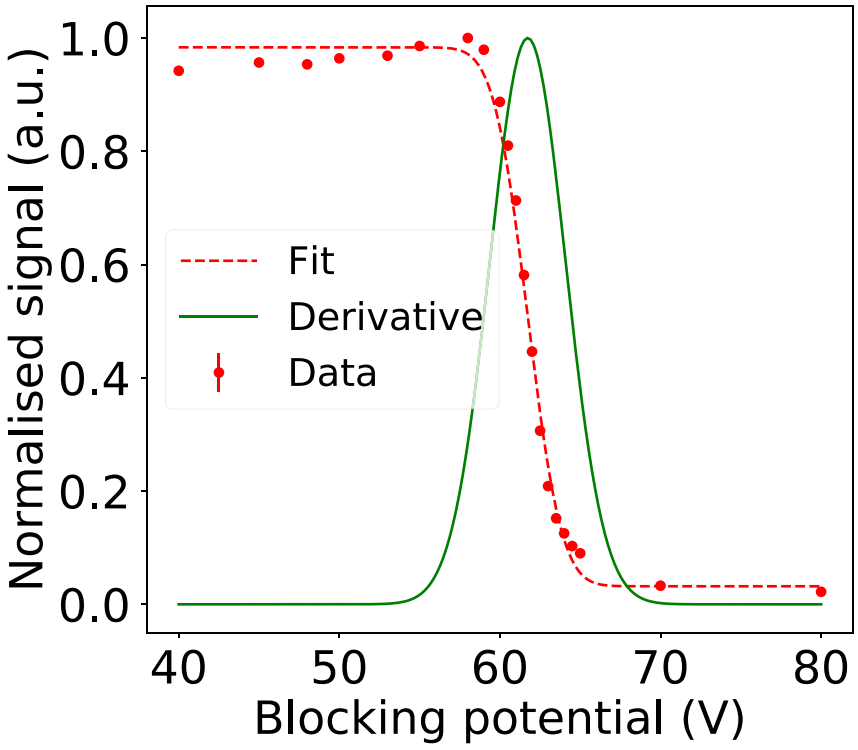

Figure 4.3: Axial energy spread of the slow beam using the CEM. The data are fitted using Eq. (4.1) (red dashed line) and additionally the derivative is shown (green).

4.1.2 Measurement of the radial profile

Figure 4.4 shows an image of the slow beam taken with the CCD camera at the positron MCP/PS biased to: MCP front: -600 V, MCP back: 600 V, PS: 1200 V. By taking an

image of the MCP plates with the known diameter of 42 mm, the pixels were converted into millimeters. The hollow center of the beam comes from the design of the moderator electrode. Positrons which left the source at an angle such that they did not interact with the neon frozen onto the cone, were not moderated.

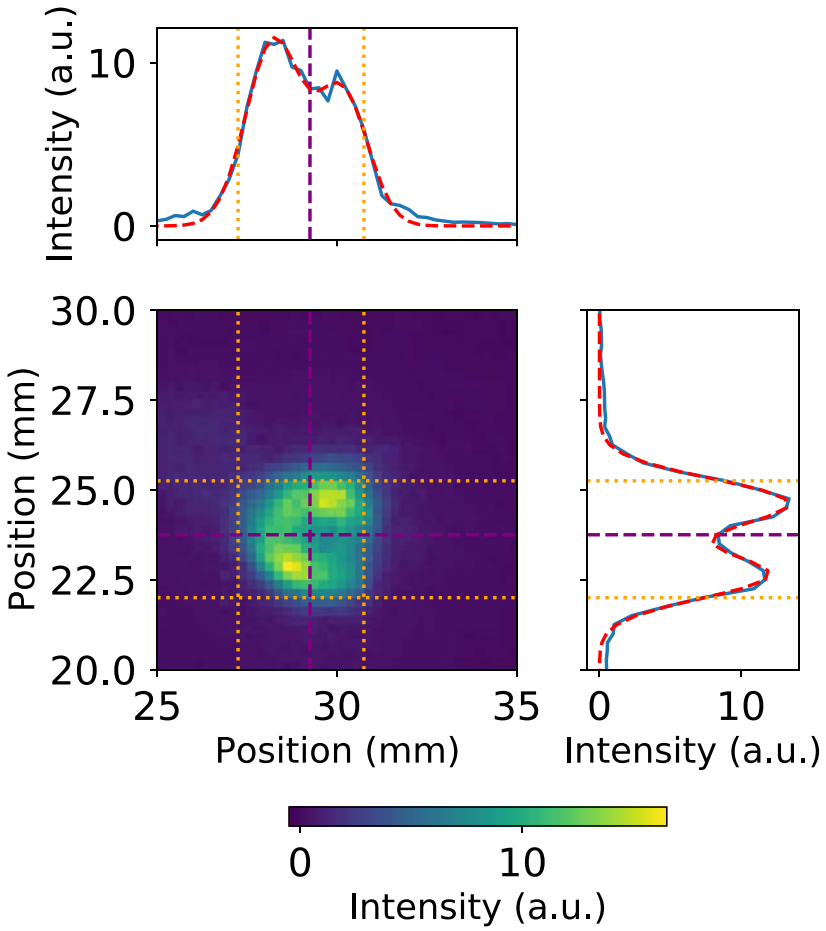

Figure 4.4: Image of the slow beam hitting the MCP/PS, taken with the CCD camera. The purple dashed lines show the cuts at which the data were fitted in the x- and y-dimension. The orange dotted lines show the position between which the radius was calculated.

In each dimension a slice of the image, as shown as the purple dashed lines in Fig. 4.4, was fitted by a sum of two Gaussian distributions

$$f(x) = A_1 \cdot e^{-\frac{(x_1-x)^2}{\sigma_1^2}} + A_2 \cdot e^{-\frac{(x_2-x)^2}{\sigma_2^2}} + c, \tag{4.2}$$

with the amplitudes A_i, the standard deviations σ_i, the means x_i for $i = 1, 2$ being the first and the second Gaussian distribution, respectively, and an offset c. A pseudo FWHM was calculated for each dimension to estimate the outer radius of the slow beam at the source: The maximum was taken as the average of the amplitudes of the two Gaussian distribution as $A = (A_1 + A_2)/2$. The minimum position values at which

Eq. (4.2) is larger than A are indicated in Fig. 4.4 as the orange dotted lines. The radii r_x and r_y were taken as half the difference between these two lines for the x- and y-dimension, respectively. The radius of the slow beam was then taken as half the squared sum of the individual radii, such that $r = \sqrt{(r_x^2 + r_y^2)/2}$.

The ratio of the magnetic field values of the source (120 G) and the detector (210 G) was taken into account to obtain the radius of the slow beam at the source as

$$\frac{r_1}{r_2} = \sqrt{\frac{B_2}{B_1}}. \tag{4.3}$$

The radius of the slow beam at the source was (2.2 ± 0.2) mm. In contrast to the presented radii, the image in Fig. 4.4 does not include magnetic field ratios, but shows the size of the slow beam on the MCP.

4.2 Buffer gas trap

The trapping efficiency, as well as the lifetime of the positrons in the trap, the axial energy spread, radius and the expansion rate of the positron cloud in the BGT are listed in Table 4.2.

Table 4.2: Trapping efficiency and properties of the positron cloud in the BGT.

Property	Result
Trapping efficiency (%)	13.8 ± 4.2
Lifetime (s)	3.0 ± 0.6
Axial energy spread (eV)	1.5 ± 0.2
Radius (mm)	2.12 ± 0.03
Expansion rate (s^{-1})	1.1 ± 0.2

The moderated positrons were magnetically guided into the BGT. Figure 4.5 shows the on-axis potential of the BGT when filling the trap and during the dump of the positrons, simulated with COMSOL [75]. The bias of the moderator electrode was 7 V, which was chosen to reduce positronium formation on the buffer gas outside the trap before positrons enter the trap electrodes.

4.2.1 Measurement of the number of positrons

The number of positrons trapped could be measured with a charge amplifier, the circuit of which is shown in appendix A.2, connected to front of the unbiased MCP. The conversion between voltage and number of positrons of this charge amplifier was $\sim$ 52000 /mV. To reduce the effect of high frequency noise 1000 data points (spanning

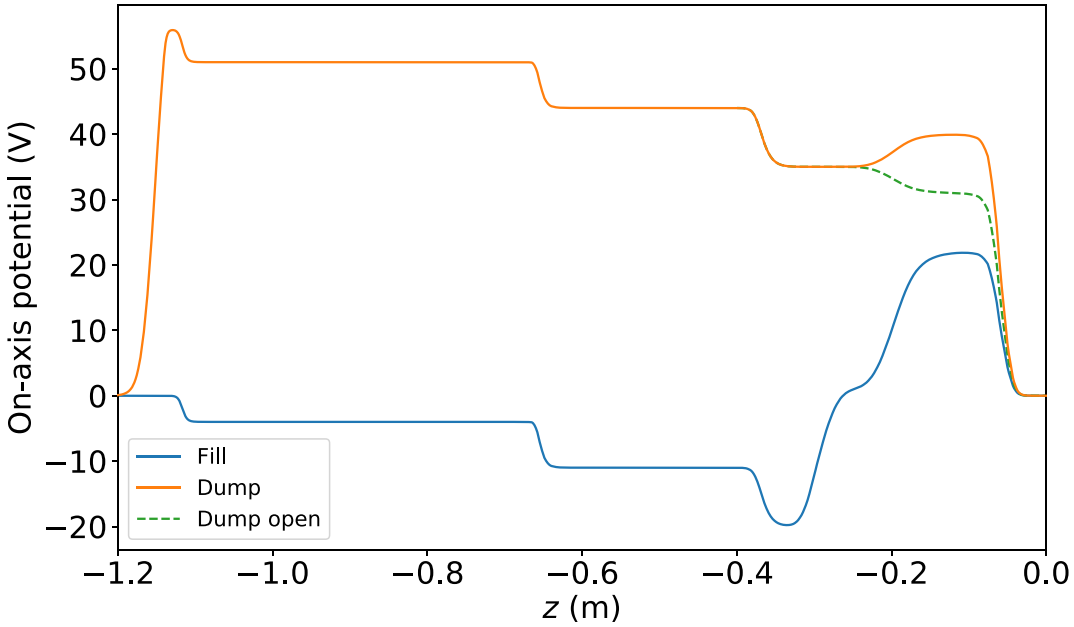

Figure 4.5: On-axis potential of the BGT during filling the trap (blue) and before dumping (orange), simulated with COMSOL [75]. The green, dashed line shows the potential when the HV pulse is applied. The moderator bias during filling was set to 7 V.

400 ns) were averaged and a squared sum of the standard deviation and the counting error, i.e. $\sqrt{N}$, was used as uncertainties. Figure 4.6 shows an example of a measurement with the charge amplifier. The red vertical lines indicate the region to calculate the weighted average of the baseline, which is shown as the red horizontal line. Additionally, the region for the signal is shown in black. The number of positrons is then proportional to the difference between the weighted average of the baseline and the signal. An overshoot was present between $t \sim 6\,\mu$s and $t \sim 12\,\mu$s even when no particles were filled into the trap and increased with larger signals, hence, this region was excluded from the analysis as shown in Fig. 4.6.

To characterise the operation of the BGT the number of positrons was measured as a function of the time in which the slow positrons were allowed to enter the trap. This fill curve is shown in Fig. 4.7.

The measured data were fitted using

$$N(t) = a \cdot (1 - e^{-\frac{t}{\tau}}), \tag{4.4}$$

yielding a lifetime τ of (3.0 ± 0.6) s.

Due to the weak source the signal was small (on the order of mV), as shown in Fig. 4.8. These small signals were in the order of low frequency noise and eight averages from the oscilloscope were taken for each of the data points to resolve the signals. As described above the signal window was chosen to avoid the overshoot. However, the later window could affect the low signals, which were sensitive to variations of

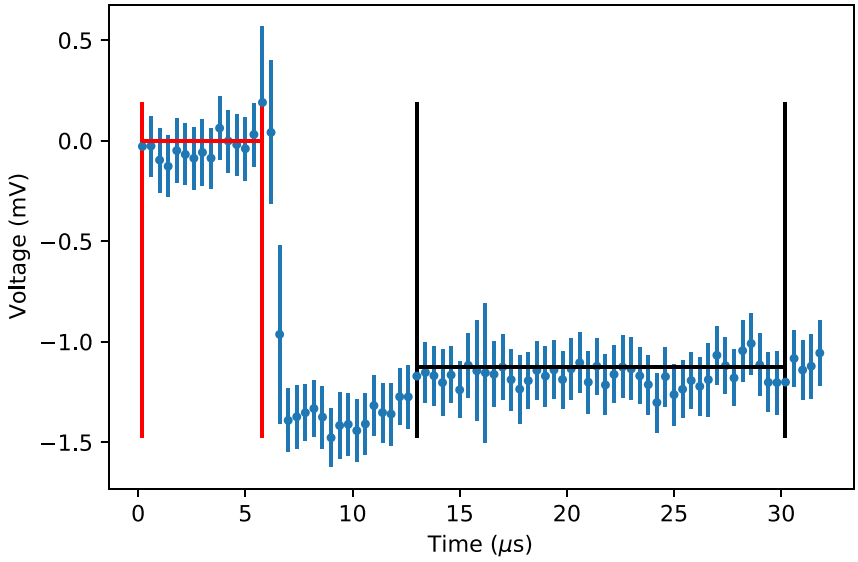

Figure 4.6: Example for the measurement of the number of positrons in a bunch accumulated for 4.5 s in the BGT. The number of positrons is proportional to the difference of the averages of the red and black region.

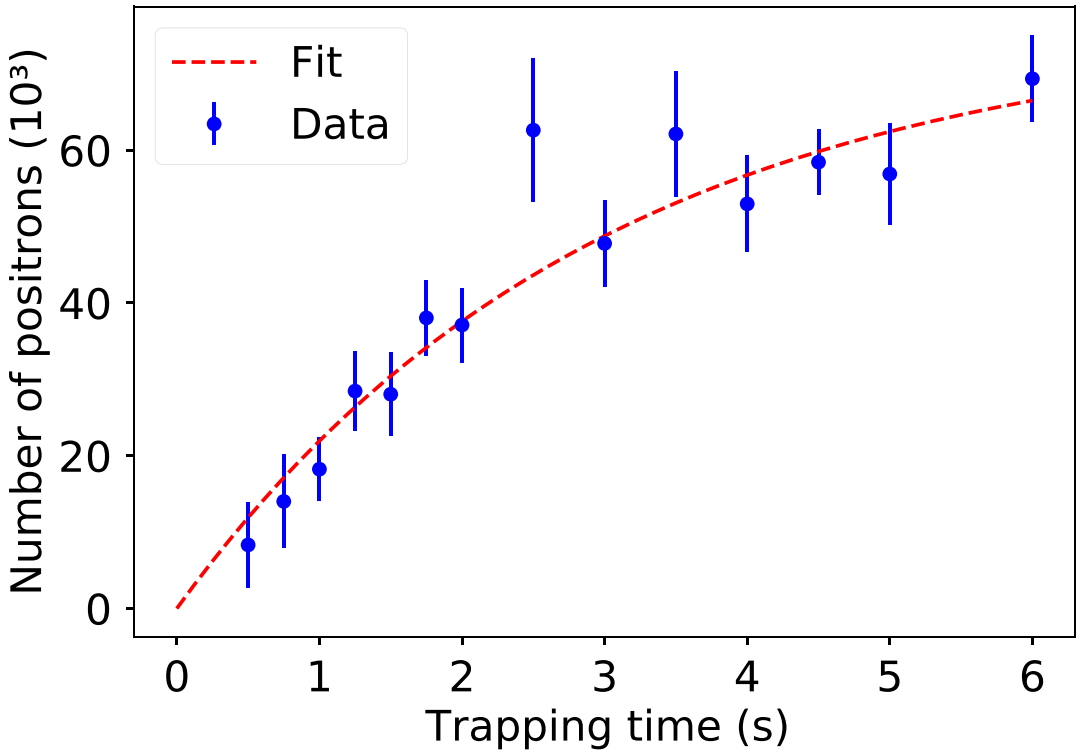

Figure 4.7: Number of positrons as a function of the accumulation time in the BGT and the fit using Eq. (4.4).

the baseline. This lead to the large scatter in the result of the number of positrons extracted from the BGT. In order to avoid the large scatter of the data, the trapping efficiency was calculated using the more conservative number of the fit result of 1 s,

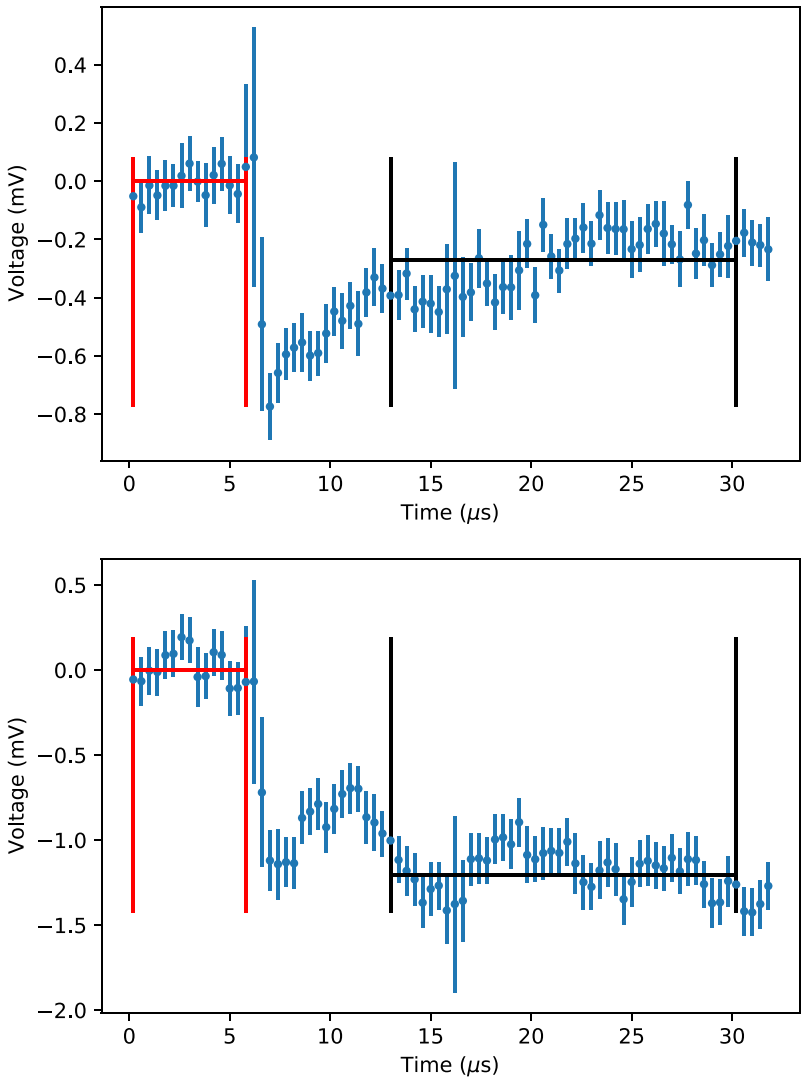

Figure 4.8: Example of the low signal for 0.75 s (top) and 2.5 s (bottom) of accumulation time in the BGT. Due to low frequency noise the analysis of the top plot tends to underestimate the number of positrons while the bottom plot tends to overestimate it.

yielding $(22 \pm 6) \cdot 10^3$ per second, which was within the error bar of the measured value of $(18.3 \pm 4.2) \cdot 10^3$. The resulting trapping efficiency was $\varepsilon_\mathrm{T} = (13.8 \pm 4.2)\,\%$, which lies within the specification given by the manufacturer of 17 %.

The axial energy spread of the positrons extracted from the BGT was measured by using the first electrode of the accumulator as a retarding potential analyser and acquiring the annihilation signal of the positrons at the corner after the accumulator. The result is shown in Fig. 4.9, yielding a FWHM using Eq. (4.1) of $(1.5 \pm 0.2)\,\mathrm{eV}$.

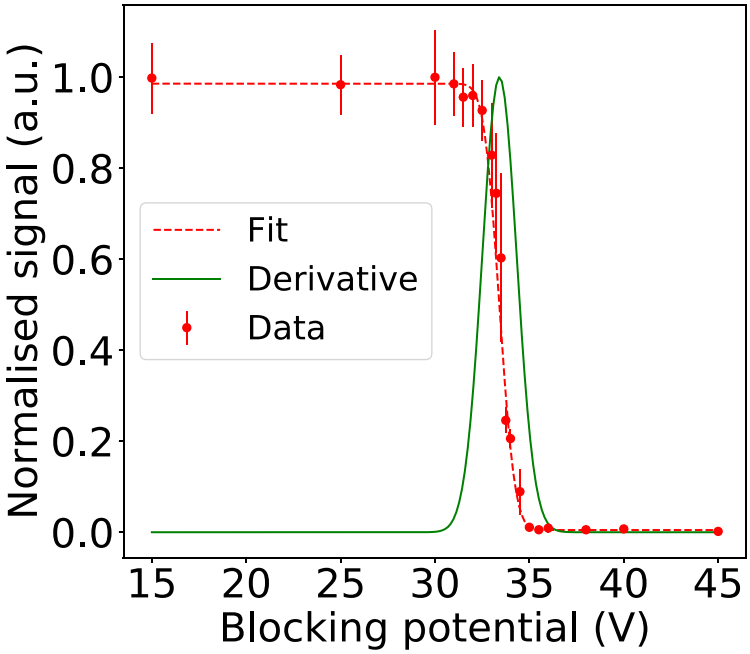

Figure 4.9: Axial energy spread measurement of the bunched positrons. The data are fitted using 4.1 (red dashed line) and the derivative is shown (green).

This large energy spread might be a result of the extraction method of pulsing down the blocking potential, causing the well well to be sloped, as shown in Fig. 4.5, instead of pushing the particles out by raising the bottom of the well to a flat potential. However, at CERN the energy spread and hence the time spread of the positrons when reaching the accumulator, was not important, as the catching potential of the latter could be held open long enough to catch the pulse without letting positrons escape.

4.2.2 Measurement of the radial profile

By imaging the positrons from the BGT the radius of the positron cloud was measured, as shown in the left image of Fig. 4.10.

The radius of the spot was fitted by a 2D-Gaussian distribution

$$f(x,y) = y_0 + A \cdot \frac{e^{-\left(\frac{(x-x_c)^2}{2\sigma_x^2}+\frac{(y-y_c)^2}{2\sigma_y^2}\right)^p}}{2\pi\sigma_x\sigma_y} \tag{4.5}$$

with the background intensity y_0, the amplitude A, the power of the Gaussian p (which was introduced to allow for oval profiles due to misalignment of the camera), the center i_c and the radii σ_i, where $i = x, y$ are the two dimensions. The presented

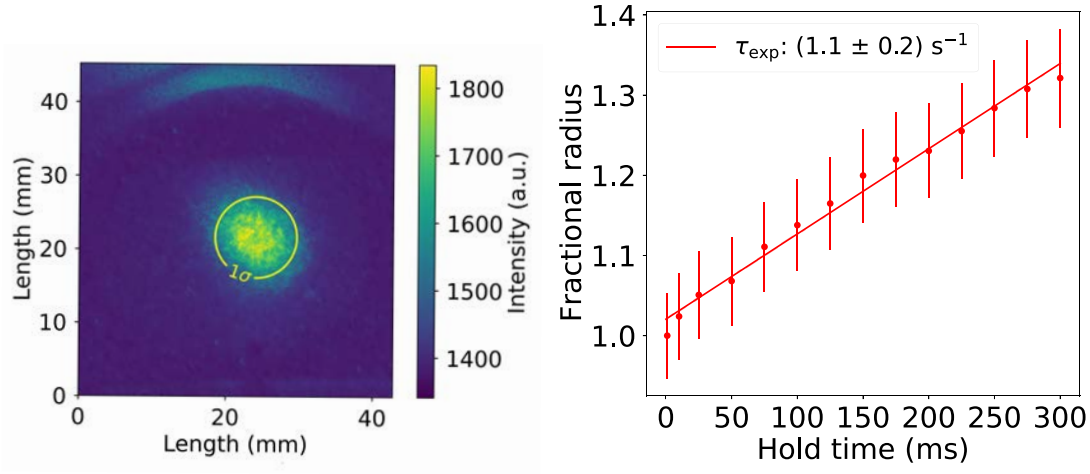

Figure 4.10: Left: Image of the positron cloud on the MCP with the one sigma result of the 2D-Gaussian fit of Eq. (4.5).
Right: Measurement of the expansion rate τ_{exp} of the positron cloud in the BGT.

radii are calculated as $r = \sqrt{(\sigma_x^2 + \sigma_y^2)/2}$. Taking the magnetic field ratio of the trap (750 G) and the detector (210 G) into account, the resulting radius was (2.12 ± 0.03) mm. To show the effect of the buffer gas on the radius of the positrons, an expansion rate was measured by turning off the RW electric field after accumulation and holding the positrons a variable amount of time. The fast expansion rate of $(1.1 \pm 0.2)\,\mathrm{s}^{-1}$, as shown in the right plot of Fig. 4.10, was due to the high pressure in the system, which was necessary to trap and cool the positrons.

4.3 Accumulator

The results of the single bunch transfer efficiency into the accumulator, the lifetime, the radius, and the expansion rate of the positron cloud are listed in Table 4.3.

Table 4.3: Single shot efficiency into, and properties of the positron cloud from, the accumulator. The lifetime and expansion rate were measured with the gate valve (GV2 in Fig. 4.1) being open/closed. The range of the radius presented corresponds to the number of stacks from 5-160.

Property	Result
Single shot efficiency (%)	90 ± 8
Lifetime (s)	104 ± 22 / >600
Radius (mm)	1.44 ± 0.05 - 1.85 ± 0.06
Expansion rate (s^{-1})	0.028 ± 0.002 / 0.008 ± 0.001

The positrons were magnetically guided from the BGT into the accumulator. 5 ms before the positrons were extracted from the BGT the potential shown as the blue solid

line in the top plot of Fig. 4.11 was applied such that the positrons were held in the minimum on-axis potential on the US side of the trap. Catching was performed by pulsing down the potential of the US catching electrode for 800 ns using a HV pulser, as shown as the green dashed line in the top plot of Fig. 4.11. Even though the accumulator trapping well is fully opening to the US side, and therefore one might expect that most of the caught positrons escape the well, it was experimentally found to yield the highest number of positrons over the tested range of number of stacks. This could be explained by the low energy of the stored positrons. In 800 ns the positrons at room temperature travel ~ 5 cm, which is too short to to be able to leave the trap on the US side.

During storage a RW electric field with a frequency of 100 kHz and an amplitude of 10 V was applied to compress the particles. As the MCP could be rotated to face the entrance of the accumulator it was possible to use the same techniques and detectors for the accumulator, by extracting the particles to the US side of the apparatus, which had been used for the BGT. For normal operation, i.e. the transfer of positrons into the Cusp-trap, the potential shown as the orange line in the bottom plot of Fig. 4.11 was applied after the last stacking cycle. The positrons were extracted by applying a fast pulse onto the electrode C9, resulting in the blue dashed line in the bottom plot of Fig. 4.11.

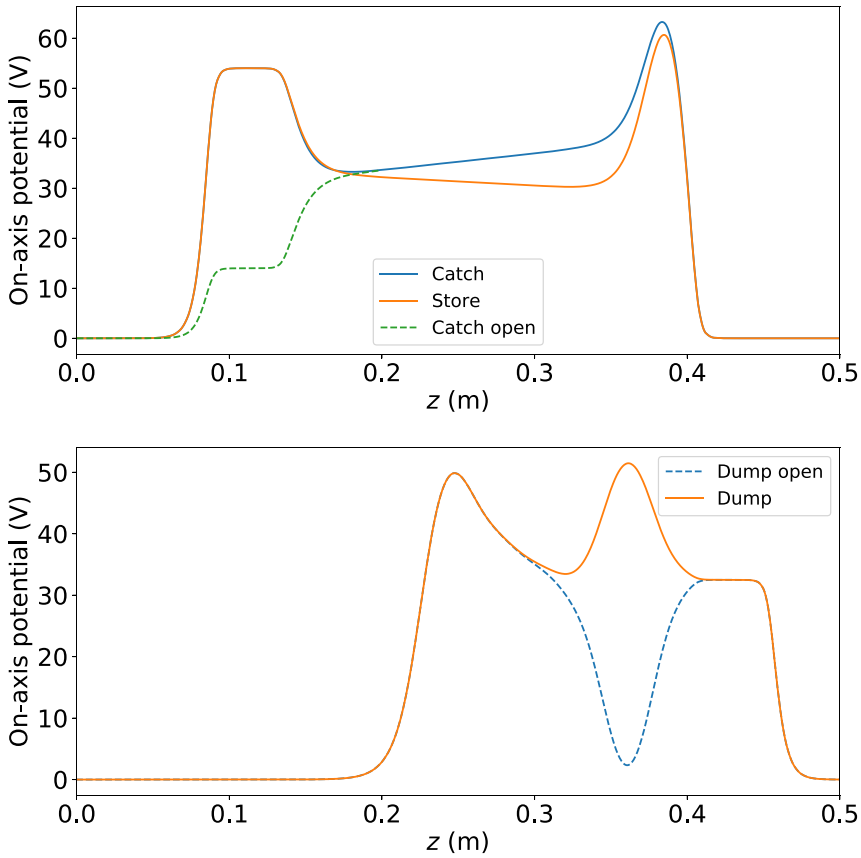

Figure 4.11: Top: Simulated on-axis potential during the catch (blue) and storage between the bunches from the BGT (orange). The green dashed line shows the potential well during the catch being applied for 800 ns.
Bottom: Simulated on-axis potential before the dump into the Cusp trap. The dashed potential shows the open well to dump the positrons.

4.3.1 Measurement of the number of positrons & radial profile

As mentioned above, the main purposes of the accumulator was to catch and store several bunches of positrons from the BGT during the time the antiprotons were decelerated and prepared for mixing. Therefore, the number of positrons as a function of stacks was measured, as shown in Fig. 4.12.

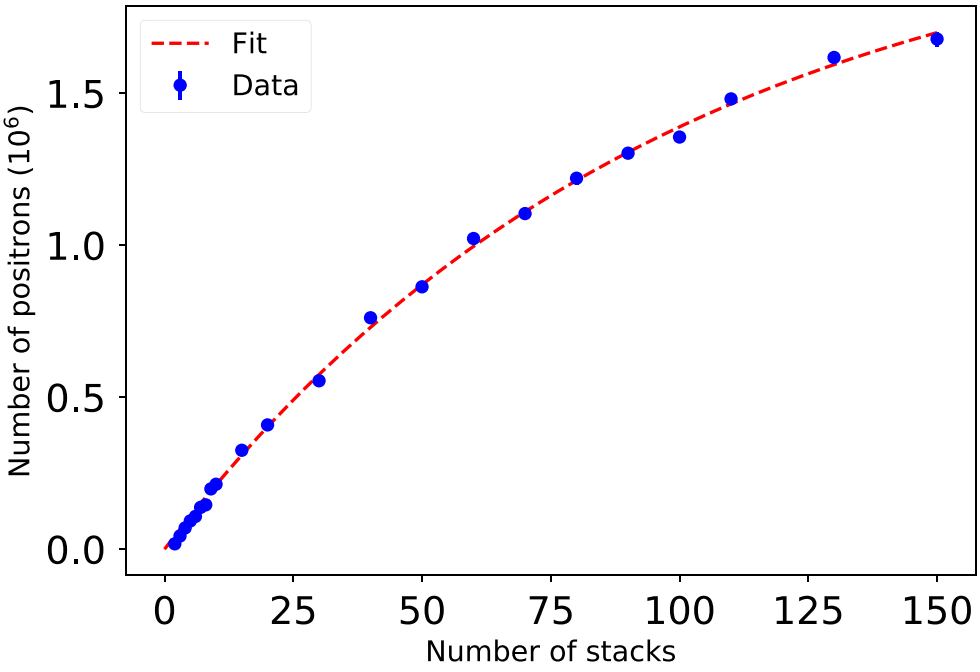

Figure 4.12: Number of positrons as a function of stacking cycles.

The measurement follows the description given in 4.2.1. However, the signal of positrons from the accumulator on the MCP with a large number of stacks was large enough to be resolved without averaging, hence it was decided to make only one measurement of the stacking instead of oscilloscope averaging. However, the signal of one stack was too small to be resolved without averaging, and therefore a different approach was taken to calculate the single shot efficiency of the accumulator: The increase in the number of positrons up to 20 stacks could be approximated by a linear function, with the slope being proportional to the number of positrons in a single shot from the BGT. To estimate the single stack efficiency, the number of positrons per stack was calculated in this region by $N(x)/x$, where x is the number of stacks. This was divided by the number of positrons from the BGT of $(22 \pm 6) \cdot 10^3\,\mathrm{s}^{-1}$, presented in the preceding section. The result of the single shot efficiency as a function of number of stacks can be seen in Fig. 4.13. Low frequency noise affected the small signals and resulted in an underestimate of the number of positrons, as can be seen in the figure. The data for two and three stacks were therefore excluded from further analysis. The large uncertainties in Fig. 4.13 is due to the large uncertainty of the number of positrons in one bunch from

the BGT.

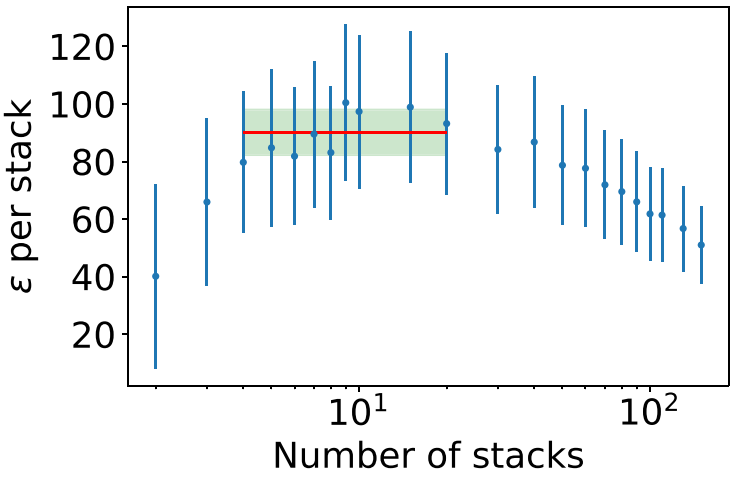

Figure 4.13: Single shot efficiency as a function of number of stacks. The red horizontal line and the green shaded area are the weighted mean and uncertainty of the efficiency calculated in the indicated region.

The weighted average in the region of four to 20 stacks was calculated to get a single shot efficiency of $\varepsilon_{\text{acc}} = (90 \pm 8)\,\%$, yielding $(19.8 \pm 1.8) \cdot 10^3$ positrons per stack.

Approximately one million positrons could be stacked in about 60 s. For further characterisation a lifetime curve was performed using 60 stacks which were held in the accumulator for a variable amount of time. This measurement was repeated when the gate valve between the accumulator and the BGT (GV2 in Fig. 4.1) was closed before holding the particles. This test was performed to verify that the lifetime without gas in the trap is sufficiently long to pump out the gas before extraction to the Cusp trap, which was necessary to minimise the contamination of the vacuum. The lifetime of the positrons was $(104 \pm 22)\,\text{s}$ when the gate valve was left open, as shown on the left hand side of Fig. 4.14. By having it closed the positron lifetime increased such that after 600 s more than 95 % of the positrons were still present in the trap. That is far longer than the typical time needed for pumping out the gas from $2 \cdot 10^{-7}\,\text{mbar}$ to $< 1 \cdot 10^{-8}\,\text{mbar}$, which took about 3 s.

The expansion rate could be measured with the gate valve open or closed as well to see the influence of the gas on the evolution of the radius of the positron cloud. For that measurement the gate valve was left open or was closed before turning the RW off. The starting radius using 30 stacks was $(1.63 \pm 0.04)\,\text{mm}$. The resulting rates were $(0.028 \pm 0.002)\,\text{s}^{-1}$ (open) and $(0.008 \pm 0.001)\,\text{s}^{-1}$ (closed). The results are shown on the right hand side of Fig. 4.14.

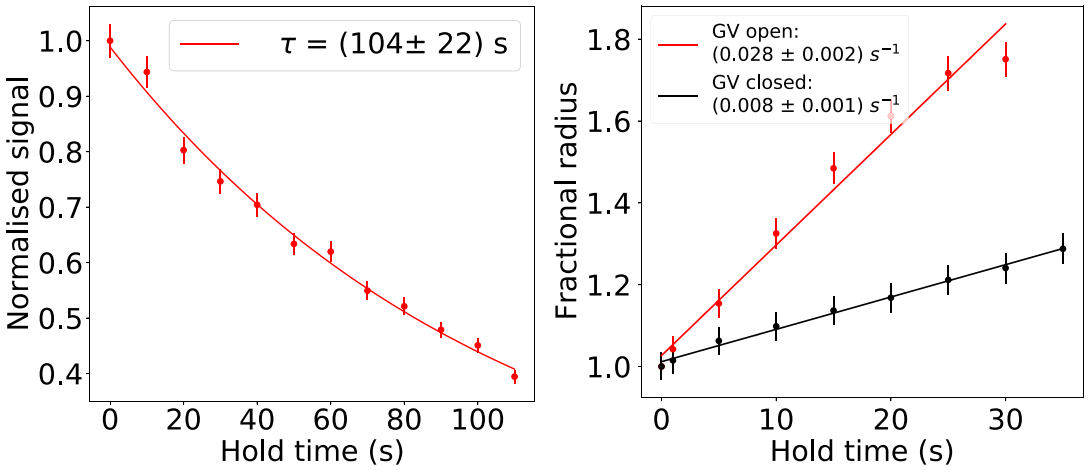

Figure 4.14: Left: Lifetime curve of the positrons in the accumulator. Right: Expansion curves of the positron cloud in the accumulator after turning the RW electric field off having the gate valve open (red) and closed (black).

4.3.2 Measurement of the temperature

The accumulator does not use an additional SF_6 supply for cooling the positrons. It was assumed that enough cooling gas is provided from the BGT. To check this assumption the temperature of the positrons was measured.

The analysis of the temperatures follows the description in [106]. To measure the temperature of a plasma the particles were extracted slowly onto the MCP by ramping down the blocking potential of the trapping well. As described in Chapter 2.2.1, the temperature of a plasma follows a Maxwell-Boltzmann distribution. The signal of particles arriving at the MCP is $\propto e^{-mu^2/(2k_BT)}$). The extraction needs to happen on a time scale much slower than the bounce frequency of the particles in order to energy-resolve the particle flux but much faster than the time it takes for instabilities to develop and re-thermalisation to occur [107]. Further, only the first particles escaping from the center of the plasma are used for the temperature analysis, for which the change in the space charge is significantly small [107].

As a first step, the time-dependent signal from the MCP was binned and converted into a space-charge dependent signal. For that purpose, the ramped dump potential applied to the extraction electrode was monitored and mapped to a calculated on-axis potential. To find the region in which the signal increases exponentially due to the Maxwell-Boltzmann distribution, the data were fitted in several windows from $V(t_0)$ up to $V(t_i)\epsilon[V(t_-) : V(t_+)]$ by

$$f_i(V_i) = e^{a_i \cdot (V(t_i) - b_i)} + c_i. \tag{4.6}$$

$V(t_-)$, shown as the purple vertical line in the top plot of Fig. 4.15, was chosen such that the signal was significantly higher than the scatter of the baseline. This was implemented as $c_i + \xi \cdot \sigma$ where ξ is a parameter which was typically ~ 20 and σ was

the standard deviation of the baseline. $V(t_+)$, shown as the orange vertical line in the top plot of Fig. 4.15, was a fraction of the maximum of the saturating signal, typically $\sim 20\,\%$. The starting value of the fit region $V(t_0)$, shown as the green vertical line in Fig. 4.15, was chosen to be a time t_0, about 0.1-1 ms, before $V(t_-)$. From each of these fits the temperature was calculated by comparing the exponent of the fit to the exponent of a Maxwell-Boltzmann distribution, i.e.

$$T_i = \frac{e}{k_\mathrm{B} \cdot a_i}. \tag{4.7}$$

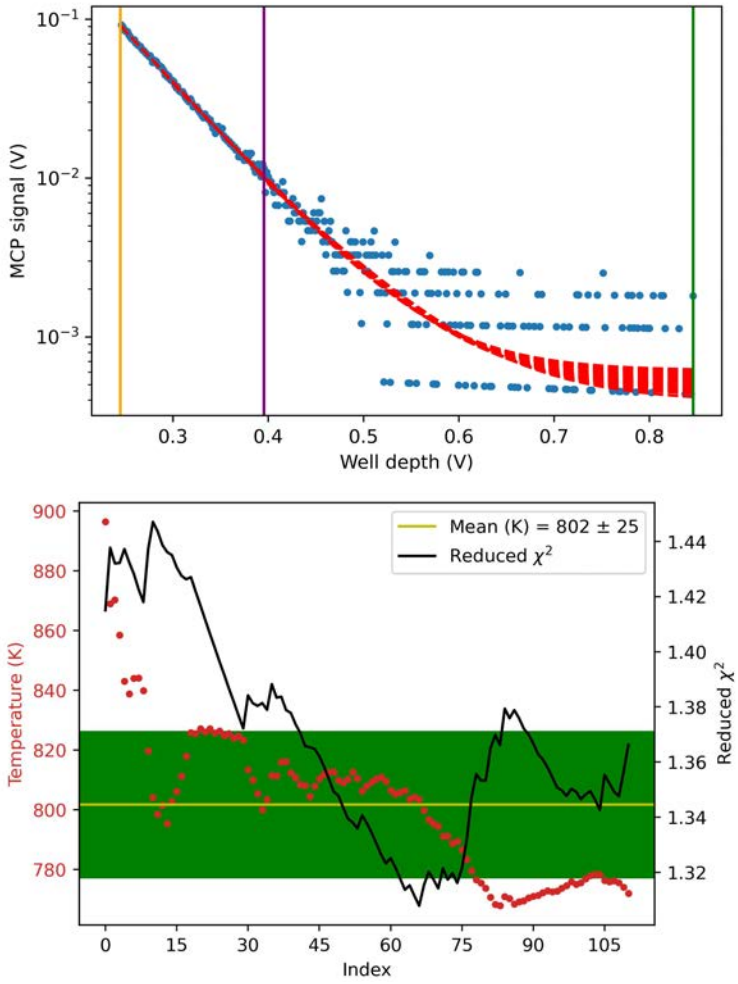

Figure 4.15: Example of the temperature analysis.
Top: Exponential fits (red) of the MCP signal (blue) for the different fit regions. The vertical lines are $V(t_0)$ (green), $V(t_-)$ (purple) and $V(t_+)$ (orange).
Bottom: Weighted average of the resulting temperatures for the fits in the top plot and the corresponding reduced χ^2. The x-axis "index" indicates the number of fit window. Index 0 is the temperature result fitting the data in the range of $V(t_0)$ to $V(t_-)$ and the last index is the result when fitting the data from $V(t_0)$ up to $V(t_+)$

The final temperature was obtained by a weighted average of the temperatures of each fit of the intervals, with the weights being the exponential of the normalised log-

likelihood $\exp|-\chi^2_{\text{red}}/2-0.5|$, where χ^2_{red} is the reduced chi square of the individual fits. These weights ensure that the fits for $V(t_i) \to V(t_-)$, which get worse, are weighted less [106]. An example of the fits and the resulting temperature is shown in Fig. 4.15.

When GV2 was open the positrons were already at room temperature when the RW was applied with no additional waiting time, hence, it was not possible to measure a cooling curve. However, this showed that enough cooling gas was present in the system. For the case that GV2 was closed, the positrons were heated up for 9 s by applying a RW electric field after GV2 was closed. The resulting curve, yielding a cooling rate of $(0.74 \pm 0.13)\,\text{s}^{-1}$, is shown in Fig. 4.16. The calculated cyclotron cooling rate of positrons in a 1100 G magnetic field was $0.0026\,\text{s}^{-1}$ which was much slower than the measured cooling rate. This indicates that even after 9 s of pumping out the cooling gas of the accumulator to a pressure of low 10^{-9} mbar, sufficient gas was in the system to speed up the cooling of the positrons. The measurement showed that it is possible to further decrease the amount of gas in the accumulator, which would lead to an increase in the lifetime of the positrons. However, the only option to decrease the gas supply was to install a pumping restriction and therefore break the vacuum, hence this intervention was postponed.

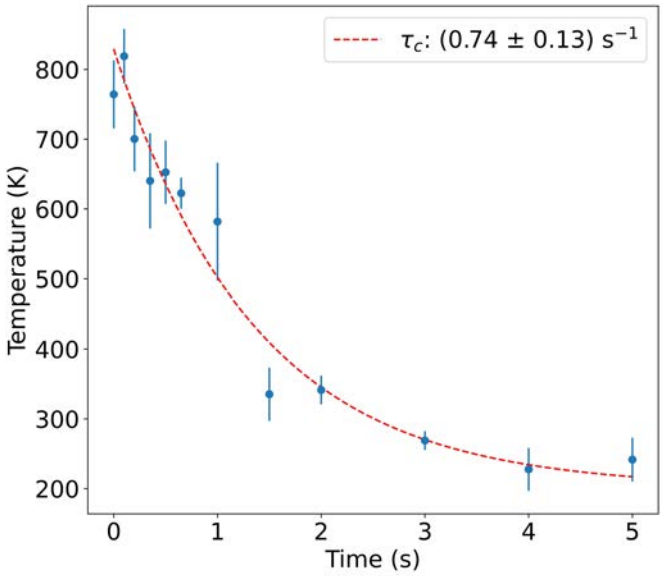

Figure 4.16: Cooling rate τ_c of the positrons in the accumulator when GV2 was closed and after 9 s of heating by applying a RW electric field.

4.4 Comparison to previous measurements

Because the results of operation of the system previously used at CERN [69], and of the FPS system used at Aarhus University [105, 108] are published, it is possible to make a comparison of the efficiencies of the system.

4.4.1 Operation of the RGM & BGT

The results of the FPS efficiencies from Aarhus University [105, 108] , the specification given by the company, and of this work at CERN are listed in Table 4.4.

Table 4.4: Comparison of the efficiencies and number of positrons provided in the specifications given by First Point Scientific Inc. and measured at Aarhus university and CERN. The listed repetition rates are the full cycle for one positron bunch including the fill time, cooling and dump process. The specifications do not give the fill time but only the repetition rate and no final number of positrons.

	Specifications	Andersen [105]	This work
^{22}Na activity (MBq)	Scaled to 1850	888	86
Slow beam (s^{-1})	$7 \cdot 10^6$	$4 \cdot 10^6$	$(1.6 \pm 0.2) \cdot 10^5$
ε_M (%)	0.38	0.5 (/0.4[1])	0.18 ± 0.04
ε_T (%)	17	35	13.8 ± 4.2
Fill time (s) / repetition rate (Hz)	– / 5	0.35 / 2.2	1 / 0.925
Number of positrons ($bunch^{-1}$)	–	$500 \cdot 10^3$	$(22 \pm 6) \cdot 10^3$

One observation is that the source activity decreased by roughly a factor of ten from Andersen to this work, however, the measured number of slow and trapped positrons (compared for an accumulation time in the BGT for 1 s) decreased by a factor of ~ 25 and ~ 60, respectively. This opened the question, if the system operates less efficiently after installation at CERN or if either of the numbers were over- or underestimated. The main difference in the two setups was that the number of positrons was measured directly at CERN, the slow beam with the CEM and the number of positrons per bunch with a charge amplifier. At Aarhus University the measurement of the slow beam was performed by counting annihilation signals on a gate valve using a NaI, where the detection efficiency of positrons was calibrated using a ^{137}Cs source with known activity. The efficiency presented in [105] differs from [108] (0.5 % and 0.4 %), although presenting the same number of positrons. Additionally, no uncertainties were given on these numbers and therefore one cannot estimate the accuracy of the calibration and the measurement. However, as the nominal moderation efficiency given by FPS is 0.38 %,

[1]This number was presented in [108]. The number of positrons in the thesis and the publication are the same, however, the moderation efficiencies differ.

it is believed that the slow beam production could be increased at CERN.

As mentioned above, the number of positrons from the pulsed systems at CERN was measured by the charge deposited on an unbiased MCP and the trapping efficiency was calculated by dividing the number of positrons trapped by the measured number of particles in the slow beam. The gain of the charge amplifier was verified by measuring a well defined number of electrons on the Cusp trap MCP. The measured value of $(13.8 \pm 4.2)\,\%$ agrees within the uncertainty with the specification of $17\,\%$.

In [105] the presented trapping efficiency is $35\,\%$, which is twice as high as the specification. To calculate the performance of the trap the slow beam and the trapped bunch were measured with a PS biased to -6 kV and a CCD camera. The light was acquired in both cases for 5 s and the time of filling the trap was taken into account. The efficiency was calculated as $\varepsilon_{\text{trap}} = \frac{N_{\text{bunch,CCD}}}{N_{\text{cont,CCD}}} \cdot \frac{t_{\text{cycle}}}{t_{\text{fill}}}$, where t_{cycle} is the whole cycle time including the cooling and dumping phase and t_{fill} is the time the trap is open. This technique has two important requirements: the PS and the camera must not saturate and all the particles of the slow beam which would be trapped have to pass through the trap. If one of these requirements is not fulfilled, the resulting trapping efficiency would have been overestimated. The type of the PS is not documented and as it is not mentioned if the measurement was repeated with a lower bias on the PS or lower exposure time resulting in the same trapping efficiency, saturation effects cannot be excluded.

To conclude this section, as the specifications and the measurement performed at Aarhus university of the moderator efficiency were at least a factor of two higher, it should be possible to increase the moderator efficiency by optimising the parameters during the growth. The trapping efficiency on the other hand, agreeing with the specifications, is believed to be close to maximum and that it was overestimated in the previous results.

4.4.2 Previous positron system

A comparison of the efficiencies measured with the system used previously at CERN [69] and the FPS & accumulator system is presented in Table 4.5.

Taking the efficiency only, the two systems operate comparably well. Therefore the upgrade was a success, as the number of positrons stayed similar, but the upgraded system has the following advantages:

- The accumulator opens up the option to continuously stack positrons, even in times the Cusp trap is occupied during mixing, which was not possible with the previous system, which had down times during mixing.

- Water cooling of the magnets is sufficient, hence no liquid helium is used anymore to cool the BGT magnet.

Table 4.5: Comparison of the moderator efficiency (ε_M), the trapping efficiency (ε_T), the accumulator single stack efficiency (ε_{acc}) and the transfer and catching efficiency in the Cusp trap (ε_{xfer} & ε_{catch}) of the system previously used and the upgraded FPS & accumulator system. Additionally, the combined trapping and moderator efficiency is shown as a comparison.

Property	Previous system [69]	RGM & BGT	Accumulator
ε_{M} (%)	0.25 ± 0.1	0.18 ± 0.04	–
ε_{T} (%)	17.4 ± 1.8	13.8 ± 4.2	–
$\varepsilon_{\mathrm{acc}}$ (%)	–	–	90 ± 8
$\varepsilon_{\mathrm{xfer}}$ & $\varepsilon_{\mathrm{catch}}$ (%)	50 ± 5	–	71 ± 27
$\varepsilon_{\mathrm{M}} \cdot \varepsilon_{\mathrm{T}}$ (%)	0.044 ± 0.018	0.025 ± 0.010	–

- The moderator decay of the upgraded system is $\sim 5\,\%$/day compared to $\sim 16\,\%$/h in the previous system. A new moderator has to be grown less often and therefore gives more time to perform experiments.

However, improvements of the new system are possible. First of all, it might be possible to increase the moderator efficiency as it is lower than the value in the specification. Spending time on optimising the parameters of the growth sequence or the transport between the source and the trap might yield an increase. However, a new 1.87 GBq source was ordered which arrived at CERN last year. The number of positrons available should increase by a factor of ~ 25, which makes the reduced efficiency less important.

Second, the pressure in the accumulator is quite high during stacking, which reduces the lifetime of positrons. A pumping restriction should be installed as it was shown that even when the gate valve between the BGT and the accumulator was closed the cooling of positrons was sufficiently fast after 9 s of pumping the gas out.

4.5 Positron plasma manipulation

This section describes the results of the preparation of the positron plasma in the Cusp trap for antihydrogen production. The main focus lies on the results taken with the new positron system in the upgraded Cusp trap. However, one important measurement was taken when the previous positron system [69] was installed, which was a proof of understanding of the temperature evolution of a non-neutral plasma in a highly inhomogeneous magnetic field.

4.5.1 Temperature evolution

The temperature evolution of a positron plasma after heating and cooling was measured in trap II. At the time of the measurement one of the two cryo cooler was broken, leading

to a temperature of the electrodes of $\sim 70\,\mathrm{K}$ and consequently a high positron plasma temperature to which it can relax to.

To measure the cooling rate, which is shown as the blue data set in Fig. 4.17, the positrons were heated by applying a RW with a frequency of 3 MHz and an amplitude of 4 V for 20 s. Afterwards, the RW was stopped and the positrons cooled via cyclotron cooling in the average magnetic field of 1.4 T. To measure the heating rate, as shown as the red data set in Fig. 4.17, the positrons were prepared the same way but were left for 8 s in the potential well after the RW was turned off and then evaporatively cooled for 100 ms. In both cases the positrons were left a variable amount of time in the trap before the temperature was measured in the same way as described in Section 4.3.2.

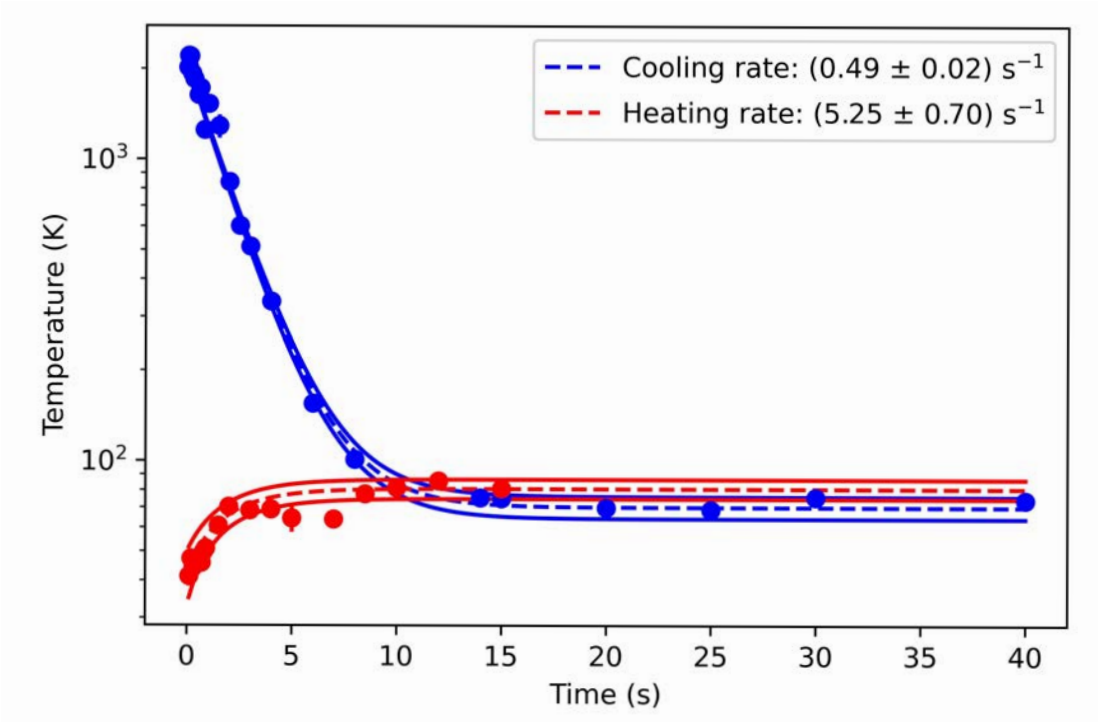

Figure 4.17: Temperature evolution of the positrons in the Cusp trap after being heated (blue) and after EVC (red). The dashed lines are fits using Eq. (4.8) *and the solid lines represent the error of the fit.*

This measurement showed that it was possible to perform EVC in the strong magnetic mirror field of the Cusp trap to reach a low temperature positron plasma. The data were fitted using an exponential function $T(t) = a \cdot \exp(-b \cdot t) + c$ and the parameters were compared to Newton's law of cooling

$$T(t) = T_\mathrm{W} + \frac{H}{G} + \left[T_i - \left(T_\mathrm{W} + \frac{H}{G}\right)\right] e^{-Gt}, \tag{4.8}$$

where $T_\mathrm{W} = 70\,\mathrm{K}$ was the measured wall temperature, T_i the measured initial temperature, G the cyclotron cooling rate and H the heating rate. The resulting cyclotron cooling rate of $(0.49 \pm 0.02)\,\mathrm{s}^{-1}$ was in good agreement with the theoretical

value of $0.51\,\mathrm{s}^{-1}$ for positrons in a magnetic field of 1.4 T. The measured heating rate was $(5.25 \pm 0.70)\,\mathrm{K\ s}^{-1}$. An expansion curve was measured by imaging the positrons after a variable amount of time on the MCP/PS to verify that the increase in temperature was caused by expansion heating of the plasma. The resulting expansion rate was $\tau_{\mathrm{exp}} = (0.019 \pm 0.001)\,\mathrm{s}^{-1}$. The number of positrons was $1.5 \cdot 10^6$, the radius was measured to be $r_{\mathrm{p}} = 1.6\,\mathrm{mm}$ and the length was estimated by the applied trapping potential to be 10 cm. From that it was possible to estimate the expected heating rate by using the plasma rotation frequency $\omega_{\mathrm{r}} = n \cdot e/(2\varepsilon B)$ and the rate of change of the angular momentum $\mathrm{d}P/\mathrm{d}t = 2 \cdot \tau_{\mathrm{exp}}(eB/2) \cdot r_{\mathrm{p}}^2 N$ [109]

$$H(\mathrm{K/s}) = \omega_{\mathrm{r}} \frac{\mathrm{d}P}{\mathrm{d}t} \frac{2}{3Nk_{\mathrm{B}}} \tag{4.9}$$

to be $H = (6.3 \pm 0.4)\,\mathrm{K\ s}^{-1}$, which is in good agreement with the measured value. These measurements showed that the temperature evolution of a positron plasma can be explained with Newton's law of cooling, even in the strong magnetic mirror field, by taking an average of the magnetic field over the length of the plasma. Additionally, it was the first systematic measurement of positrons cooled evaporatively in an inhomogeneous magnetic field to a temperature of $(41 \pm 4)\,\mathrm{K}$, which was a factor of three lower than previously achieved.

4.5.2 Stacking

As the activity of the source in the upgraded positron system was low, the lifetime in the accumulator was too short to achieve a sufficient number of positrons (of the order of millions or tens of millions) for mixing. To be able to prepare a higher number of particles and perform plasma studies several positron bunches from the accumulator needed to be stacked in the Cusp trap.

Typically 60 stacks were accumulated in, and transferred from, the accumulator as explained above, taking approximately 75 s. The bunches were magnetically guided with no significant losses during transport to the Cusp trap. The positrons were caught in the Cusp trap by pulsing down the US blocking potential of the trap, as shown in Fig. 4.18(a), with an efficiency of $(71 \pm 27)\,\%$. The transfer and catching efficiency was measured by calculating the ratio of charge deposited onto the MUSASHI MCP and of positrons caught in the Cusp trap and immediately dumped onto the Cusp MCP. Ten averages were taken for each value and the 79 % transmission of the mesh at the entrance of the Cusp trap, which particles had to pass twice when caught and extracted, was taken into account. The large uncertainty comes from the low charge amplifier signal of a few mV, which is comparable to the level of the noise on the system.

To decrease the amount of contaminating ions produced by the ionisation of residual gas in the vacuum chambers between the trap during transfer, a RW sweep from 3 MHz to 4.5 MHz was applied to the split electrode, driving out the species with higher mass but keeping the positrons. After the transfer of one bunch of positrons from the accu-

mulator in the Cusp trap the stacking of positrons in the accumulator started again. In parallel the transferred bunch was merged with the positrons which had already been stored in the Cusp trap and moved to the maximum of the magnetic field to minimise the time needed to thermalise due to cyclotron cooling, as shown in Fig. 4.18(b). Afterwards, the particles were compressed and evaporatively cooled in the potential well shown in Fig. 4.18(c). The compression was performed with a RW of frequency 100 kHz and 10 V for about 20 s in the SDR, which will be shown in the subsequent section. The particles were then moved into the storage potential shown in Fig. 4.18(d), in which they were held until the next bunch arrived.

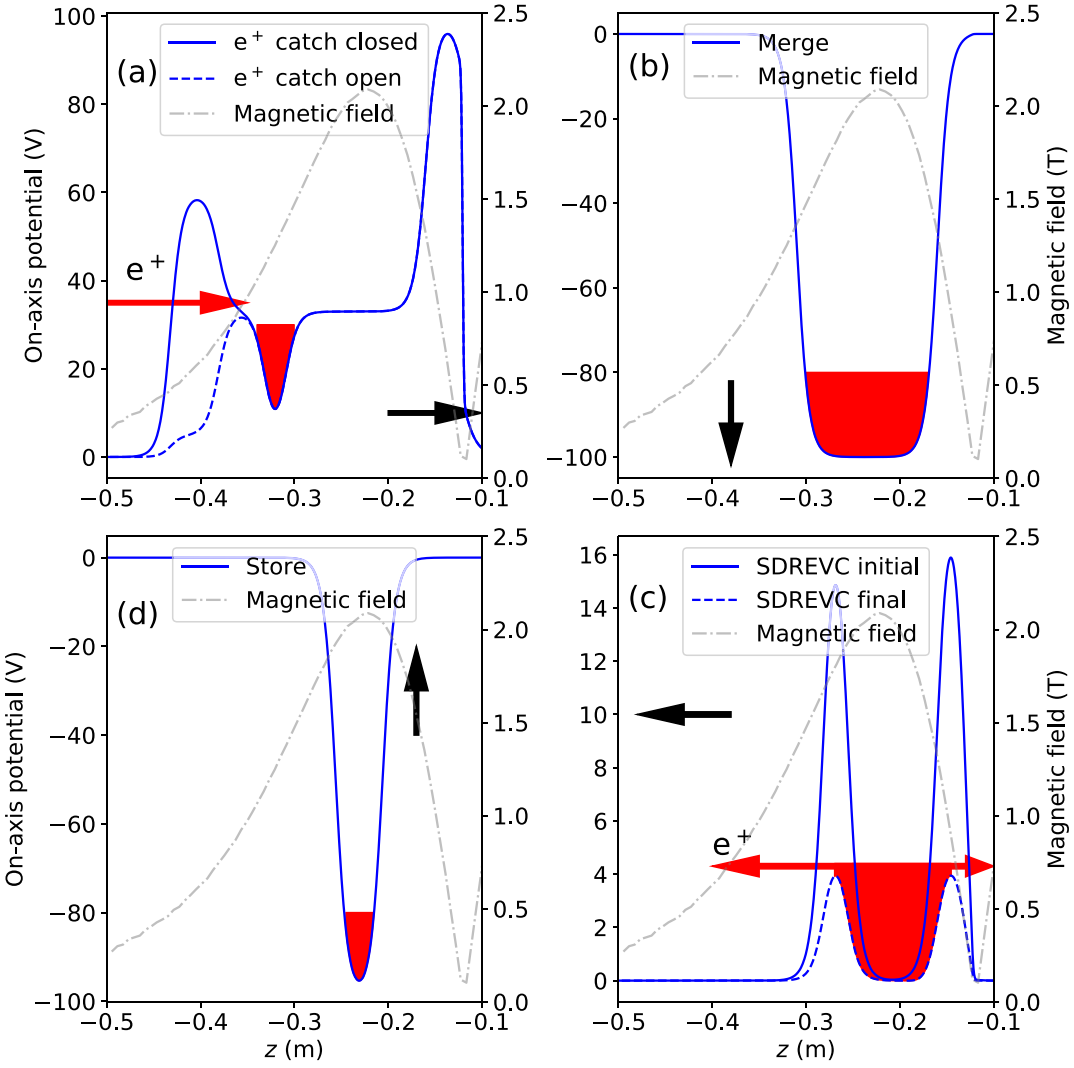

Figure 4.18: Simulated on-axis potential of the catching (a), merging (b), compression and cooling (c), and the storage (d) of positrons. The colored areas indicate the position of the positrons. The red arrows indicate the incoming (a) and evaporating (c) positrons. The magnetic field is shown as the dash-dotted line. The black arrows show the order of the potential manipulations.

Using this scheme, typically eight stacks were prepared in the Cusp trap, yielding

$\sim 4 \cdot 10^6$ positrons with a temperature of $\sim 25\,\mathrm{K}$. After the accumulation was finished, the particles could be held in the Cusp trap for several minutes without losing a significant amount. That was important, because it might take a few minutes for the next antiproton shot to be delivered.

4.5.3 Compression - SDR

A measurement was performed to check if the RW was operating in the SDR. Therefore, the frequency was scanned from 25 kHz to 350 kHz to look for a linear increase in density. To measure the density the positrons were either imaged on the biased MCP/PS US of the Cusp trap to calculate the radius of the plasma as described in Section 4.2.2, or the charge deposited onto the unbiased MCP/PS was acquired with the charge amplifier as described in Section 4.2.1. For the measurement eight stacks of positrons were accumulated in the Cusp trap, yielding on the day of the measurement $(2.88 \pm 0.07) \cdot 10^6$ positrons [2], which were compressed for 20 s in a $\sim 7\,\mathrm{cm}$ long well. Using the number of positrons N, the radius r_p calculated using an average magnetic field of 1.87 T and the length of the well l_p, the density was calculated by

$$n = \frac{N}{r_\mathrm{p}^2 \pi l_p}. \tag{4.10}$$

The plot on the left hand side of Fig. 4.19 shows the measured number density as a function of RW frequency. As one can see, the density increased linearly up to $\sim 200\,\mathrm{kHz}$, after which it started to flatten. The plot on the right hand side of Fig. 4.19 shows the radius and the number of positrons as a function of the frequency f.

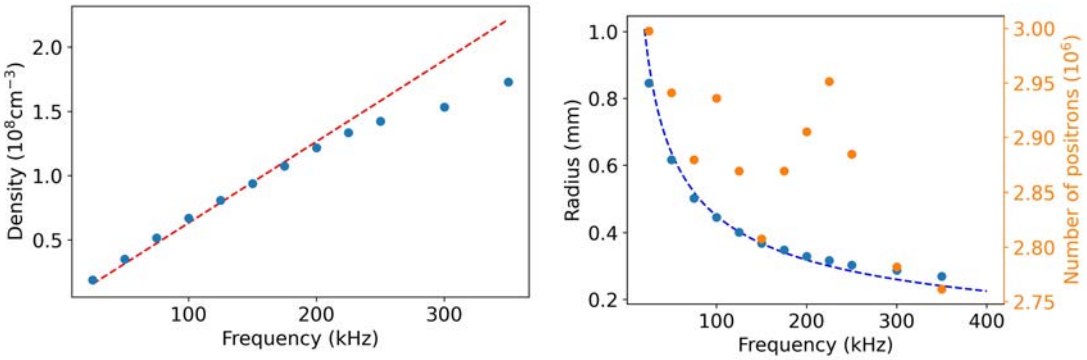

Figure 4.19: Left: Number density of positrons in the Cusp trap as a function of RW frequency (blue dots) and a linear fit using the data points up to 200 kHz (red dashed line) Right: Radius (blue) and number of positrons (orange) as a function of RW frequency. Additionally, the fit of the radius as a function of frequency using the simplified solution to Eq. (4.11) is shown as the dashed line.

The radius of the trapped positrons changes according to [60]

[2] No new moderator was grown on that day, hence the lower initial number of positrons.

$$\frac{\mathrm{d}r_\mathrm{p}}{\mathrm{d}f} = -\frac{r_\mathrm{p}}{2f} \cdot \left(1 + \frac{1}{2\ln\frac{R_\mathrm{W}}{r_\mathrm{p}}}\right), \tag{4.11}$$

where $R_\mathrm{W} = 17\,\mathrm{mm}$ is the electrode radius. Ignoring the logarithmic term which is < 0.1, the differential equation can be solved to be $r_\mathrm{p} = a/\sqrt{f}$, which is in good agreement with the data, as shown in the plot on the right hand side in Fig. 4.19.

Theoretically, for a long cylindrical plasma in a homogeneous magnetic field, the dependence of the plasma density on the RW frequency should be

$$n(f_\mathrm{RW}) = \frac{4\pi\epsilon_0 B}{e \cdot f_\mathrm{RW}}. \tag{4.12}$$

However, the slope of the function did not agree with the calculation when taking the average magnetic field over the length of the well. The measured dependence agreed with a magnetic field of $B_\mathrm{calc} \sim 1.25\,\mathrm{T}$, however, only a small fraction of the positrons were experiencing such a weak field. A similar discrepancy was seen previously with electrons in the same trap [110]. The deviation from the calculated value was connected to the fact that an average of the magnetic field does not reflect the distribution of the particles within in the field and that particles in an equilibrium state of a non-neutral plasma do not follow the magnetic field lines in a strong magnetic mirror field [110]. These effects influence the radius measurement and therefore the density calculation. Nevertheless, it was shown that a linear dependency of the density on the RW frequency could be achieved in the inhomogeneous magnetic field of the Cusp trap, i.e. the positrons were compressed in the SDR.

Chapter 5

Proton source & matter mixing attempts

The proton source, see Section 3.5, was transported to CERN after the initial characterisation and was initially commissioned with a similar setup to that shown in 3.20. Afterwards, it was installed into the experiment and the first accumulation of protons in the Cusp trap was achieved, which will be explained in Section 5.1. The results of the first measurement of cooling protons on positrons and the first attempts to produce hydrogen by mixing electrons and protons will be described in Section 5.2. These measurements showed the possibility to use this setup to mix electrons and protons in future, even though it was not possible to unambiguously measure hydrogen within this work.

5.1 Proton source

At CERN the H_2 generator was exchanged with a Hydrofill Pro (Model: FCH-020, [111]) which was used to fill Hydrostick Pro cartridges (Model: LWH22-10L-5 [112]). This device produced H_2 gas from distilled water with a purity of 99.99 %, and the cartridge was connected to the needle valve of the proton source. After the initial commissioning process the electrodes were spray painted with colloidal graphite to reduce patch potentials. The detector chamber was removed and a differential pumping restriction (ID: 10 mm, length: 60 mm) was added between the source and the connection to the experimental beamline to minimise the hydrogen contamination in the Cusp trap. To transport protons from the source into the trap three additional coils were added, which changed the magnetic field in the source and therefore the motion of the protons. Figure 5.1 shows a sketch of the full setup (top) as well as the changed magnetic field in and around the source due to the additional coils (bottom).

The test setup in Vienna was operating with an extraction rate of 500 Hz. At CERN, such a high rate was not applicable, as the protons had to be caught and moved in the

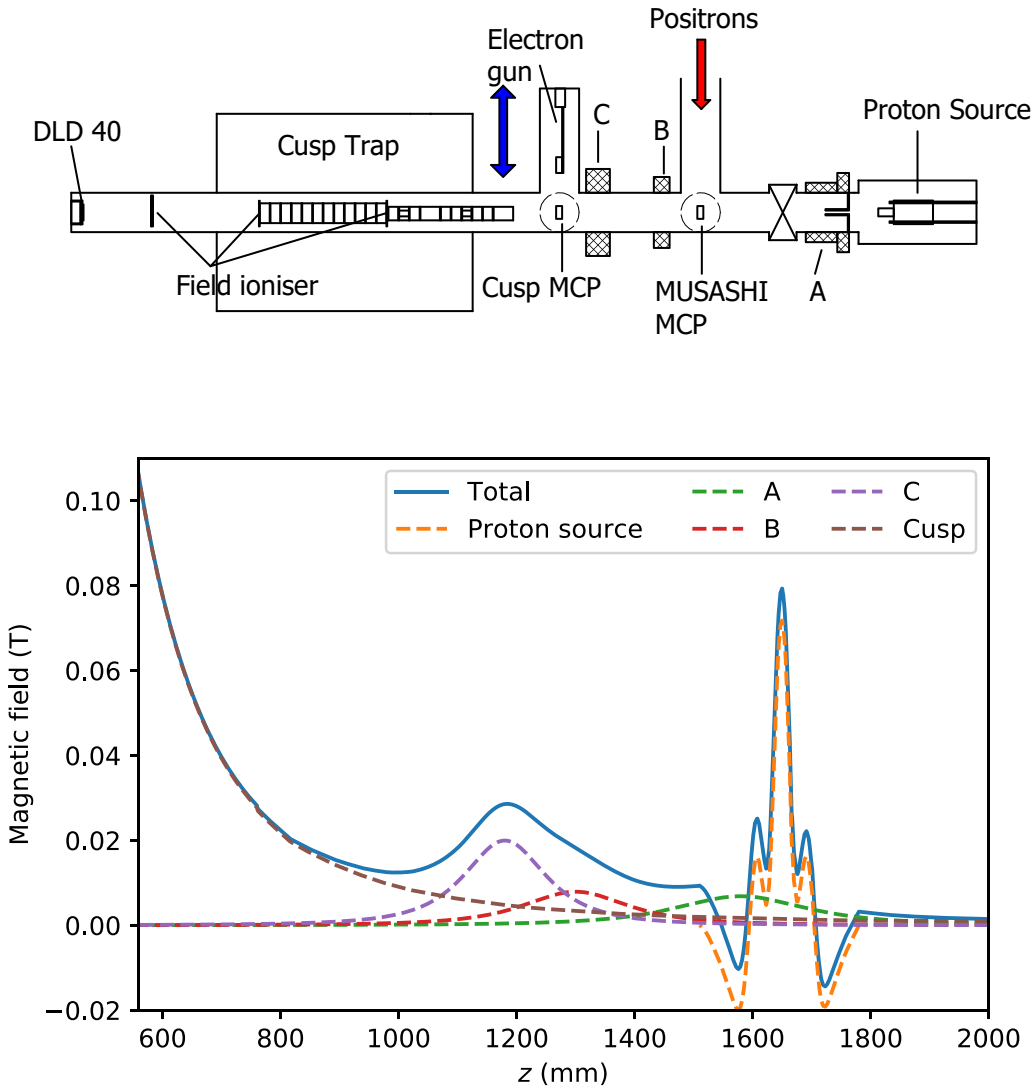

Figure 5.1: Top: Sketch of the proton source installed in the ASACUSA experiment. The magnets are indicated as cross-hatching
Bottom: Total magnetic field in the proton source, which is located at $z = 1650\,mm$, and along the transfer line into the Cusp trap (blue solid line). Additionally, the fields of the proton source, the three transfer line coils and the cusped magnetic field are shown. The fields shown could vary by 10 % due to measurement and simulation errors of the position of the magnets and the magnetic fields.

Cusp trap[1], which took place on the time scale of 100 ms, hence the proton source was operated at an extraction rate of 10 Hz. The electron gun current was increased to 2.1 A. The optimal RW frequency was measured to be 0.46 MHz with an amplitude of 15 V.

The number of protons in the Cusp trap could be measured by extracting the particles onto the Cusp MCP/PS. For a high number of extraction cycles ($\geq$ 200), the

[1] At the time of the first installation of the source Cusp trap II was in place, which had an electrode temperature of $\sim$ 70 K.

charge deposited onto the unbiased MCP could be measured using a charge amplifier as described in Section 4.2.1, the data from which are shown as triangles in Fig. 5.2. To be able to measure small signals for low numbers of repetition cycles the SiPM setup surrounding the imaging camera was used. The MCP/PS was biased and the light acquired by the SiPM was calibrated to the previously measured number of protons with the unbiased MCP at a higher number of extraction cycles. However, it was seen that the number of protons started to saturate for 500 repetitions, yielding $(1.34 \pm 0.51) \cdot 10^6$ protons. Hence, this number was excluded from the calibration. The calibrated stacking curve is shown as circles in Fig. 5.2.

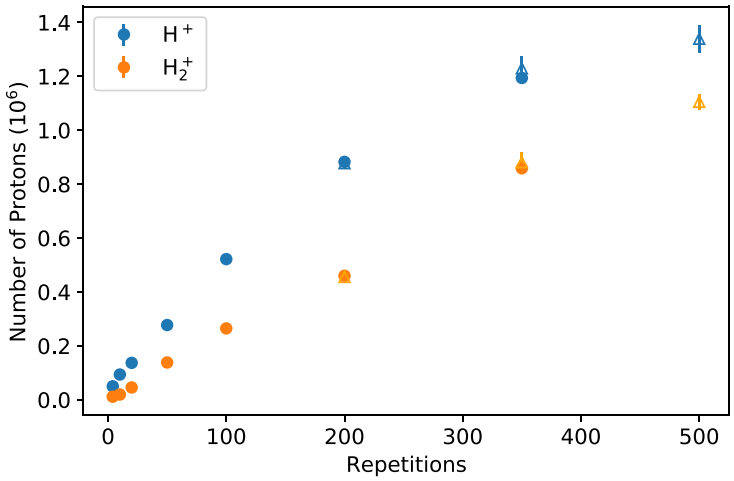

Figure 5.2: Number of protons (blue) and H_2^+ (orange) extracted from the Cusp trap as a function of catching cycles. The triangles show the number of protons measured with the unbiased MCP and a charge amplifier.

Even though it was possible to time the proton source extraction pulse to the Cusp trap catching pulse and filter out heavier ions by the time of flight, H_2^+ was observed in the time-of-flight spectrum when emptying the trap, which was assumed to be produced during the transfer of particles between the trap and the source due to the high temperature of the Cusp trap at that time. Even though no systematic measurements were performed, it should have been possible to remove the H_2^+ from the Cusp trap by applying a rotating wall to confine the protons and drive out the heavier ions, similarly to the operation in the proton source. However, this measurement showed that it was possible to accumulate one million protons within approximately 30 s, confirming the successful integration of the proton source in the experiment.

However, after the installation of the upgraded Cusp trap (i.e. trap III as described in Section 3.3), the stacking of protons did not work anymore without positron cooling in between bunches, which will be described in the subsequent section. In the presented data, the protons cooled on the residual gas in the Cusp trap, which was a consequence of the high temperature of ~ 70 K, in between bunches, which made it possible to stack them. In the upgraded trap, which had an electrode temperature of 6 K, the residual

gas was too low to efficiently cool the protons, hence, an active cooling mechanism was needed not only for mixing but also for stacking protons.

5.2 Proton preparation and mixing attempts

This section describes the measurements and results of the preparation of protons for mixing with electrons to produce hydrogen. After the preparation, mixing studies were undertaken in Cusp trap III. Although experiments seemed promising they had to be stopped abruptly because the antiproton run started soon after.

5.2.1 Electrons

For the production of hydrogen, electrons are required. As shown in the top sketch of Fig. 5.1 an electron gun is installed near the entrance of the Cusp trap, which could be inserted into the beamline. The trap was filled with electrons and compressed with a RW with a frequency of 100 kHz and an amplitude of 8 V. The potential well was simultaneously decreased to a final depth of 3.5 V, yielding a temperature in the order of 30 K. The electrons were then stored in the downstream side of the trap before catching the positrons, which were needed to cool the protons.

5.2.2 Proton cooling

In order to catch protons and produce hydrogen, the protons need to be cooled with positrons, similar to the cooling of antiprotons with electrons, and as described in Chapter 2.2.2. Therefore, $\sim 8 \cdot 10^5$ positrons were caught in the Cusp trap after electron loading, using the potential shown on the left hand side of Fig. 5.3. Subsequently, the positrons were moved to a shallow well for compression by applying a RW with a frequency of 100 kHz and 8 V amplitude. After 10 s of compression the potentials were changed to the proton catching potential, which is shown on the right hand side Fig. 5.3.

The cooling of protons was measured indirectly by looking at the pick-off voltage of the biased MCP after 100 bunches of protons were extracted from the proton source and accumulated in the Cusp trap with a variable waiting time in between each of the extraction cycles, as shown in Fig. 5.4.

Increasing the cooling time between stacks lead to an increase of the MCP signal, i.e. more protons cooled into the bottom of the well and could be stored while the trap was opened for the next bunch rather than escape out of the opened well. The data were fitted with an exponential rise to maximum function

$$N(t) = A(1 - e^{-\frac{t}{\tau}+c}), \tag{5.1}$$

where τ is the characteristic time in seconds, A is the maximum signal and c is an offset from $t = 0$. The result showed a characteristic time of (0.8 ± 0.1) s for $\sim 8 \cdot 10^5$ positrons. The measurement was repeated with a reduced number of $\sim 3.5 \cdot 10^5$

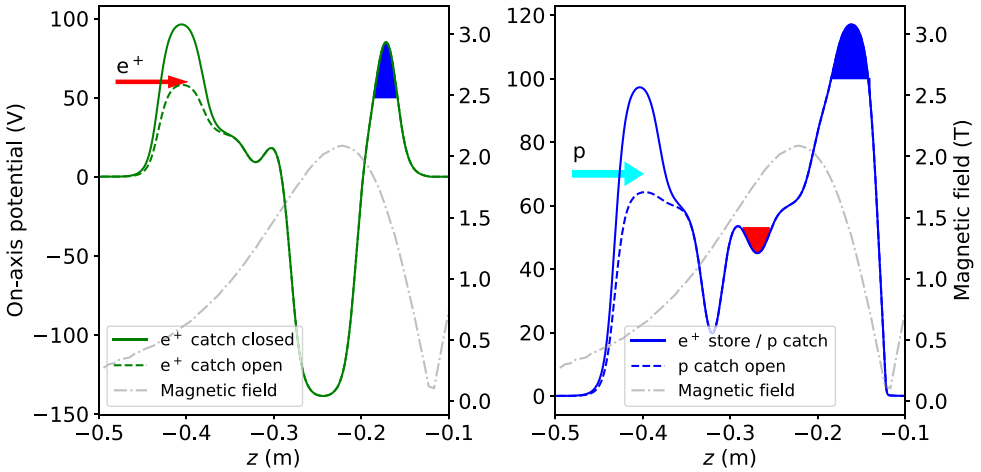

Figure 5.3: On-axis magnetic field and potentials for catching of positrons (left) and protons (right). The colors indicate the stored electrons (blue), the positrons (red) and the protons (cyan).

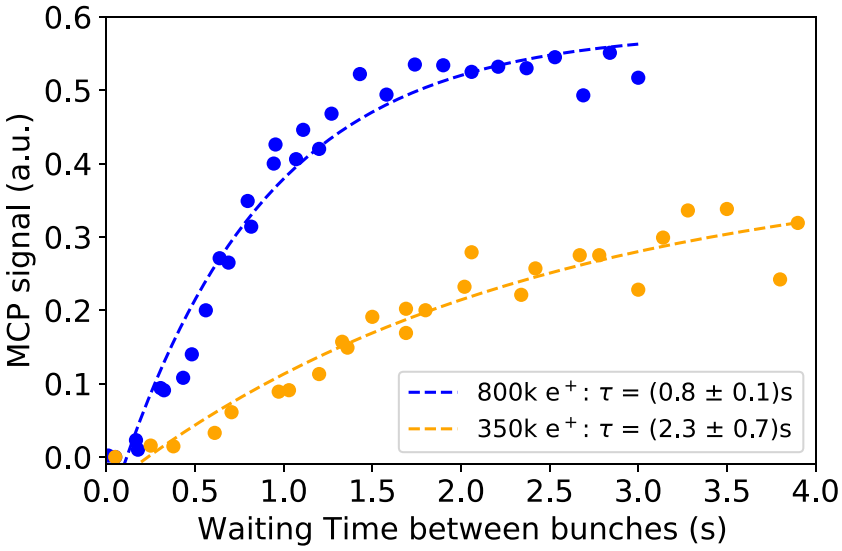

Figure 5.4: Signal of protons extracted as a function of waiting time between bunches extracted from the proton source for ≈ 800 k (blue) and ≈ 350 k (orange) positrons. The data were fitted using an exponential rise to max function (see text).

positrons, which resulted in a much slower cooling time of the protons of (2.3 ± 0.7) s. With this scheme it was possible to accumulate $(4.3 \pm 0.2) \cdot 10^5$ protons in 100 repetitions, each cooling the protons for 1 s, which is comparable to the number of antiprotons used for antihydrogen production.

5.2.3 Mixing attempts

Unambiguously demonstrating the formation of hydrogen was not possible because of the limited time available to operate the proton source before it was necessary to remove

it to install MUSASHI. However, a few experiments were performed to test the mixing procedure which would later be used for antihydrogen, and to measure the temperature of the protons and electrons after mixing. The procedure was:

- Load, SDREVC and store electrons
- Catch, compress and store positrons
- Stack, compress and cool protons
- Kick out positrons and perform mixing of electrons and protons

After stacking of the protons was completed, the protons and positrons could be compressed in the same well, shown on the left hand side of Fig. 5.5, by applying a RW with a frequency of 200 kHz and an amplitude of 8 V. To cool the protons using the positrons the RW was turned off after 10 s to stop the heating due to the RW, and the particles were held in the potential shown in the central plot of Fig. 5.5. Subsequently, the positrons were kicked out by applying a 50 V amplitude and 10 ns long pulse, as shown on the right hand side of Fig. 5.5. The short pulse ensures that the protons cannot leave the trapping well in the given time due to their larger mass and consequently the longer time-of-flight. The protons and electrons were afterwards moved into the mixing potential, as shown in Fig. 5.6, where the bottom of the electron trapping well was decreased within 480 ms to produce an overlap of the protons and electrons.

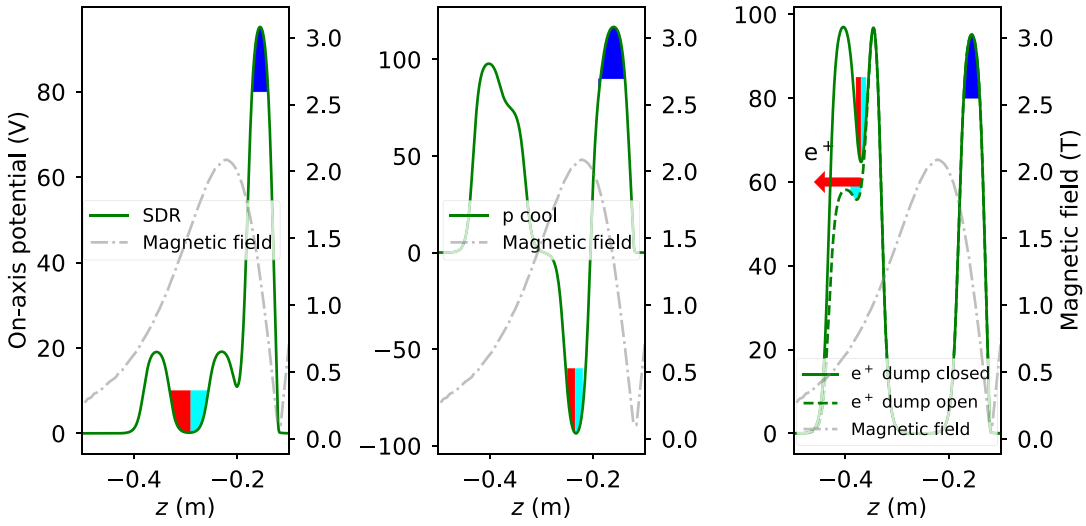

Figure 5.5: On-axis potentials for compressing the protons and positrons (left), cooling of the protons (center), and the kick out of positrons (right). The two coloured regions indicate that positrons and protons are present in this well.

The temperature of the protons (in the US well) and the electrons were measured by slowly releasing the particles out of the well, as described in Chapter 4.3. Additionally, the DS well was emptied by a fast dump to see the SiPM signal of the protons which relaxed to the deeper DS well. The number was not measured directly as the MCP/PS

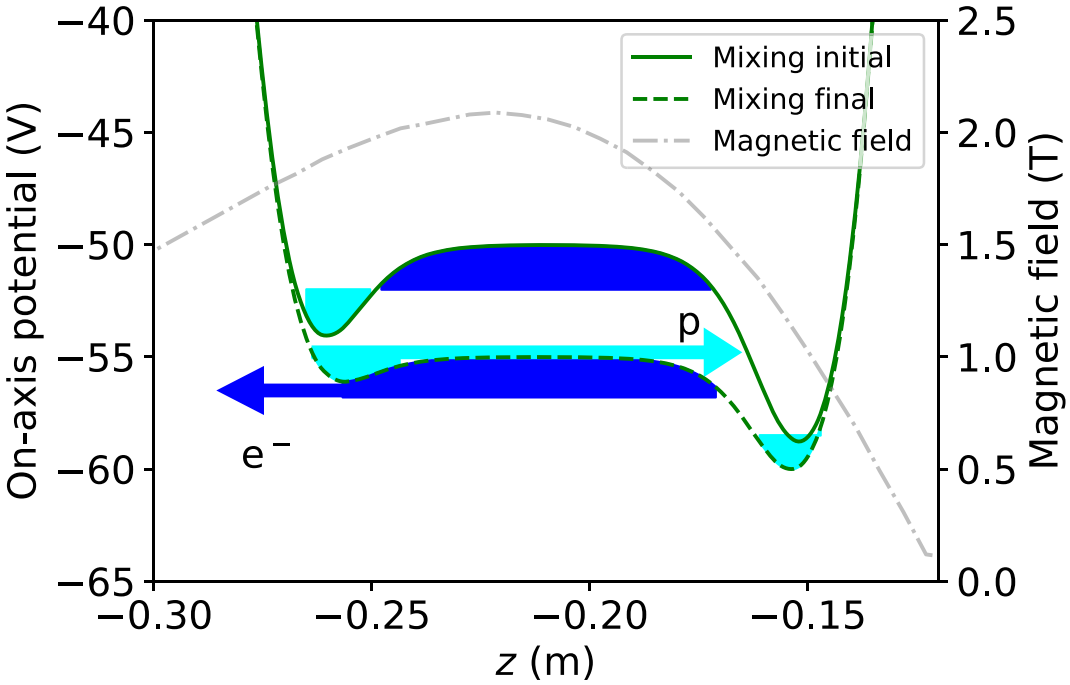

Figure 5.6: Initial and final mixing potentials.

needed to be biased for the temperature diagnostics and couldn't be turned off fast enough. The potentials of the individual dumps are shown in Fig. 5.7. The number of positrons kept in the proton well to cool the protons during mixing, was changed as well. These could relax into the DS well and can be seen in the DS dump. There were few data points taken, due to limited time, hence no reasonable conclusion could be made whether or not hydrogen was produced. The results of the measurements are shown in Table 5.1.

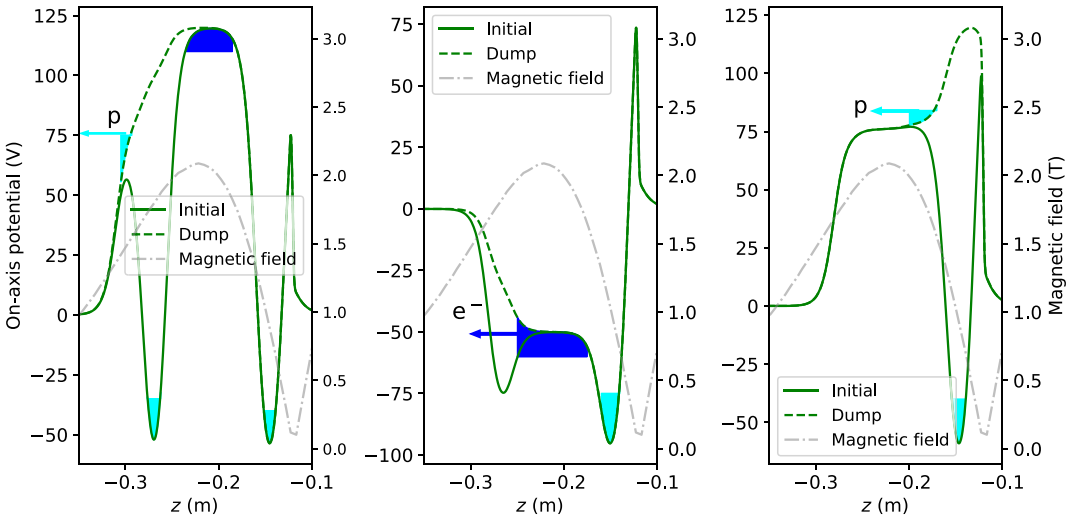

Figure 5.7: Initial (solid lines) and final (dashed lines) potentials for dumping of the protons (cyan) in the US (left) and DS (right) well and the electrons (blue, center).

Table 5.1: Temperature of the US protons and electrons and the integrated SiPM signal of the positrons for different preparation methods.

Property	Hot e^-	Cold e^-	Cold e^- & keep $\sim 5 \cdot 10^4$ e^+	Cold e^- & keep $\sim 4 \cdot 10^5$ e^+
T_{e^-} (K)	2430 ± 110	24 ± 6	21 ± 5	18 ± 3
T_p US (K)	14120 ± 1150	6120 ± 440	7990 ± 570	550 ± 40
e^+ signal (a.u.)	410 ± 20	690 ± 70	2210 ± 220	16850 ± 1200

The results of the measurements can be summarised as follows. Column two in the table shows the test when the electrons were heated during mixing by applying white noise to the split electrode [113] to a temperature of (2430 ± 110) K and kicking out all positrons with a 50 V pulse. This lead to a high temperature of the protons in the US well on the order of (14120 ± 1150) K, because no positrons were left for cooling. Decreasing the temperature of the electrons halved the temperature of the protons to roughly (6120 ± 440) K, indicating that the protons were heated by the white noise as well as the electrons. The effect of keeping positrons in the well during mixing on the temperature of the protons can be seen in columns four and five. Reducing the voltage in the fast pulse to dump the positrons to 40 V, for which $\sim 5 \cdot 10^4$ positrons remained in the well, the temperature of the protons was the same. However, keeping $\sim 4 \cdot 10^5$ positrons, corresponding to a pulse amplitude of 35 V, decreased the proton temperature to (550 ± 40) K.

These few data could not be used to verify the mixing scheme as a method of making hydrogen. However, it was seen that it was possible to cool protons to a lower temperature with a higher number of positrons in the well. Hence, these few tests together with the ability of stacking protons showed the first measurement of cooling protons on positrons to reach low temperature on the order of a few hundred Kelvin.

Additionally, these measurements tested the full mixing cycle with charged particles. It showed that it is possible to measure the temperature of the residual particles remaining in different wells after mixing. The investigations showed the principle working of the proton source in the experiment and will be useful in future to produce hydrogen in times when no antiprotons are delivered by CERN, hence they provide a crucial tool in the development of future measurements.

Chapter 6

Antihydrogen

During the antiproton run the production of antihydrogen was performed with the plasma control described in Chapter 4. The preparation of antiprotons and positrons was optimised to achieve reproducible initial temperature, number and density of the plasmas. The timing sequence for preparing the particles and the mixing cycle is shown in Fig. 6.1. The preparation of the positrons and antiprotons in the Cusp trap will be described in detail in Section 6.1, and the description of the mixing cycle in Section 6.2. In Section 6.3 the results of the measurements of the plasma temperature, space charge and radial profile at different times during the mixing sequence will be presented, followed

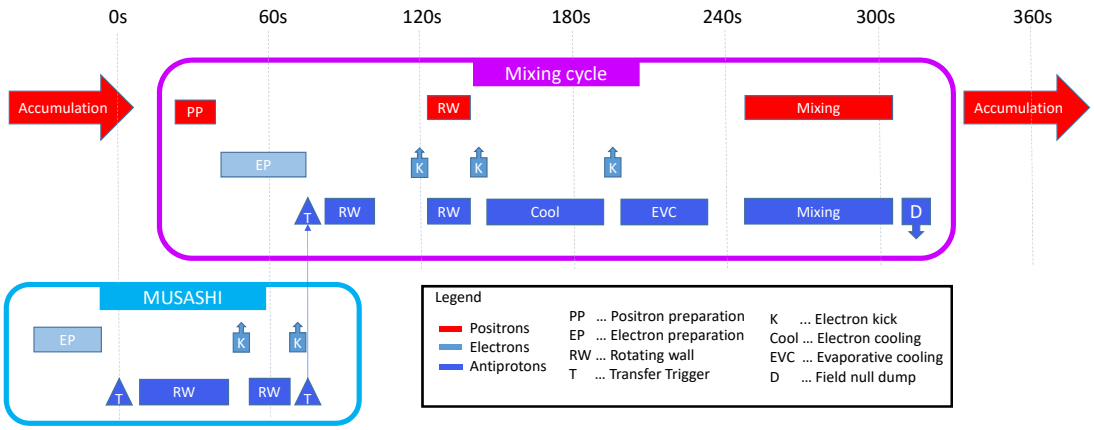

Figure 6.1: Sequence of the parallel preparation of positrons and antiprotons and the 60 s mixing cycle relative to the antiproton injection into MUSASHI at 0 s. Positrons are stacked for 12 minutes in the Cusp trap, which is not shown in this schematic.

6.1 Positron and antiproton preparation

The temperatures, number of particles, radii, number densities and space charges of the positron and antiproton plasmas before the mixing sequence is started are listed in Table 6.1.

Table 6.1: Initial plasma properties of the antiprotons and positrons before mixing.

Property	Positron	Antiproton
Temperature (K)	24 ± 4	96 ± 30
Number of particles (10^6)	~ 4.0	~ 0.5
Radius (mm)	0.40 ± 0.01	0.57 ± 0.04
Density (cm^{-3})	$\sim 1.6 \cdot 10^8$	$\sim 2.0 \cdot 10^7$
Space charge (V)	2.0 ± 0.1	0.4 ± 0.1

6.1.1 Positron preparation in the Cusp trap

Due to the low activity of the ^{22}Na source several fill cycles of the accumulator had to be stacked in the Cusp trap, as discussed in Chapter 4. Typically, eight stacks, each accumulating 60 shots from the BGT, were necessary to trap $\sim 4 \cdot 10^6$ positrons. The stacking and preparation of positrons took about 12 minutes.

After stacking, the positrons were held in the DS part of the trap and the antiprotons were transferred into the Cusp trap and prepared. Before the mixing started, the positrons stored were compressed using a RW with a frequency of 200 kHz and an amplitude of 10 V to a density of $\sim 1.6 \cdot 10^8\,\mathrm{cm}^{-3}$. Positrons cooled via cyclotron cooling to (24 ± 4) K in the average 1.87 T magnetic field over the length of the plasma.

6.1.2 Antiproton preparation

At the end of the positron preparation, the antiproton cycle was started, as described in Chapter 3.2.3. In parallel to the antiproton preparation cycle in MUSASHI, electrons were prepared in the Cusp trap to cool the incoming antiprotons. First, the trap was filled with electrons which were prepared by the SDREVC technique using a RW with a frequency of 30 kHz and an amplitude of 2 V. After the antiproton transfer and the cooling on the electrons, the latter were removed by several extraction pulses (labeled as electron kick in Fig. 6.1) interrupted by compression and cooling stages. The antiprotons were finally evaporatively cooled for 20 s to a space charge of (0.4 ± 0.1) V. Approximately $5 \cdot 10^5$ antiprotons were kept in the potential well for mixing, yielding a density of $\sim 2 \cdot 10^7\,\mathrm{cm}^{-3}$ with a temperature of (96 ± 30) K.

6.2 Antihydrogen Formation

The production of antihydrogen was performed by slowly merging the trapping potentials of the antiprotons (held in the well at $z \sim -0.27$ m) and positrons (at $z \sim -0.23$ m), as shown in Fig. 6.2. This technique was pioneered by the ATRAP collaboration [114] and improved by the ALPHA collaboration [115], both at CERN.

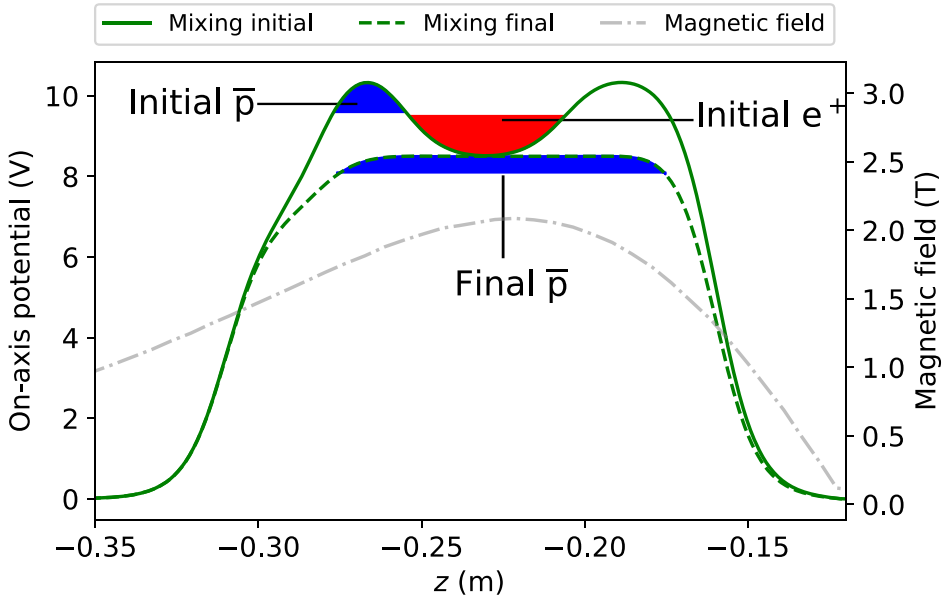

Figure 6.2: Initial and final on-axis potential during mixing. The confinement potential is ramped down slowly within 60 s. The colored areas indicate the position of the antiprotons (blue) and positrons (red) to guide the eye of the reader.

Several experiments were performed to investigate the mixing procedure and will be described in this chapter. The CSS was used to estimate the number of antihydrogen atoms produced. The annihilation signals during mixing were cumulatively acquired in 2- and 3-coincidence mode (i.e. a signal must be measured on two or three of the scintillators to count as an event, as described in Chapter 3.3.2), which are shown in Fig. 6.3 as the blue and orange solid lines, respectively. The increase in the number of the counts from the background was estimated by a linear fit on the data points before the mixing sequence had started, i.e. the data points at $t < 0\,\text{s}$ in the figure, which was subtracted from all data points for each acquisition mode separately. The number of antihydrogen atoms produced ($N_{\text{mix},i}$, with the counting error $\sqrt{N_{\text{mix},i}}$, where $i = 2, 3$ indicates the 2- and 3-coincidence mode, respectively) was taken as the cumulative counts at the time the mixing sequence had finished, indicated as the black dash-dotted line in Fig. 6.3. The remaining antiprotons were slowly (within 5 s) pushed out of the well towards the magnetic field null, where the particles followed the diverging field lines and annihilated on the electrode walls, after the mixing sequence was finished. The number of antiprotons ($N_{\text{dump},i}$) was taken as the cumulative counts after the dump had finished and the curve flattened again, indicated as the green dash-dotted line in the figure. The relative antihydrogen yield $Y^{\overline{\text{H}}}$ was calculated as the ratio of the annihilation signal during mixing and from the remaining antiprotons in the dump as

$$Y^{\overline{\text{H}}} = \frac{N_{\text{mix},i}}{N_{\text{dump},i}}, \tag{6.1}$$

where $i = 2, 3$ indicates the 2-coincidence and the 3-coincidence measurements. By multiplying this relative yield by the measured number of initial antiprotons, the number of antihydrogen atoms produced could be estimated.

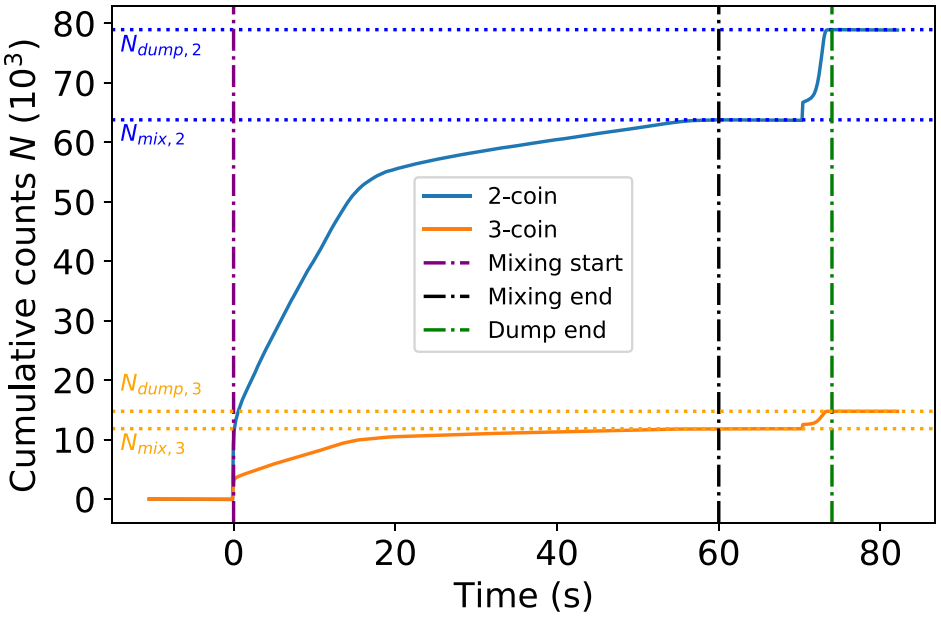

Figure 6.3: Background subtracted cumulative annihilation counts of the CSS during a 60 s mixing sequence and the subsequent antiproton dump. The data were acquired in 2-coincidence (blue solid line) and 3-coincidence (orange solid line) mode. The vertical dash-dotted lines indicate the time of the start of the mixing cycle (purple), the end of the mixing cycle (black) and the end of the antiproton dump (green). The vertical dotted lines show the cumulative counts after the merging (N_{mix}) and after the dump (N_{dump}). See text for further information.

A Simulation was performed in order to estimate the acceptance of the CSS along the Cusp trap [116]. In the simulation, which was performed in FLUKA [117], 10^4 antiprotons were initially generated at points along the trap axis with a thermal distribution ΔE and expanded isotropically annihilating on trap electrodes. The result of the acceptance, which was taken as the ratio of the detected antiproton signals to the initial number of antiprotons, normalised to the maximum as a function of the annihilation position is shown in Fig. 6.4. Additionally, the center of the mixing region (green dashed line) and the magnetic field null (red dashed line) are indicated. The acceptance of the detector is flat over a range of about 10 cm from the magnetic field null before it starts to decrease.

The two acquisition modes suffer from different systematic effects. For example, the 2-coincidence is sensitive to positrons annihilating on the electrode walls producing two gamma rays (with an estimated efficiency of $< 1\,\%$ due to the thin scintillator sheets), and cosmic ray background which can be detected on two opposing scintillators. The 3-coincidence method is not sensitive to either of these two, hence it has a lower background count rate. However, the number of events is much lower, as it needs three scintillators detecting a particle simultaneously. Additionally, as can be seen

from the simulation in Fig. 6.4, the acceptance starts to decrease closer to the field null. Nevertheless, the 2-coincidence and the 3-coincidence event decisions have both approximately equal acceptances at the magnetic field null and the mixing region. The subsequent sections present the results for both of the coincidence yields separately.

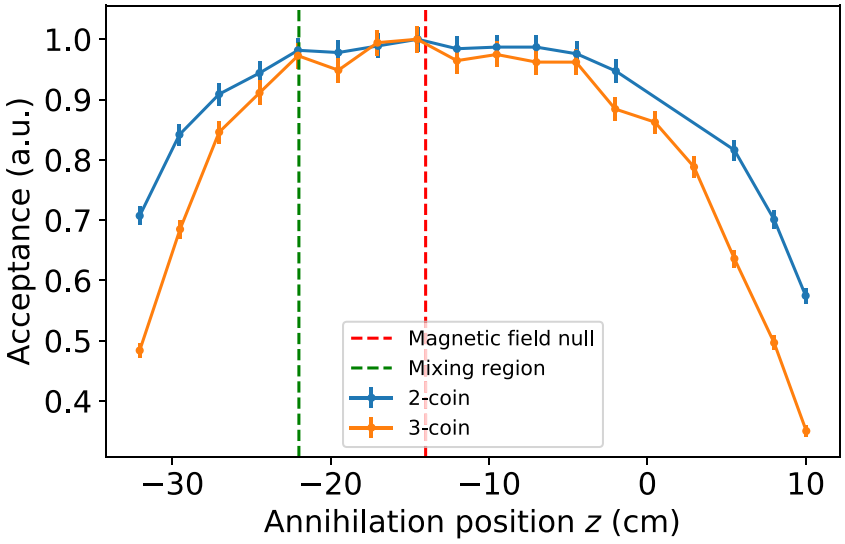

Figure 6.4: Simulated acceptance normalised to the maximum of the CSS in 2-coincidence (blue) and 3-coincidence (orange) mode for anitproton annihilation at various positions along the Cusp trap. The green dashed line indicates the position of the mixing, the red dashed line is the position of the magnetic field null.

The antihydrogen formation process was studied by stopping the mixing sequence after a variable time and measuring the temperature (as explained in Chapter 4.3), radius (as explained in Chapter 4.2) or residual number of particles in the well, all measured on the Cusp MCP/PS.

6.3 Time dependence

The production of antihydrogen was performed by slowly merging the two species as described above. It was possible to study the formation as a function of a total mixing time τ in a range of 100 ms up to 60 s. After the mixing sequence had finished, the residual antiprotons were moved to the magnetic field null and the antihydrogen yield $Y^{\overline{\mathrm{H}}}$ was calculated as described above. The top plot of Fig. 6.5 shows the resulting ratio as a function of mixing time for the 2- (blue) and 3- (orange) fold coincidences. The data were taken with slightly different preparation schemes, represented by the open and solid data points. For the open circles (and in the course of this subsection), the antiprotons were evaporatively cooled within 20 s as described above, leaving more particles in the trap. On the second day, i.e. the solid points, the cooling was performed within 40 s and to a slightly shallower well, leaving less antiprotons in the well, hence less cumulative counts during mixing and in the dump, which resulted in the larger uncertainties in the

3-coincidence measurements. This mixing preparation was used in the data presented in subsequent section. However, it can be seen that up to $\sim 80\,\%$ of the antiprotons could be converted into antihydrogen, yielding up to $\sim 4 \cdot 10^5$ antiatoms. Additionally, by performing the potential manipulation slower, i.e. having a longer mixing time τ, more antihydrogen was produced.

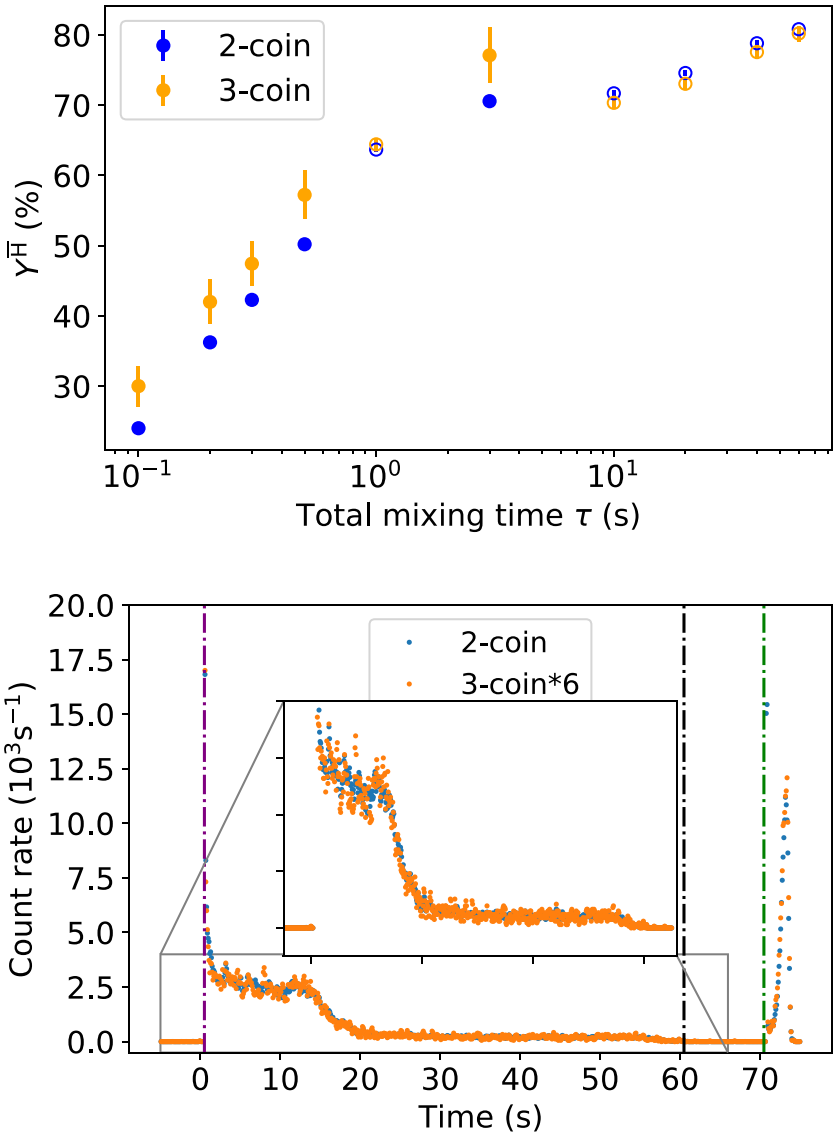

Figure 6.5: Top: Relative antihydrogen yield $Y^{\overline{H}}$, as defined in Eq. (6.1), as a function of total mixing time τ for events acquired in 2-coincidence (blue) and 3-coincidence (orange) mode. The open data points indicate measurements with a higher number of initial antiprotons compared to the solid points. See text for further information.
Bottom: Count rate over a mixing time of 60 s and the subsequent dump of antiprotons. The data points for "3-coin" are scaled by a factor of 6 for comparison. The y-axis in the plot is limited to $20 \cdot 10^3\ s^{-1}$ for visibility. The vertical lines indicate the times of the start of the mixing (purple), the end of mixing (black) and the beginning of the magnetic field null dump (green).

The bottom plot of Fig. 6.5 shows the count rate during 60 s of mixing, calculated

as the derivative of the cumulative sum of events recorded. The sample time was 0.1 s. The vertical lines indicate the start of the mixing (purple), the end of the mixing (black) and the start of the dump (green). The blue and orange data points represent the measurement using the 2- and the 3-coincidence, respectively. A high and a low antihydrogen production rate plateau were visible. The high rate region was consistently up to 1/3 of the total mixing time τ when $\tau > 1$ s. That implied that the transition between the two regions occurred at a fixed fraction of the mixing cycle. In order to understand this transition in the production rate, the mixing time was fixed to be $\tau = 60$ s. The mixing cycle was interrupted at variable times and the temperature, radius and space charge of the positrons and the antiprotons were measured.

To acquire the radius of the species as described in Section 4.2.2, the particles had to be extracted upstream to the MCP-PS. First, the antiprotons were extracted and the positrons 10 s later. Figure 6.6 shows the results for positrons (blue) and antiprotons (orange) for a $\tau = 60$ s mixing sequence interrupted at variable times. In the case of positrons, the radius was constant up to approximately 1/3 of the mixing cycle after which the expansion rate increased. For antiprotons the plasma expanded rapidly between 5 s and 10 s, and the antiproton cloud covered the MCP completely after 10 s preventing further measurements being made. This fast increase in radius can be explained by the conservation of the canonical angular momentum. In a sufficiently strong magnetic field $\sum r_j^2 \approx NR^2$, where r_j is the radial position of the j^{th} particle and R is the radius of the plasma [118]. As a consequence, the radius of the antiprotons has to increase for each antiproton escaping due to the formation of antihydrogen. In the first 20 s most of the antiprotons were converted into antihydrogen atoms, hence the fast expansion of the antiprotons in this region.

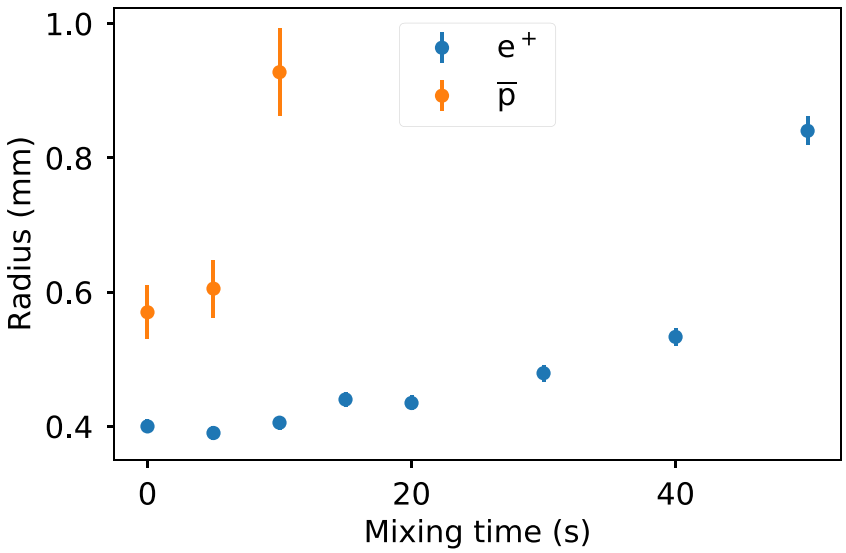

Figure 6.6: Positron (blue) and antiproton (orange) radius in the Cusp trap as a function of mixing time.

A similar behaviour was observed for the temperature, where the positrons remained at the initial temperature of $(24 \pm 4)\,\mathrm{K}$ over the full mixing cycle, which was a consequence of the strong magnetic field with an average of $\sim 1.87\,\mathrm{T}$ in the mixing region and therefore a fast cyclotron cooling rate of the positrons. The antiprotons started heating up after $\sim 10\,\mathrm{s}$, as shown in the top plot of Fig. 6.7. From the temperature analysis it was possible to extract the space charge ϕ of the positrons and the antiprotons as the on-axis potential at which the particles start to leave the trap. The result is shown in the bottom plot of Fig. 6.7. The space charge of the positrons was decreasing linearly over the measured time range, which was expected as the blocking potential was lowered linearly. The uncertainty of the space charge of the antiprotons is too large to make a conclusion about the evolution, however, from the antihydrogen signal during mixing, a strong decrease within the first 20 s would have been expected.

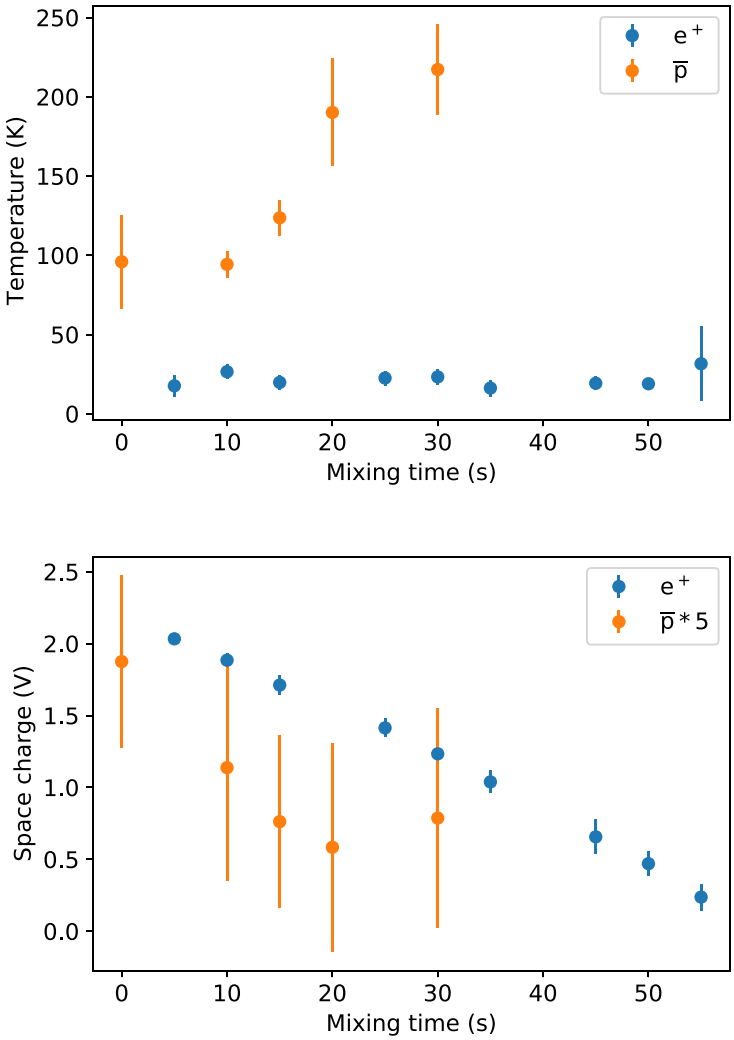

Figure 6.7: Temperature (top) and space charge (bottom) of the positrons (blue) and antiprotons (orange) as a function of mixing time. The space charge of the antiprotons was multiplied by five for visibility.

6.4 Temperature dependence

As described in Chapter 2.3.1 the antihydrogen production rate via three-body recombination is theoretically proportional to the positron temperature with $T^{-9/2}$. However, simulations have shown [68] that the exponent observed is not constant for ground-state antihydrogen but variable, depending on the positron plasma temperature and density due to collisions of the atoms with the positron plasma which can lead to collisional de-excitation of the atoms. In order to study the temperature dependence of the formation process white noise was applied to the downstream split electrode during mixing to heat up the positrons [113]. This measurement was performed (i) without and (ii) with positrons, and (iii) interrupting the mixing sequence after 10 s to measure the positron temperature. As antiprotons were stored in the US side of the trap, they did not interact with the RW until they were able to reach the DS well, i.e. when the potential barrier was small enough for the antiprotons to overcome. The measurement of the positron temperature, following the description in Section 4.3.2, yielded a linear dependence on the power P - presented as the input power into the electrode [1] - with a slope of $(6.6 \pm 0.3) \cdot 10^4\,\mathrm{K/W}$ and an offset of $(28 \pm 4)\,\mathrm{K}$ as shown in Fig. 6.8.

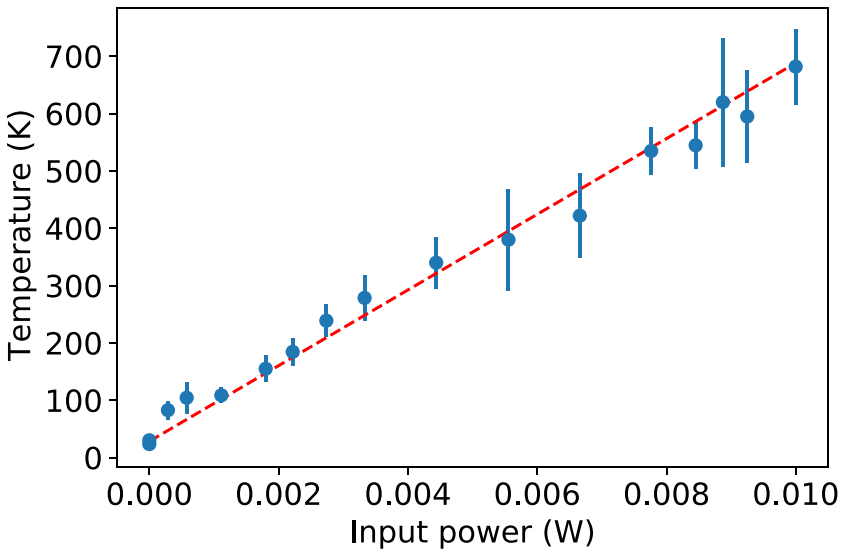

Figure 6.8: Positron temperature as a function of noise power. The red dashed line shows the linear fit.

Figure 6.9 shows $Y^{\overline{\mathrm{H}}}$, as defined in Eq. (6.1), without (top plot) and with (bottom plot) positrons. For the first case, the quantity $Y^{\overline{\mathrm{H}}}$ does not reflect any antihydrogen production, however, it shows the loss of antiprotons during the mixing sequence as a function of heating power. For the second case the power was mapped to the positron temperature using the result of the fit shown in Fig. 6.8.

[1] The amplitude of the noise was scanned. The total impedance into the electrodes, hence the actual power injected, is unknown.

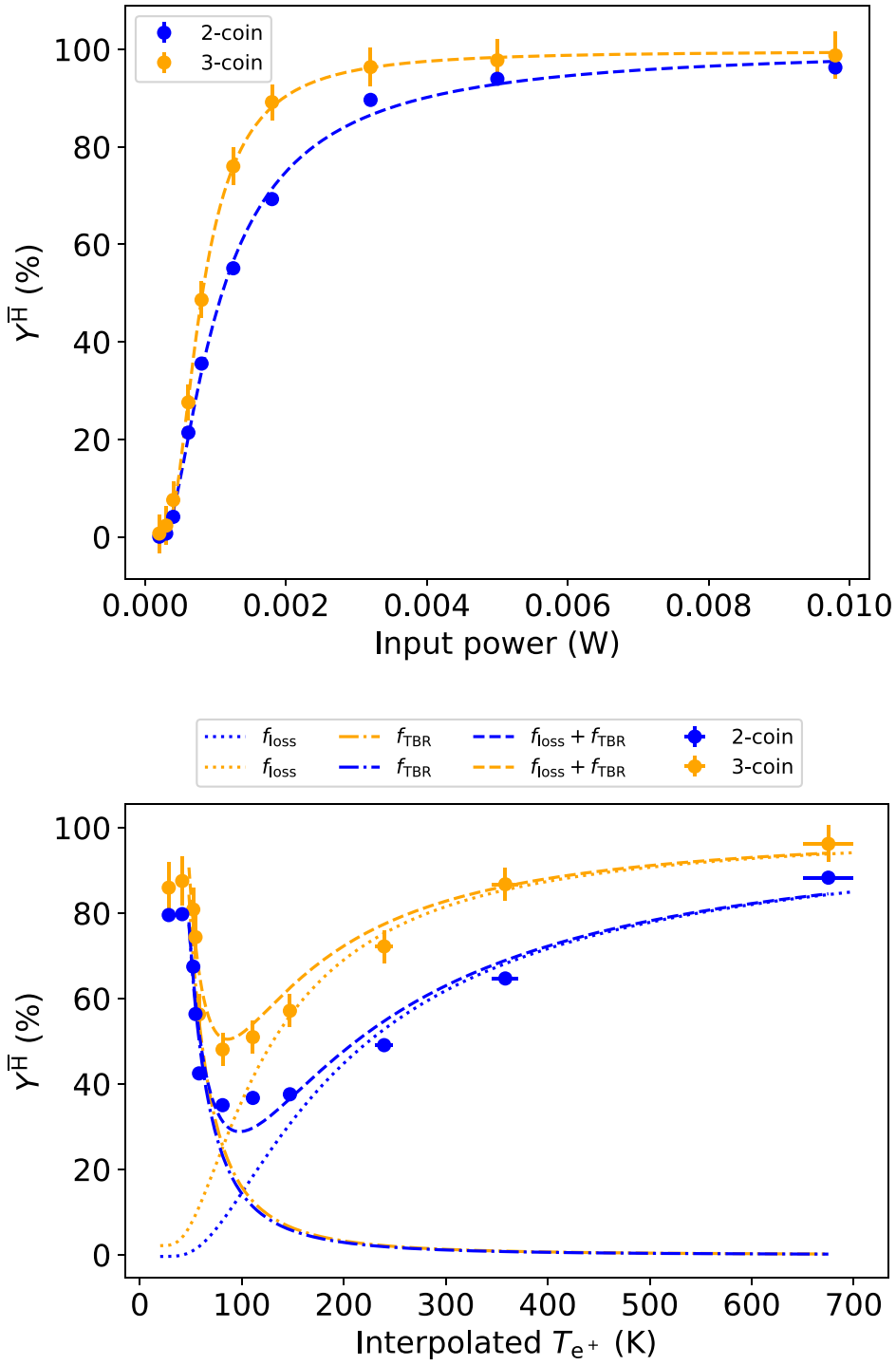

Figure 6.9: Top: $Y^{\overline{H}}$ for a 60 s mixing sequence acquired in 2-coincidence (blue) and 3-coincidence (orange) mode as a function of noise power without positrons. The dashed lines are the corresponding fits using Eq. (6.4).
Bottom: $Y^{\overline{H}}$ as a function of positron temperature. The dotted lines are the fits using Eq. (6.7)*, the dash-dotted lines are the fits using Eq.* (6.8) *and the dashed lines are the combined fits using Eq.* (6.9)*. See text for further information.*

The antihydrogen yield was flat for low heating powers, i.e. low positron temperatures, and dropped fast in the range above 50 K. Additionally, it can be seen that at higher heating powers the annihilation signal increased again, independent of whether or not positrons were present in the trap. This increase in signal was caused by antiprotons being heated enough by the noise to be able to escape the trapping well DS and annihilated on the trap walls following the magnetic field lines at the field null. This signal occurred on the CSS >30 s after the mixing started and showed an exponential increase in time rather than the plateau structure described above for antihydrogen production. An example of the count rate is shown in Fig. 6.10 for the cases without (top) and with (bottom) positrons present in the trap for the minimum (left) and maximum (right) heating power tested.

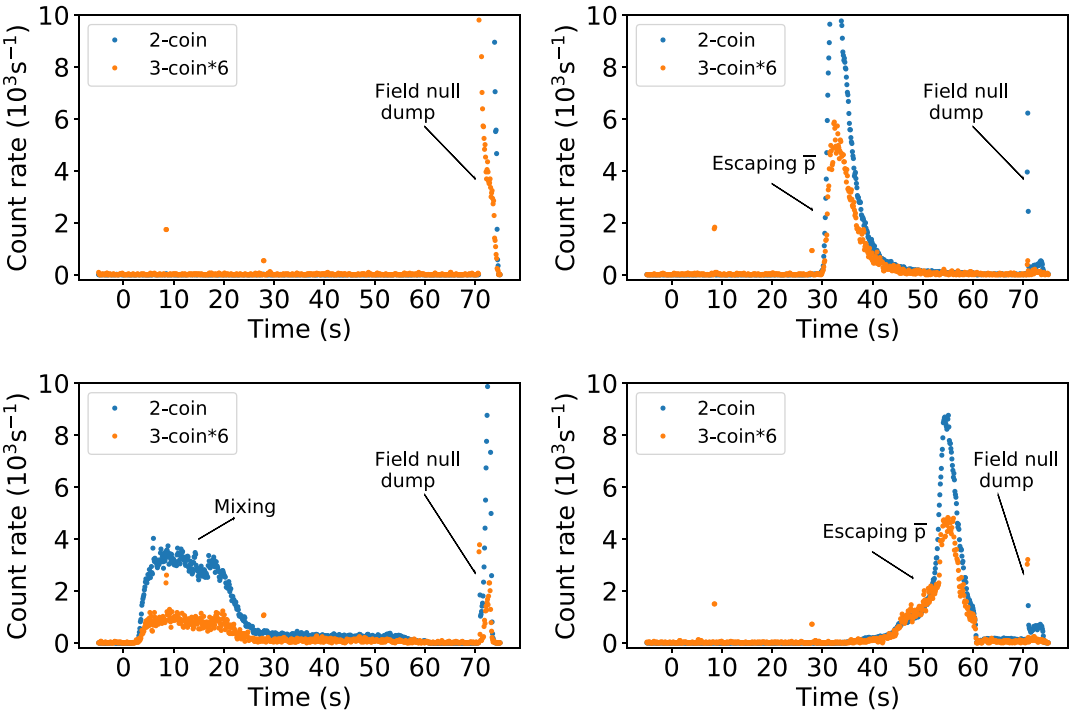

Figure 6.10: Count rate as a function of mixing time with antiprotons only (top) and antiprotons and positrons (bottom), and application of a noise input power with amplitude of 0 W (left) and 0.01 W (right). The y-axis of the plots was limited to $10^4\ s^{-1}$ for visibility.

Antiprotons could escape the potential well if their energy was larger than the trapping well depth. The minimum energy to escape the well E_{esc} is a function of time due to the change in the mixing potential, and in consequence depends on the heating power introduced, as shown in Fig. 6.11. The onset time of the heating induced annihilation signal could be extracted and mapped to the simulated on-axis depth of the trapping well. The resulting dependence on the power P was fitted by

$$E_{\mathrm{esc}}(P) = a \cdot P^{-b} + c. \tag{6.2}$$

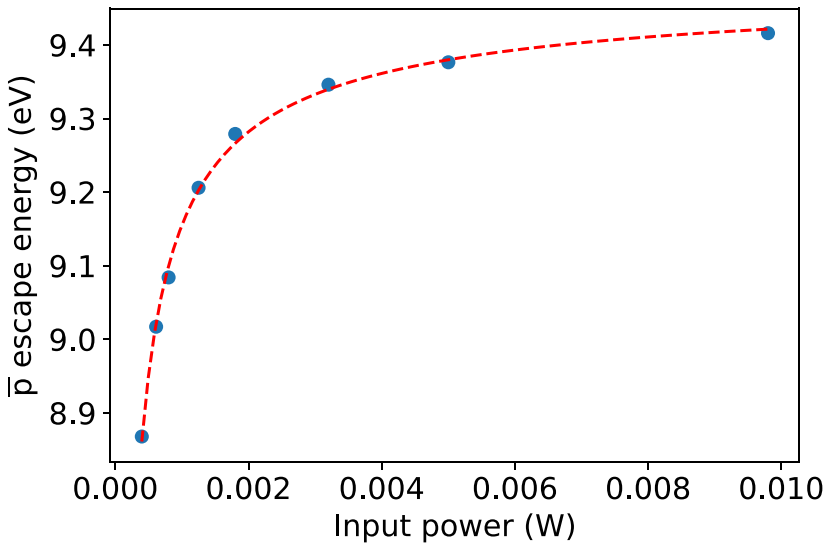

Figure 6.11: Estimated energy of the antiprotons at the time the annihilation signal was observed as a function of the heating power.

If the heating due to the noise is slow enough, the antiprotons will have a well defined and power-dependent energy and the loss function of antiprotons, which is dependent on the temperature of the antiprotons, hence follows a Maxwell-Boltzmann distribution as described in Chapter 2.2.1, can be described by

$$f_{\text{loss}} \propto e^{-\frac{E_{\text{esc}}(P)}{k_{\text{B}} T_{\overline{\text{p}}}}} . \tag{6.3}$$

To test this hypothesis the data of the top plot of Fig. 6.9 were fitted using ROOT with

$$f_{\text{loss}}^{\text{no e}^+}(P) = a^{\text{no e}^+} \cdot e^{-\frac{E_{\text{esc}}(P)}{k_{\text{B}} \cdot (b \cdot P^c + 96\text{K})}} + d^{\text{no e}^+} \tag{6.4}$$

where k_{B} is the Boltzmann constant in units of eV/K and the input power dependent temperature $T_{\overline{\text{p}}} = b \cdot P^c + 96\,\text{K}$, with the last term being the measured temperature of the antiprotons without any heating applied of $(96 \pm 30)\,\text{K}$. The results for the 2-coincidence and 3-coincidence acquisition modes are shown in the top plot of Fig. 6.9 in blue and orange, respectively. The resulting exponents were $c^{\text{2-coin}} = 1.45 \pm 0.04$ for the data in 2-coincidence mode, and $c^{\text{3-coin}} = 2.21 \pm 0.02$ for the 3-coincidence mode. The difference from a linear increase, as measured with positrons, arose from the fact that while the antiprotons were heated, the potential well depth changed, i.e. changing the energy of the antiprotons needed to escape. The amplitudes of the fits $a^{\text{no e}^+}$ being 101 ± 1 (for 2-coincidence) and 98 ± 4 (for 3-coincidence) agreed very well with the physical limit of $Y^{\overline{\text{H}}} = 100$, i.e. the fraction of signal during mixing cannot exceed the number of antiprotons in the dump.

With positrons present in the trap it was seen at positron temperatures $>100\,\text{K}$

that the annihilation signal increased. This was to be expected because the antiprotons could leave the trap due to the applied heating, as in the case that no positrons were present. However, the antiprotons could lose energy via collisions with the positrons as described in Chapter 2, which can be described by the Spitzer collision rate which is $\propto T^{-3/2}$ [54]. Additionally, some fraction of the power was used heating up the positrons, i.e. changing the dependence of the antiproton temperature on the noise power. The effect of the reduction in the temperature can be seen by comparing the two right hand side plots of Fig. 6.10. The antiproton annihilation signal was shifted to later times when positrons were present in the trap, as the temperature increase of the antiprotons was slower compared to the case no positrons were present. To disentangle the loss function and the three-body recombination rate, the following approach was used: Assuming that the positrons and the antiprotons were in thermal equilibrium at the time the antiprotons start to leave the trap due to the power induced increase in temperature. In thermal equilibrium the cooling due to Spitzer collisions and the heating due to the noise are at the same rate, i.e.

$$0 = \frac{\mathrm{d}T_{\overline{\mathrm{p}}}}{\mathrm{d}t} = p_1 \cdot P - p_2 \cdot T_{\overline{\mathrm{p}}}^{-3/2}, \tag{6.5}$$

that is

$$T_{\overline{\mathrm{p}}} = (\tilde{p} \cdot P)^{-2/3}. \tag{6.6}$$

This assumption was used to fit the annihilation signal due to the loss of antiprotons to the data shown in the bottom plot of Fig. 6.9 for which $P > 1.5 \cdot 10^{-3}\,\mathrm{W}$ (i.e. $T_{\mathrm{e}^+} > 127\,\mathrm{K}$). Additionally, it was seen that the potential well depth at the time the antiprotons could leave the trap was approximately constant, hence the escape energy could be averaged to $E_{\mathrm{esc}} = (8.7 \pm 0.1)\,\mathrm{eV}$. Further, the power was converted into the positron temperature using the result of the fit shown in Fig. 6.8. The resulting function, which is shown as the dotted line in the bottom plot of Fig. 6.10, was

$$f_{\mathrm{loss}}(P) = a^{\text{no e}^+} \cdot e^{-\frac{8.7\mathrm{eV}}{k_{\mathrm{B}} \cdot (p_{2,\mathrm{loss}} \cdot T_{\mathrm{e}^+}^{p_{3,\mathrm{loss}}} + 96\mathrm{K})}} + d^{\text{no e}^+}, \tag{6.7}$$

where $T_{\overline{\mathrm{p}}} = p_{2,\mathrm{loss}} \cdot T_{\mathrm{e}^+}^{p_{3,\mathrm{loss}}} + 96\,\mathrm{K}$ is the temperature as a function of the positron temperature (i.e. a function of power due to the linear dependence of the positron temperature on the input power) with changed parameters compared to Eq. (6.4) due to the presence of the positrons. The terms $a^{\text{no e}^+}$ and $d^{\text{no e}^+}$ are taken from the results of the fit from Eq. (6.4), as these two parameter are independent of whether or not positrons are present. The fits for the 2-coincidence data and the 3-coincidence data are shown as the blue and orange dotted lines in the bottom plot of Fig. 6.9, respectively. The resulting exponents were $p_{3,\mathrm{loss}}^{\text{2-coin}} = 1.3 \pm 0.1$ and $p_{3,\mathrm{loss}}^{\text{3-coin}} = 1.5 \pm 0.2$, which was not in agreement with the Spitzer collision rate, which should have resulted in an exponent of $p_{3,\mathrm{loss,Spitzer}} = -2/3$. This suggests that the heating of antiprotons due to the noise

was the dominant factor in the temperature of the antiprotons at the time the signal was observed. This may be caused by the loss of positrons due to the change of the mixing potential, which decreased the space charge of the positrons by approximately a factor of two by the time the antiprotons start to leave the trap. It was shown by Rolston *et al.* [53] that the cooling rate of antiprotons on electrons strongly depends on the ratio of the two species. This is a consequence of electrons dissipating the energy from the antiprotons. As a result, the lower the ratio, i.e. the higher the number of protons to the number of electrons, the smaller the cooling rate. In the work of Rolston *et al.* a ratio of $N_\mathrm{e}/N_\mathrm{p}$ of 10^2, 10^3 and 10^4 was modeled and it was clearly seen that at the lowest ratio the cooling rate was already significantly smaller.

At high input powers hardly any antihydrogen was formed (e.g. the bottom plot on the right hand side of Fig. 6.10 shows no indication of antihydrogen formation in the first 40 s), which means that most of the antiprotons were still confined in the trap. However, the number of positrons decreased due to the lowering of the blocking potential. At the time the antiprotons started to escape (e.g. 40 s), the space charge of the positrons decreased by a factor of ~ 2, but the radius was similar to the beginning of the mixing, as shown in Fig. 6.6. According to Eq. (2.12) in Chapter 2.2 the number of particles needed to decrease by a factor of ~ 2 to account for the decrease in space charge. Therefore, the data presented in Fig. 6.10 had a ratio of positrons to antiprotons on the order of one at the time the antiprotons escaped the well, hence the cooling of antiprotons on positrons would have been highly suppressed. As a consequence the antiproton temperature in f_loss, as defined in Eq. (6.7), mainly depended on the noise power introduced as in the case when no positrons were present in the trap but with a smaller exponent as some fraction of the power was used by the positrons.

The loss-function f_loss for each of the acquisition modes could be subtracted from the data, as shown for the 2-coincidence on the left hand side and for the 3-coincidence on the right hand side of Fig. 6.12, to extract the temperature dependence of the three-body recombination. The large uncertainties in the plot on the right hand side is a consequence of the error propagation from the subtraction. The error bars on these data points were initially much bigger than in the case of the 2-coincidence, due to the lower detection rate of particles. The uncertainty of the parameter of f_loss further increased these error bars.

The data were fitted by

$$f_\mathrm{TBR}(T_{e+}) = p_{1,\mathrm{TBR}} \cdot T_{e^+}^{-p_{2,\mathrm{TBR}}} \tag{6.8}$$

with T_{e^+} being the positron temperatures calculated from the fit shown in Fig. 6.8. The resulting exponent was $p^{\text{2-coin}}_{2,\mathrm{TBR}} = 2.3 \pm 0.4$ for the data acquired in 2-coincidence mode, and $p^{\text{3-coin}}_{2,\mathrm{TBR}} = 2.3 \pm 0.8$ for the 3-coincidence mode, i.e. a temperature dependence of $\propto T^{-2.3\pm0.4}$ and $\propto T^{-2.3\pm0.8}$, respectively. The fits are shown as the dash-dotted lines in the bottom plot of Fig. 6.9 and in Fig. 6.12. The combined fit functions as a function

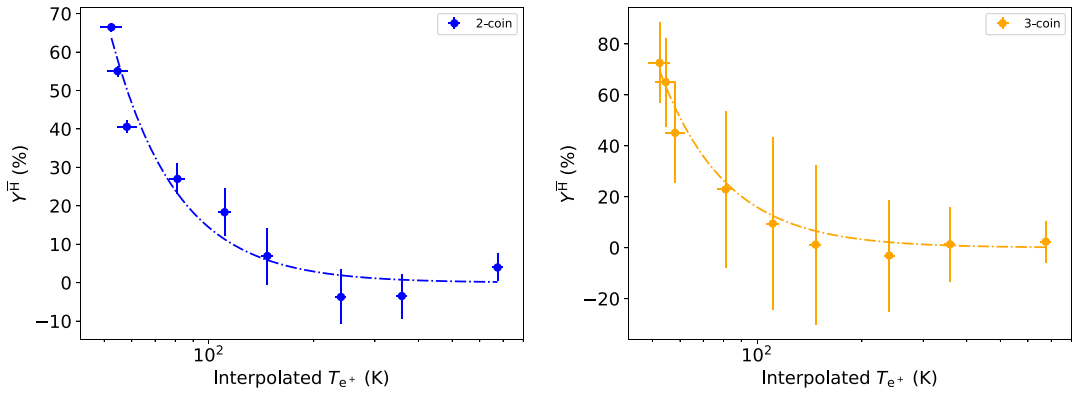

Figure 6.12: $Y^{\overline{H}}$, as defined in Eq. (6.1), with the loss function f_{loss} subtracted from the data acquired in 2-coincidence (left) and 3-coincidence (right) mode. The dash-dotted lines are the fits for three-body recombination using Eq. (6.8). See text for further information.

of positron temperature

$$f_{\text{total}} = f_{\text{loss}} + f_{\text{TBR}} \tag{6.9}$$

are shown as the dashed lines in the bottom plot of Fig. 6.9.

The measurement deviates slightly from the purely theoretical prediction of $\propto T^{-4.5}$ [65, 66], as described in Chapter 2.3.1. However, the theoretical expression does not include scattering of the antihydrogen atoms within the plasma, which alters the temperature dependence of the formation rate, as it was described in Section 2.3.2 [68]. The measurement agrees very well with the results of the simulations, which span a temperature dependence of $\propto T^{-4.5}$ to $\propto T^{-2.0}$, depending on the density of the positron plasma in the range of $n \sim 10^{16}\,\mathrm{m}^{-3}$ to $n \sim 10^{14}\,\mathrm{m}^{-3}$.

6.4.1 Comparison to previous result

The ATHENA collaboration at CERN reported the first measurement of the temperature dependence of antihydrogen production in 2004 [119]. The data of this measurement are shown in Fig. 6.13 and the findings can be summarised to: (i) the antihydrogen production rate decreased with an increase in the positron temperature, (ii) antihydrogen production was clearly present for room temperature positrons, and (iii) the formation did not scale as a simple power law with the positron temperature [119].

In both measurements the decrease of the production of antihydrogen atoms with increasing positron temperatures was observed. To discuss the other findings, the positron temperature measurement of the ATHENA collaboration needs to be described in more detail. The absolute temperature was not measured directly but the relative temperature increase was extracted from the quadrupole mode frequency of the plasma [120]. It was assumed that the positron temperature relaxed to the temperature of the trap electrodes, which was 15 K, i.e. the unperturbed case yielding a positron temperature

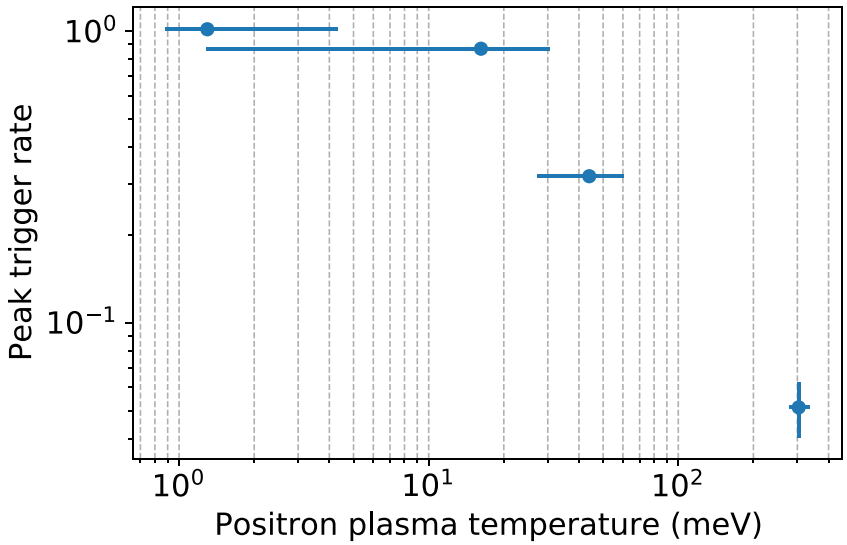

Figure 6.13: Temperature dependence of antihydrogen production measured by the ATHENA collaboration. Data from [119]. See text for further information.

of $\sim 15\,\mathrm{K}$. The minimum observable temperature increase was $\sim 15\,\mathrm{meV}$, corresponding to an increase of $\sim 175\,\mathrm{K}$ [119]. The x-axis of the data presented in Fig. 6.13 can be converted into a temperature range of $\sim 15\,\mathrm{K}$ up to $\sim 3500\,\mathrm{K}$.

In the preceding section, a power law as $\propto T^{-2.3\pm0.8}$ was in reasonable good agreement with the measured data shown in the bottom plot of Fig. 6.9 and in Fig. 6.12. The result presented by the ATHENA collaboration shown in Fig. 6.13, indicated a leveling-off of the antihydrogen production rate at lower temperatures. Assuming that three-body recombination was the dominant process for antihydrogen production at temperatures $< 100\,\mathrm{K}$, an increase in the rate should have been observed. The authors described that neither a simple power law nor a mixture of the power laws for three-body and radiative recombination described the data. Even though it was not possible to find a power law describing the full measurement, the authors presented the best-fit of the temperature dependence to be $T^{-0.7\pm0.2}$. This result was in agreement with a pure radiative recombination process, calculated in [121] to be $\propto T^{-0.63}$, the measured antihydrogen production rate was one order of magnitude larger than radiative recombination would have suggested for a positron temperature of 15 K. However, the presence of radiative recombination could not be excluded. Further, the mechanism for the turnover in the production rate was unclear but the possibility of an uncertainty in the measured positron temperature was mentioned as a possible cause.

The difference in the temperature dependence of the antihydrogen formation presented in this work and by the ATHENA collaboration is not yet understood. However, there are several mechanisms which could play a role: First, as mentioned above, the temperature was not measured by the ATHENA collaboration, hence assuming that the positron plasma relaxes to the electrode temperature may be wrong. It was seen in

the ASACUSA-Cusp experiment in previous traps, that the temperature of an electron plasma did not relax to the temperature of the electrodes [52]. Only after the design of a trap with the focus on the reduction of the positron temperature and improved control over the plasma parameter using SDREVC, it was possible to get plasma temperatures within 20 K of the electrode temperatures. Further, a turnover in the production rate could suggest a saturation effect of the production due to some other limitation rather than the positron temperature. For example in the data presented in this work the antihydrogen production seemed to be at maximum at the lowest achievable temperature of ~ 24 K. It was seen that in a mixing time of 60 s a large fraction of the antiprotons were converted into antihydrogen atoms, hence limiting the antihydrogen production rate.

Chapter 7

Conclusion and outlook

In this work several improvements to the ASACUSA-Cusp experiment were presented which yield significant advances towards a measurement of the hyperfine splitting of antihydrogen in a low magnetic field region.

The positron system for the ASACUSA-Cusp experiment was upgraded. One part of the upgrade was the change of the rare-gas moderator system and the Surko-type buffer gas trap as described in [69] to a system previously used at Aarhus University. In the course of the work, this system was characterised. The moderator efficiency of $\varepsilon_{\mathrm{M}} = (0.18 \pm 0.04)\,\%$ and the trapping efficiency of $\varepsilon_{\mathrm{T}} = (13.8 \pm 4.2)\,\%$ of the upgraded positron system were comparable with the results in the old positron system of $\varepsilon_{\mathrm{M}} = (0.25 \pm 0.1)\,\%$ and $\varepsilon_{\mathrm{T}} = (17.4 \pm 1.8)\,\%$[69]. The second part of the upgrade was the installation of a new 3$^{\mathrm{rd}}$ stage accumulator, which stores several bunches of positrons coming from the buffer gas trap. The successfull accumulation of roughly one million positrons in $\sim 60\,\mathrm{s}$ (the main limitation during this work was the low activity of the source), the high pressure buffer gas trap could be separated from the accumulator by closing a gate valve in between. The gas was pumped out within 3 s reaching a pressure of $< 10^{-8}\,\mathrm{mbar}$ and the positrons were transferred into the mixing trap. The main advantages of the upgraded system are that with the installation of the accumulator a continuous stacking of positrons is possible, independent of the other apparatuses. The previous system had down times during mixing. This opens up the possibility of a constant accumulation of positrons, hence decrease the time to reach a sufficient number of particles for mixing. Additionally, all magnets on the positron system are water-cooled, hence no liquid helium is needed anymore.

Even though the system is operating, some limitations were seen during operation, which will be addressed in future to increase the efficiency of the accumulation of positrons. Firstly, a new source was delivered earlier last year, which should increase the number of positrons available by a factor of 25. Secondly, the moderation efficiency of 0.2 % may be optimised by adjusting the moderator electrode temperature, the neon pressure during, and the time of the moderator growth, which requires a systematic study. Finally, the lifetime of the stacked positrons may be increased by installing a

pumping restriction between the buffer gas trap and the accumulator.

A low energy proton source was successfully integrated into the experiment. The purpose of this implementation is to investigate and optimise the mixing process at times no antiprotons are delivered (for example during the next Long Shutdown at CERN) by making hydrogen instead of antihydrogen. It was shown that more than one million protons could be caught in the Cusp trap within 30 s. Further, the first demonstration of cooling protons with positrons in the Cusp trap to a temperature of (550 ± 40) K was achieved. This opened up the possibility of attempting to produce hydrogen in the experiment to test the same techniques which will be used for antihydrogen. Due to the limited time available for this investigation, so far no clear evidence of hydrogen production was observed. Nevertheless, it was shown by the simultaneous preparation of electrons, protons, and positrons that this system will be useful in future for optimisation of the experimental techniques, especially for manipulation and investigation of the plasma properties needed for mixing. This had been already very useful for the antihydrogen mixing results shown in this work, as the investigation of the hydrogen mixing sequence gave some guidance to possible measurement techniques during the sequence, which were later applied on the antihydrogen experiments.

After the preparation of positrons antiprotons in the Cusp trap, reaching a positron temperature of (24 ± 4) K, which was five times colder than previously achieved in this trap, and an antiproton temperature of (96 ± 30) K, the production of antihydrogen was studied. It was shown that up to 80 % of antiprotons could be converted into antihydrogen (equal to ~ 0.4 million atoms in this work) when merging the two plasmas slowly in 60 s, which was eight times higher than other experiments have reported [122], and an increase from 2% previously reported by the ASACUSA collaboration [39]. It was possible to investigate the evolution of the density and temperature of the positrons and antiprotons over a wide range of mixing times. These measurements showed that the positron temperature stays constant up to a mixing time of at least 60 s. As a consequence, the formation of the antihydrogen atoms seems to not being limited by this quantity, but rather by the number of antiprotons used for mixing.

By applying noise onto one Cusp trap electrode it was possible to heat up the positrons during mixing and measure the resulting antihydrogen formation efficiency. It was observed that the production of antihydrogen decreased drastically at a positron temperature of ~ 50 K. To estimate the strength of this decrease a simplified model was applied to decouple the annihilation signal from antihydrogen formation and antiprotons which gained enough energy to escape the trapping well. The resulting temperature dependence, presenting the more conservative value of the 3-coincidence data acquisition, was $\propto T^{-2.3\pm0.8}$, which is fairly close to the theoretical value of $\propto T^{-4.5}$. This measurement confirmed a low positron temperature such that three-body recombination is the main formation mechanism. A deviation from a previous result by the ATHENA collaboration of $T^{-0.7\pm0.2}$ was observed. The reason for this deviation is not fully understood, but might be connected to the different methods to an underestimate of the

temperature of the positron plasma in the previous work.

In this work the beam formation, i.e. the number of antihydrogen atoms which are leaving the trapping electrodes to the downstream side of the experiment, was not verified. However, a different approach may be more suitable for the beam formation. Figure 7.1 shows the mixing technique used in this work (top plot), and the scheme which should favour beam formation (bottom plot). The idea in the second case is that the antiprotons are held in the potential well at $z \sim -0.37\,\mathrm{m}$ and are slowly released such that they pass only once through the centre of the positrons held at $z \sim -0.27\,\mathrm{m}$. Simulations indicated that beam formation should be favoured due to the forward momentum of the antiprotons [123]. In the simulation a maximum of 13 % of the antihydrogen atoms produced was found to form a beam assuming an antiproton energy of 0.05 eV, a 1 cm long positron plasma with a temperature of 5 K, a positron density of $10^{15}\,\mathrm{m}^{-3}$ and a magnetic field of 1 T. However, with these parameters the overall antihydrogen production rate was reduced by 60 % compared an incoming antiproton energy of 0.004 eV. Increasing the temperature of the positrons decreased both the beam formation and the antihydrogen formation. Additionally, if the antiprotons are injected away from the center of the trap, the beam formation is suppressed. Nevertheless, the simulations suggest that this technique can increase the production of an antihydrogen beam, albeit experimental difficulties, such as the exact matching of the energy of the antiprotons and the positrons and the low temperatures, might be challenging. Furthermore, this simulation showed the necessity of a high production rate of antihydrogen atoms for the ASACUSA-Cusp collaboration to form an antihydrogen beam.

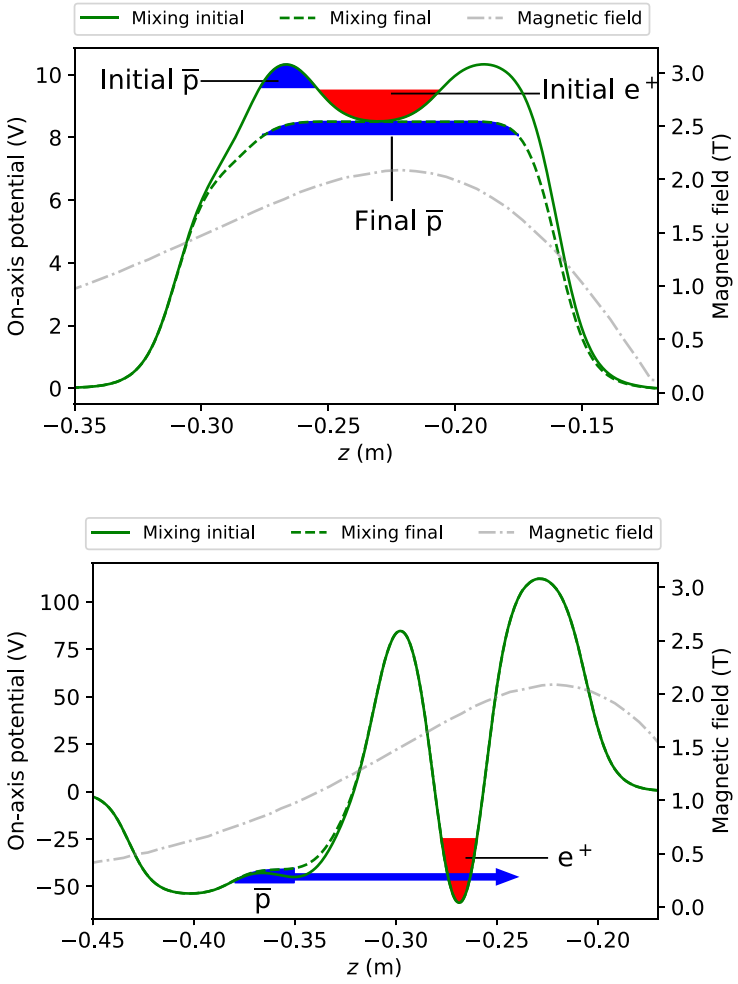

Figure 7.1: Schemes for combining the antiprotons and positrons to form antihydrogen in the Cusp trap. The slow merging technique used in this work is shown in the top plot. The bottom plot shows the scheme reported to favour the beam formation.

The next steps in the experiment are to measure the antihydrogen atoms which formed a beam, i.e. measure the fraction of atoms which reach the antihydrogen detector downstream of the Cusp trap. This can be achieved by measuring the antihydrogen atoms annihilating on the BGO detector. After the confirmation that the antihydrogen form a beam, a measurement of the principal quantum number will be performed to see how the temperature and density of the positron plasma affects the ground-state population. As a consequence, the preparation of the plasma will be optimised to increase the fraction of ground-state atoms, and finally, perform the first measurement of the hyperfine splitting of antihydrogen using a spin-polarised beam of atoms in a low magnetic field.

Appendix A

Electrical circuits

A.1 FPS filter box

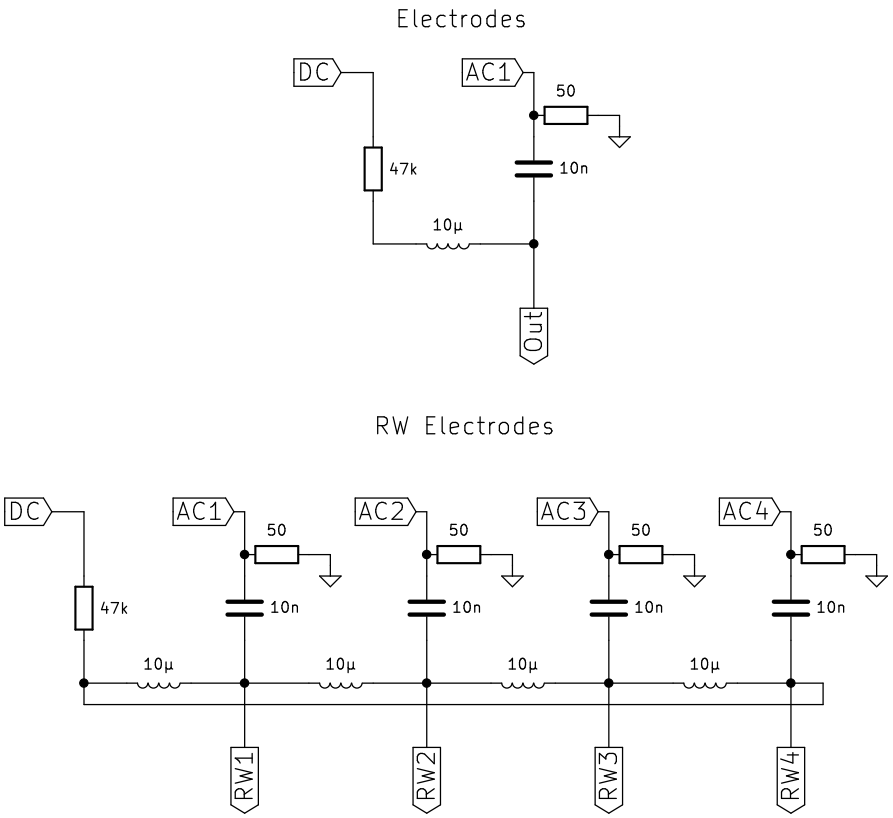

Figure A.1: Filter box used for the FPS system to be able to apply fast pulses to each individual electrode and the RW.

A.2 Charge integrating amplifier

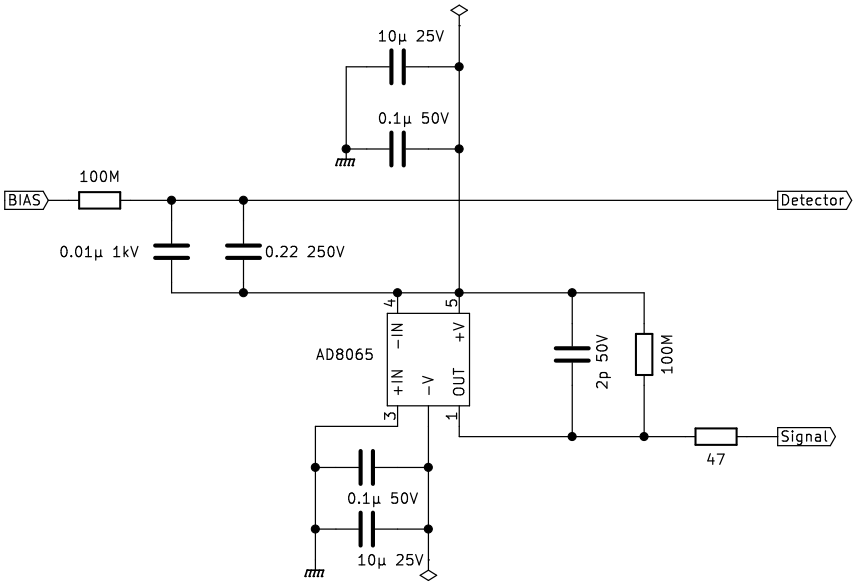

Figure A.2: Charge integrating amplifier for measuring the number of positrons.

A.3 Proton Source RF-coupling box

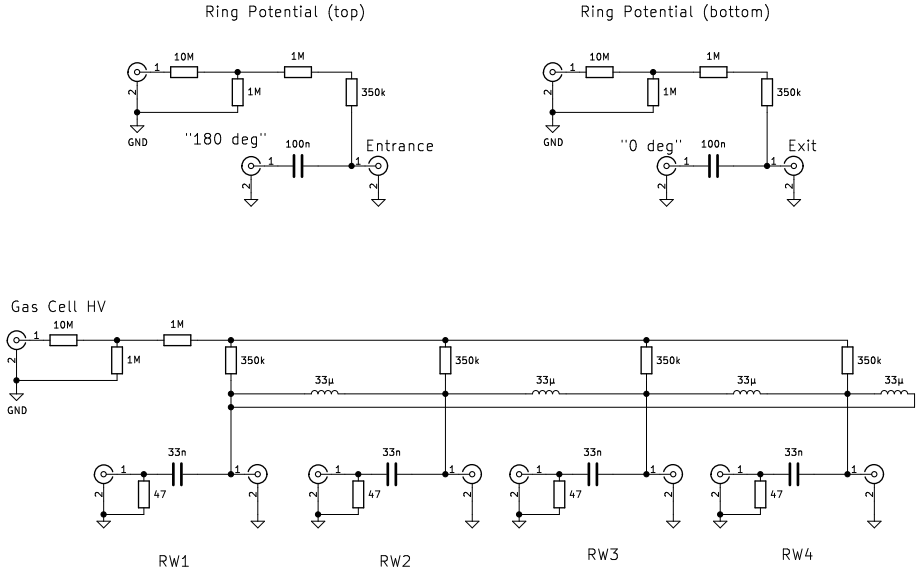

Figure A.3: Circuit of the RF-coupling box for the proton source.

Appendix B

Control Software

In order to avoid a constantly growing LabView program with hard coded parameters to control the experiment, E.D. Hunter had the idea of an upgrade of the control software of the ASACUSA-Cusp experiment. The basic idea behind this was to have an interchangeable control software for all three apparatuses (positron system, Cusp trap and MUSASHI), easy implementation of new devices and a timed control of parameter settings. The control program was implemented in LabView 2019 and the basic principle of the software is described in this section.

Figure B.1 shows a sketch of the user interface. One control sequence, which is called "Cue", consists of several instructions which can be divided in "Parameter" and "Macro". Each instruction can be set to be repeated ("Reps") and to an execution time, which lower limit is set by the communication time with devices or the ramp speed of the amplifiers used for applying potentials to the electrodes. A parameter is a slow change, which typically takes hundreds of milliseconds, e.g. the settings of the RW frequency and amplitudes by an arbitrary waveform generator. A Macro is a sequence of instructions to change the values of the electrode potentials and sending/receiving triggers, e.g. enabling the output of the waveform generator to apply a RW electric field, opening gate valves, or waiting for an input trigger which tells to continue with the next instruction.

As an example of a Cue the stacking in the accumulator is described: First, the RW parameters for the accumulator and the BGT are set in the arbitrary waveform generators (can be seen as "Parameter 1" in Fig. B.1). After the set time of 1000 ms, which is approximately the time needed to communicate with the waveform generators, the HV inputs of the pulsers to extract the positrons from the BGT and catch in the accumulator is set ("Parameter 2"). In the next instruction a Macro ("Macro 1") is executed to open the GV between the RGM and the BGT, which is set to 3 s to make sure it is fully open. The next step ("Parameter 3") is turning on the magnets needed for transporting the positrons into the accumulator. This instruction is set to 5 s to assure the magnets reach the set field before the software continues. "Macro 2" is used to enable the output of the arbitrary waveform generator to apply the RW electric field

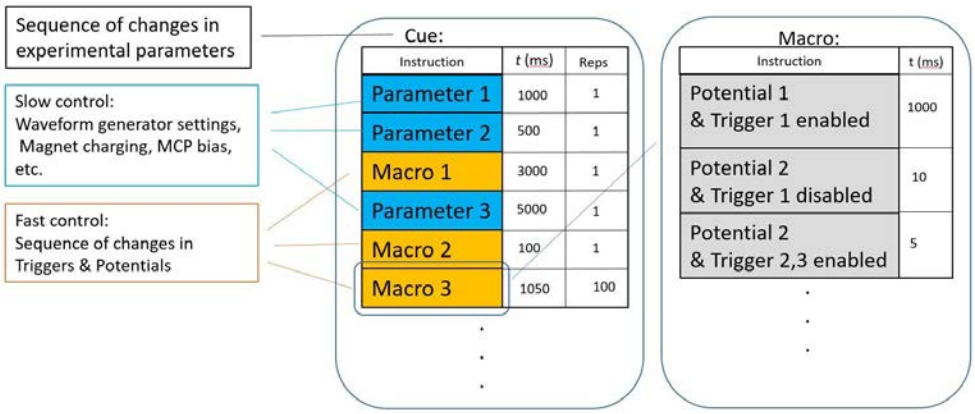

Figure B.1: Principle of the control software showing a "Cue" with a few "Parameter" and "Macro" changes, as well as an example of a Macro. See text for further information.

before the positrons are let into the BGT. The following macro ("Macro 3") is repeated 100 times, and is used to stack several bunches from the BGT in the accumulator. Here, the first instruction sets the potentials ("Potential 1") of the BGT and accumulator and leaves it for 1 s to fill positrons into the BGT. The next instruction reduces the moderator bias to stop the filling, changes the accumulator potentials to the catching well ("Potential 2"), and disables the output of the waveform generator to stop the application of the RW electric field. No potential change is performed in the next step but the output of the HV pulsers to extract and catch the positrons are enabled, i.e. the transfer happens. Afterwards, these triggers are disabled again and the potential is set to "Potential 1" and the filling repeats. After finishing all repetitions the positrons can be send into the Cusp trap or can be extracted on a MCP, which work the same way as described above by adding the needed macro or parameter change.

The advantages of the new control software are that first, every cue as well as macro is saved on the control computers, which makes reproducibility tests easy. That system replaces the previous, hard coded LabView program, which overwrote the potentials whenever an improved operation was found. Further, the timing for each instruction enables a much finer control over the potential changes, improving the plasma control in the traps. An additional advantage is that is easily accessible for also for people who are new to the collaboration, as the working principle is the same for all apparatuses and the construction of a Cue is straightforward.

List of acronyms and abbreviations

AD Antiproton Decelerator

AMT ASACUSA Micromegas Tracker

ASACUSA Atomic Spectroscopy And Collisions Using Slow Antiprotons

BGO Bismuth-Germanium-Oxide, $Bi_4Ge_3O_{12}$

BGT Buffer Gas Trap

BoPET Biaxially Oriented PolyEthylene Terephtalate

BSM Beyond the Standard Model

CEM Channel Electron Multiplier

CERN Conseil Européene pour la Recherche Nucléaire

CSS Cusp Segmented Scintillator

DCE Downstream Catching Electrode

DS Downstream

EE Extraction Electrodes

ELENA Extra Low ENergy Antiproton ring

EVC Evaporative Cooling

FI Field Ionisers

FPS First Point Scientific Inc. (used as an acronym for the upgraded positron system)

GV Gate Valve

HFS High-Field Seeker

ID Inner Diameter

LFS Low-Field Seeker

LHS Left hand side

MCP Microchannel Plate

MRE Multi Ring Electrode

MUSASHI Mono-energetic Ultra-Slow Antiproton Source for High-precision Investigation

PS Phosphor Screen

RF Radio-Frequency

RFQD Radio-Frequency Quadrupole Decelerator

RGM Rare Gas Moderator

RHS Right hand side

RW Rotating Wall

SDR Strong-Drive Regime

SDREVC Strong-Drive Evaporative Cooling

SiPM Sillicon Photomultiplier

SM Standard Model

SME Standard Model Extension

TBR Three-Body Recombination

TMP Turbo-Molecular Pump

UCE Upstream Catching Electrode

US Upstream

UHV Ultra-High Vacuum

List of Tables

List of Figures

Bibliography

1. Dirac, P. A. M. The quantum theory of the electron. *Proceedings of the Royal Society of London. Series A, Containing Papers of a Mathematical and Physical Character* **117,** 610–624. doi:10.1098/rspa.1928.0023 (1928).
2. Dirac, P. A. M. A theory of electrons and protons. *Proceedings of the Royal Society of London. Series A, Containing Papers of a Mathematical and Physical Character* **126,** 360–365. doi:10.1098/rspa.1930.0013 (1930).
3. Anderson, C. D. The Positive Electron. *Physical Review* **43,** 491–494. doi:10.1103/PhysRev.43.491 (1933).
4. Anderson, C. D. The Apparent Existence of Easily Deflectable Positives. *Science* **76,** 238–239. doi:10.1126/science.76.1967.238 (1932).
5. Bennett, C. L. *et al.* Nine-Year *Wilkinson Microwave Anisotropy Probe* (*WMAP*) Observations: Final Maps and Results. *The Astrophysical Journal Supplement Series* **208,** 20. doi:10.1088/0067-0049/208/2/20 (2013).
6. Ahlen, S. P. *et al.* New Limit on the Low-Energy Antiproton/Proton Ratio in the Galactic Cosmic Radiation. *Physical Review Letters* **61,** 145–148. doi:10.1103/PhysRevLett.61.145 (1988).
7. Pontecorvo, B. Neutrino experiments and the problem of conservation of leptonic charge. *Soviet Physics JETP* **26** (1968).
8. Davis, R. A review of the homestake solar neutrino experiment. *Progress in Particle and Nuclear Physics* **32,** 13–32. doi:10.1016/0146-6410(94)90004-3 (1994).
9. Noether, E. Invariante Variationsprobleme. *Nachrichten von der Gesellschaft der Wissenschaften zu Göttingen, Mathematisch-Physikalische Klasse,* 235–257 (1918).
10. Lüders, G. On the equivalence of invariance under time reversal and under particle-antiparticle conjugation for relativistic field theories. *Dan. Mar. Fys. Medd* **28** (1954).
11. Bell, J. S. & Peierls, R. E. Time reversal in field theory. *Proceedings of the Royal Society of London. Series A. Mathematical and Physical Sciences* **231,** 497–495. doi:10.1098/rspa.1955.0189 (1955).

12. Wu, C. S., Ambler, E., Hayward, R. W., Hoppes, D. D. & Hudson, R. P. Experimental Test of Parity Conservation in Beta Decay. *Physical Review* **105,** 1413–1415. doi:10.1103/PhysRev.105.1413 (1957).

13. Christenson, J. H., Cronin, J. W., Fitch, V. L. & Turlay, R. Evidence for the 2π Decay of the $K_2{}^0$ Meson. *Physical Review Letters* **13,** 138–140. doi:10.1103/PhysRevLett.13.138 (1964).

14. Lees, J. P. *et al.* Observation of Time-Reversal Violation in the B^0 Meson System. *Physical Review Letters* **109,** 211801. doi:10.1103/PhysRevLett.109.211801 (2012).

15. Sakharov, A. D. Violation of CP invariance, C asymmetry, and baryon asymmetry of the universe. *Soviet Physics Uspekhi* **34,** 392. doi:10.1070/PU1991v034n05ABEH002497 (1991).

16. Bertolami, O., Colloday, D., Kostelecký, V. A. & Potting, R. CPT violation and baryogenesis. *Physics Letters B* **395,** 178–183. doi:10.1016/S0370-2693(97)00062-2 (1997).

17. Colladay, D. & Kostelecký, V. A. CPT violation and the standard model. *Physical Review D* **55,** 6760–6774. doi:10.1103/PhysRevD.55.6760 (1997).

18. Colladay, D. & Kostelecký, V. A. Lorentz-violating extension of the standard model. *Physical Review D* **58,** 116002. doi:10.1103/PhysRevD.58.116002 (1998).

19. Kostelecký, V. A. & Vargas, A. J. Lorentz and C P T tests with hydrogen, antihydrogen, and related systems. *Physical Review D* **92,** 056002. doi:10.1103/PhysRevD.92.056002 (2015).

20. Karshenboim, S. G. Precision physics of simple atoms: QED tests, nuclear structure and fundamental constants. *Physics Reports* **422,** 1–63. doi:https://doi.org/10.1016/j.physrep.2005.08.008 (2005).

21. Kostelecký, V. A. & Mewes, M. Fermions with Lorentz-violating operators of arbitrary dimension. *Physical Review D* **88,** 096006. doi:10.1103/PhysRevD.88.096006 (2013).

22. Mohri, A. & Yamazaki, Y. A possible new scheme to synthesize antihydrogen and to prepare a polarised antihydrogen beam. *Europhysics Letters (EPL)* **63,** 207–213. doi:10.1209/epl/i2003-00509-0 (2003).

23. Hori, M. *et al.* Two-photon laser spectroscopy of antiprotonic helium and the antiproton-to-electron mass ratio. *Nature* **475,** 484–488. doi:10.1038/nature10260 (2011).

24. Widmann, E., Hayano, R. S., Hori, M. & Yamazaki, T. Measurement of the hyperfine structure of antihydrogen. *Nuclear Instruments and Methods in Physics Research Section B: Beam Interactions with Materials and Atoms. Low Energy Antiproton Physics (LEAP'03)* **214,** 31–34. doi:10.1016/j.nimb.2003.08.021 (2004).

25. Amoretti, M. *et al.* Production and detection of cold antihydrogen atoms. *Nature* **419,** 456–459. doi:10.1038/nature01096 (2002).

26. Gabrielse, G. *et al.* Background-Free Observation of Cold Antihydrogen with Field-Ionization Analysis of its States. *Physical Review Letters* **89,** 213401. doi:10.1103/PhysRevLett.89.213401 (2002).

27. Ahmadi, M. *et al.* Investigation of the fine structure of antihydrogen. *Nature* **578,** 375–380. doi:10.1038/s41586-020-2006-5 (2020).

28. Ahmadi, M. *et al.* Observation of the 1S–2S transition in trapped antihydrogen. *Nature* **541,** 506–510. doi:10.1038/nature21040 (2017).

29. Ahmadi, M. *et al.* Observation of the hyperfine spectrum of antihydrogen. *Nature* **548,** 66–69. doi:10.1038/nature23446 (2017).

30. Anderson, E. K. *et al.* Observation of the effect of gravity on the motion of antimatter. *Nature* **621,** 716–722. doi:10.1038/s41586-023-06527-1 (2023).

31. Nagahama, H. *et al.* Sixfold improved single particle measurement of the magnetic moment of the antiproton. *Nature Communications* **8,** 14084. doi:10.1038/ncomms14084 (2017).

32. Ulmer, S. *et al.* High-precision comparison of the antiproton-to-proton charge-to-mass ratio. *Nature* **524,** 196–199. doi:10.1038/nature14861 (2015).

33. Smorra, C. *et al.* BASE-STEP: A transportable antiproton reservoir for fundamental interaction studies. *Review of Scientific Instruments* **94,** 113201. doi:10.1063/5.0155492 (2023).

34. Kellerbauer, A. *et al.* Proposed antimatter gravity measurement with an antihydrogen beam. *Nuclear Instruments and Methods in Physics Research Section B: Beam Interactions with Materials and Atoms. Low Energy Positron and Positronium Physics* **266,** 351–356. doi:10.1016/j.nimb.2007.12.010 (2008).

35. Perez, P. & Rosowsky, A. A new path toward gravity experiments with antihydrogen. *Nuclear Instruments and Methods in Physics Research Section A: Accelerators, Spectrometers, Detectors and Associated Equipment* **545,** 20–30. doi:10.1016/j.nima.2005.01.301 (2005).

36. Aumann, T. *et al.* PUMA, antiProton unstable matter annihilation. *The European Physical Journal A* **58,** 88. doi:10.1140/epja/s10050-022-00713-x (2022).

37. Rabi, I. I., Millman, S., Kusch, P. & Zacharias, J. R. The Molecular Beam Resonance Method for Measuring Nuclear Magnetic Moments. The Magnetic Moments of $_3Li^6$, $_3Li^7$ and $_9F^{19}$. *Physical Review* **55,** 526–535. doi:10.1103/PhysRev.55.526 (1939).

38. Nowak, L. *et al.* CPT and Lorentz symmetry tests with hydrogen using a novel in-beam hyperfine spectroscopy method applicable to antihydrogen experiments. *Physics Letters B* **858,** 139012. doi:10.1016/j.physletb.2024.139012 (2024).

39. Enomoto, Y. *et al.* Synthesis of Cold Antihydrogen in a Cusp Trap. *Physical Review Letters* **105,** 243401. doi:10.1103/PhysRevLett.105.243401 (2010).

40. Kuroda, N. *et al.* A source of antihydrogen for in-flight hyperfine spectroscopy. *Nature Communications* **5,** 3089. doi:10.1038/ncomms4089 (2014).

41. Kolbinger, B. *et al.* Measurement of the principal quantum number distribution in a beam of antihydrogen atoms. *The European Physical Journal D* **75,** 91. doi:10.1140/epjd/s10053-021-00101-y (2021).

42. Penning, F. Die glimmentladung bei niedrigem druck zwischen koaxialen zylindern in einem axialen magnetfeld. *Physica* **3,** 873–894. doi:10.1016/S0031-8914(36)80313-9 (1936).

43. Dehmelt, H. in *Advances in Atomic and Molecular Physics* 53–72 (Elsevier, 1968). ISBN: 978-0-12-003803-9. doi:10.1016/S0065-2199(08)60170-0.

44. Gabrielse, G. & Mackintosh, F. C. Cylindrical Penning traps with orthogonalized anharmonicity compensation. *International Journal of Mass Spectrometry and Ion Processes* **57,** 1–17. doi:10.1016/0168-1176(84)85061-2 (1984).

45. Gabrielse, G., Haarsma, L. & Rolston, S. L. Open-endcap Penning traps for high precision experiments. *International Journal of Mass Spectrometry and Ion Processes* **88,** 319–332. doi:10.1016/0168-1176(89)85027-X (1989).

46. Malmberg, J. H. & Driscoll, C. F. Long-Time Containment of a Pure Electron Plasma. *Physical Review Letters* **44,** 654–657. doi:10.1103/PhysRevLett.44.654 (1980).

47. Knoop, M., Madsen, N. & Thompson, R. C. *Trapped Charged Particles* (World Scientific Publishing Europe Ltd, 2016).

48. Mitchell, D. W. & Smith, R. D. Cyclotron motion of two Coulombically interacting ion clouds with implications to Fourier-transform ion cyclotron resonance mass spectrometry. *Physical Review E* **52,** 4366–4386. doi:10.1103/PhysRevE.52.4366 (1995).

49. Chen, F. F. *Introduction to Plasma Physics and Controlled Fusion* 3rd ed. (Springer Cham, 2016).

50. Ketterle, W. & Druten, N. J. V. in *Advances in Atomic, Molecular, and Optical Physics* 181–236 (Academic Press, 1996). doi:https://doi.org/10.1016/S1049-250X(08)60101-9.

51. Andresen, G. B. *et al.* Evaporative Cooling of Antiprotons to Cryogenic Temperatures. *Physical Review Letters* **105,** 013003. doi:10.1103/PhysRevLett.105.013003 (2010).

52. Amsler, C. *et al.* Reducing the background temperature for cyclotron cooling in a cryogenic Penning–Malmberg trap. *Physics of Plasmas* **29,** 083303. doi:10.1063/5.0093360 (2022).

53. Rolston, S. L. & Gabrielse, G. Cooling antiprotons in an ion trap. *Hyperfine Interactions* **44,** 233–245. doi:10.1007/BF02398673 (1989).

54. Spitzer, L. *Physics of fully ionized gases* 2nd ed. (Interscience Publ., New York, 1957).

55. Huang, X.-P., Anderegg, F., Hollmann, E. M., Driscoll, C. F. & O'Neil, T. M. Steady-State Confinement of Non-neutral Plasmas by Rotating Electric Fields. *Physical Review Letters* **78,** 875–878. doi:10.1103/PhysRevLett.78.875 (1997).

56. Anderegg, F., Hollmann, E. M. & Driscoll, C. F. Rotating Field Confinement of Pure Electron Plasmas Using Trivelpiece-Gould Modes. *Physical Review Letters* **81,** 4875–4878. doi:10.1103/PhysRevLett.81.4875 (1998).

57. Isaac, C. A., Baker, C. J., Mortensen, T., Van Der Werf, D. P. & Charlton, M. Compression of Positron Clouds in the Independent Particle Regime. *Physical Review Letters* **107,** 033201. doi:10.1103/PhysRevLett.107.033201 (2011).

58. Danielson, J. R. & Surko, C. M. Torque-Balanced High-Density Steady States of Single-Component Plasmas. *Physical Review Letters* **94,** 035001. doi:10.1103/PhysRevLett.94.035001 (2005).

59. Danielson, J. R. & Surko, C. M. Radial compression and torque-balanced steady states of single-component plasmas in Penning-Malmberg traps. *Physics of Plasmas* **13,** 055706. doi:10.1063/1.2179410 (2006).

60. Ahmadi, M. *et al.* Enhanced Control and Reproducibility of Non-Neutral Plasmas. *Physical Review Letters* **120,** 025001. doi:10.1103/PhysRevLett.120.025001 (2018).

61. Carruth, C. *Methods for plasma stabilization and control to improve antihydrogen production* PhD thesis (University of California, Berkeley, 2018).

62. Charlton, M. Antihydrogen production in collisions of antiprotons with excited states of positronium. *Physics Letters A* **143,** 143–146. doi:10.1016/0375-9601(90)90665-B (1990).

63. Poth, H. Antihydrogen formation through positron-antiproton radiative combination. *Applied Physics A* **43,** 287–293. doi:10.1007/BF00635185 (1987).

64. Robicheaux, F. Atomic processes in antihydrogen experiments: a theoretical and computational perspective. *Journal of Physics B: Atomic, Molecular and Optical Physics* **41,** 192001. doi:10.1088/0953-4075/41/19/192001 (2008).

65. Glinsky, M. E. & O'Neil, T. M. Guiding center atoms: Three-body recombination in a strongly magnetized plasma. *Physics of Fluids B: Plasma Physics* **3,** 1279–1293. doi:10.1063/1.859820 (1991).

66. Robicheaux, F. & Hanson, J. D. Three-body recombination for protons moving in a strong magnetic field. *Physical Review A* **69,** 010701. doi:10.1103/PhysRevA.69.010701 (2004).

67. Bass, E. M. & Dubin, D. H. E. Antihydrogen formation from antiprotons in a pure positron plasma. *Physics of Plasmas* **16,** 012101. doi:10.1063/1.3040168 (2009).

68. Radics, B., Murtagh, D. J., Yamazaki, Y. & Robicheaux, F. Scaling behavior of the ground-state antihydrogen yield as a function of positron density and temperature from classical-trajectory Monte Carlo simulations. *Physical Review A* **90,** 032704. doi:10.1103/PhysRevA.90.032704 (2014).

69. Murtagh, D. *et al.* Slow positron production and storage for the ASACUSA-Cusp experiment. *Journal of Plasma Physics* **89,** 905890608. doi:10.1017/S0022377823001034 (2023).

70. Gullikson, E. M. & Mills, A. P. Positron Dynamics in Rare-Gas Solids. *Physical Review Letters* **57,** 376–379. doi:10.1103/PhysRevLett.57.376 (1986).

71. Mills, A. P. & Gullikson, E. M. Solid neon moderator for producing slow positrons. *Applied Physics Letters* **49,** 1121–1123. doi:10.1063/1.97441 (1986).

72. Surko, C. M., Leventhal, M. & Passner, A. Positron Plasma in the Laboratory. *Physical Review Letters* **62,** 901–904. doi:10.1103/PhysRevLett.62.901 (1989).

73. Murphy, T. J. & Surko, C. M. Positron trapping in an electrostatic well by inelastic collisions with nitrogen molecules. *Physical Review A* **46,** 5696–5705. doi:10.1103/PhysRevA.46.5696 (1992).

74. Kersevan, R. & Pons, J.-L. Introduction to MOLFLOW+: New graphical processing unit-based Monte Carlo code for simulating molecular flows and for calculating angular coefficients in the compute unified device architecture environment. *Journal of Vacuum Science & Technology A: Vacuum, Surfaces, and Films* **27,** 1017–1023. doi:10.1116/1.3153280 (2009).

75. *COMSOL Multiphysics®* Stockholm, Sweden.

76. Charlton, M., Griffith, T. C., Heyland, G. R. & Wright, G. L. Total scattering cross sections for low-energy positrons in the molecular gases H_2 , N_2 , CO_2 , O_2 and CH_4. *Journal of Physics B: Atomic and Molecular Physics* **16,** 323–341. doi:10.1088/0022-3700/16/2/019 (1983).

77. Marler, J. P. & Surko, C. M. Positron-impact ionization, positronium formation, and electronic excitation cross sections for diatomic molecules. *Physical Review A* **72,** 062713. doi:10.1103/PhysRevA.72.062713 (2005).

78. Cooke, D. A., Murtagh, D. J. & Laricchia, G. Positronium formation cross-sections for Xe, CO_2 and N_2. *Journal of Physics: Conference Series* **199,** 012006. doi:10.1088/1742-6596/199/1/012006 (2010).

79. Natisin, M. R., Danielson, J. R. & Surko, C. M. Positron cooling by vibrational and rotational excitation of molecular gases. *Journal of Physics B: Atomic, Molecular and Optical Physics* **47,** 225209. doi:10.1088/0953-4075/47/22/225209 (2014).

80. Baker, C. J. *et al.* Measurements of Penning-Malmberg trap patch potentials and associated performance degradation. *Physical Review Research* **6,** L012008. doi:10.1103/PhysRevResearch.6.L012008 (2024).

81. Bordoni, F. Channel electron multiplier efficiency for 10–1000 eV electrons. *Nuclear Instruments and Methods* **97,** 405–408. doi:10.1016/0029-554X(71)90300-4 (1971).

82. Newson, D. *et al.* Detection of low-energy charged particles by channel electron multipliers. *Journal of Instrumentation* **17,** P11026. doi:10.1088/1748-0221/17/11/P11026 (2022).

83. Baird, S. A. *et al. Design study of the antiproton decelerator* tech. rep. CERN/PS 96-43 (AR) (CERN, Geneva, Switzerland, 1996). doi:10.17181/CERN.KNXM.AYKR.

84. Möhl, D., Petrucci, G., Thorndahl, L. & van der Meer, S. Physics and technique of stochastic cooling. *Physics Reports* **58,** 73–102. doi:10.1016/0370-1573(80)90140-4 (1980).

85. Poth, H. Electron cooling: Theory, experiment, application. *Physics Reports* **196,** 135–297. doi:10.1016/0370-1573(90)90040-9 (1990).

86. Chohan, V. *et al. Extra Low ENergy Antiproton (ELENA) ring and its Transfer Lines: Design Report* tech. rep. (CERN, Geneva, 2014). doi:10.5170/CERN-2014-002.

87. Nordlund, K., Hori, M. & Sundholm, D. Large nuclear scattering effects in antiproton transmission through polymer and metal-coated foils. *Physical Review A* **106,** 012803. doi:10.1103/PhysRevA.106.012803 (2022).

88. Kuroda, N. *et al.* Development of a monoenergetic ultraslow antiproton beam source for high-precision investigation. *Physical Review Special Topics - Accelerators and Beams* **15,** 024702. doi:10.1103/PhysRevSTAB.15.024702 (2012).

89. Amsler, C. *et al.* Injection and capture of antiprotons in a Penning–Malmberg trap using a drift tube accelerator and degrader foil. *Nuclear Instruments and Methods in Physics Research Section A: Accelerators, Spectrometers, Detectors and Associated Equipment* **1065,** 169529. doi:10.1016/j.nima.2024.169529 (2024).

90. Hori, M., Yamashita, K., Hayano, R. & Yamazaki, T. Analog Cherenkov detectors used in laser spectroscopy experiments on antiprotonic helium. *Nuclear Instruments and Methods in Physics Research Section A: Accelerators, Spectrometers, Detectors and Associated Equipment* **496,** 102–122. doi:10.1016/S0168-9002(02)01618-2 (2003).

91. Kuroda, N. *et al.* Antihydrogen atom formation in a CUSP trap towards spin polarized beams. *Hyperfine Interactions* **212,** 31–40. doi:10.1007/s10751-012-0646-z (2012).

92. Caspers, F. *Experience with UHV-compatible microwave absorbing materials at CERN* Technical Report CM-P00059508 (CERN, 1993).

93. Radics, B. *et al.* The ASACUSA Micromegas Tracker: A cylindrical, bulk Micromegas detector for antimatter research. *Review of Scientific Instruments* **86,** 083304. doi:10.1063/1.4927685 (2015).

94. Costantini, G. *et al.* The upgrade of the ASACUSA scintillating bar detector for antiproton annihilation measurements. *Journal of Instrumentation* **18,** P04013. doi:10.1088/1748-0221/18/04/P04013 (2023).

95. Gallagher, T. F. *Rydberg Atoms Cambridge Monographs on Atomic, Molecular and Chemical Physics* **3.** ISBN: 0-521-38531-8 (Cambrige University Press, 1994).

96. Federmann, S. *A Spin-Flip Cavity for Microwave Spectroscopy of Antihydrogen* PhD thesis (Universität Wien, 2012).

97. Arguedas Cuendis, S. *Measuring the hydrogen ground state hyperfine splitting through the π1 and σ1 transitions* MA thesis (Universität Wien, 2017).

98. Kraxberger, V. *et al.* Upgrade of ASACUSA's antihydrogen detector. *Nuclear Instruments and Methods in Physics Research Section A: Accelerators, Spectrometers, Detectors and Associated Equipment* **1045,** 167568. doi:10.1016/j.nima.2022.167568 (2023).

99. Kraxberger, V. *Upgrade of ASACUSA's Antihydrogen Detector* MA thesis (Universität Wien, 2022).

100. Weiser, A. *et al.* A compact low energy proton source. *Review of Scientific Instruments* **94,** 103301. doi:10.1063/5.0162339 (2023).

101. Straub, H. C., Renault, P., Lindsay, B. G., Smith, K. A. & Stebbings, R. F. Absolute partial cross sections for electron-impact ionization of H_2, N_2 , and O_2 from threshold to 1000 eV. *Physical Review A* **54,** 2146–2153. doi:10.1103/PhysRevA.54.2146 (1996).

102. Kersevan, R. & Ady, M. Recent Developments of Monte-Carlo Codes Molflow+ and Synrad+. *Proceedings of the 10th Int. Particle Accelerator Conf.* **IPAC2019,** 4 pages, 2.540 MB. doi:10.18429/JACOW-IPAC2019-TUPMP037 (2019).

103. Jagutzki, O. *et al.* Position sensitive anodes for MCP read-out using induced charge measurement. *Nuclear Instruments and Methods in Physics Research Section A: Accelerators, Spectrometers, Detectors and Associated Equipment* **477,** 256–261. doi:10.1016/S0168-9002(01)01843-5 (2002).

104. Blaum, K. *et al.* Population inversion of nuclear states by a Penning trap mass spectrometer. *Europhysics Letters (EPL)* **67,** 586–592. doi:10.1209/epl/i2004-10089-5 (2004).

105. Andersen, S. L. *Positronium Formation & Cooling in Meso-Structured Silica Films* PhD thesis (Aarhus University, Aarhus (Denmark), 2015).

106. Evans, L. T. *Phenomenology of creation of antihydrogen and measurement of antihydrogen properties* PhD thesis (University of California, Berkeley, Berkeley, 2016).

107. Eggleston, D. L., Driscoll, C. F., Beck, B. R., Hyatt, A. W. & Malmberg, J. H. Parallel energy analyzer for pure electron plasma devices. *Physics of Fluids B: Plasma Physics* **4,** 3432–3439. doi:10.1063/1.860399 (1992).

108. Andersen, S. L. *et al.* Positronium formation from porous silica in backscattering and transmission geometries. *The European Physical Journal D* **68,** 124. doi:10.1140/epjd/e2014-40762-x (2014).

109. Danielson, J. R., Dubin, D. H. E., Greaves, R. G. & Surko, C. M. Plasma and trap-based techniques for science with positrons. *Reviews of Modern Physics* **87,** 247–306. doi:10.1103/RevModPhys.87.247 (2015).

110. Hunter, E. *et al.* SDR, EVC, and SDREVC: Limitations and Extensions. *Journal of Plasma Physics* **89,** 955890501. doi:10.1017/S0022377823001022 (2023).

111. Horizon Fuel Cell Technologies. *HYDROFILL PRO FCH-020*

112. Horizon Fuel Cell Technologies. *HYDROSTIK PRO LWH22-10L-5*

113. Greaves, R. G., Tinkle, M. D. & Surko, C. M. Creation and uses of positron plasmas. *Physics of Plasmas* **1,** 1439–1446. doi:10.1063/1.870693 (1994).

114. Gabrielse, G. *et al.* Antihydrogen Production within a Penning-Ioffe Trap. *Physical Review Letters* **100,** 113001. doi:10.1103/PhysRevLett.100.113001 (2008).

115. Andresen, G. *et al.* Antihydrogen formation dynamics in a multipolar neutral anti-atom trap. *Physics Letters B* **685,** 141–145. doi:10.1016/j.physletb.2010.01.066 (2010).

116. Cripe, M. G. *Summer Student project report: counting antiprotons in ASACUSA's Cusp trap* CERN, 2024.

117. Battistoni, G. *et al.* Overview of the FLUKA code. *Annals of Nuclear Energy. Joint International Conference on Supercomputing in Nuclear Applications and Monte Carlo 2013, SNA + MC 2013. Pluri- and Trans-disciplinarity, Towards New Modeling and Numerical Simulation Paradigms* **82,** 10–18. doi:10.1016/j.anucene.2014.11.007 (2015).

118. Malmberg, J. H. & O'Neil, T. M. Pure Electron Plasma, Liquid, and Crystal. *Physical Review Letters* **39,** 1333–1336. doi:10.1103/PhysRevLett.39.1333 (1977).

119. Amoretti, M. *et al.* Antihydrogen production temperature dependence. *Physics Letters B* **583,** 59–67. doi:10.1016/j.physletb.2004.01.009 (2004).

120. Amoretti, M. *et al.* Positron Plasma Diagnostics and Temperature Control for Antihydrogen Production. *Physical Review Letters* **91,** 055001. doi:10.1103/PhysRevLett.91.055001 (2003).

121. Stevefelt, J., Boulmer, J. & Delpech, J.-F. Collisional-radiative recombination in cold plasmas. *Physical Review A* **12,** 1246–1251. doi:10.1103/PhysRevA.12.1246 (1975).

122. Jones, J. M. *Sympathetically Laser-Cooled Positron Plasmas for Antihydrogen Formation* PhD thesis (Swansea University, Swansea, 2022).

123. Jonsell, S. & Charlton, M. Formation of antihydrogen beams from positron–antiproton interactions. *New Journal of Physics* **21,** 073020. doi:10.1088/1367-2630/ab2bdc (2019).